A Study of the Ultrahigh-Energy Cosmic Ray Mass Composition with the MACRO and EAS-TOP Experiments

Thesis by

Stéphane Coutu

In Partial Fulfillment of the Requirements
for the Degree of
Doctor of Philosophy

California Institute of Technology
Pasadena, California
1993
(Submitted May 4)

Acknowledgements

I feel extremely fortunate to have experienced the guidance of my thesis advisor, Charles W. Peck, for I have learned from him not only much physics, but also an entire philosophy of scientific thinking. I have also benefitted tremendously from the example of Barry C. Barish, who has always been supportive and available, and provided me with the right opportunities at the right times. To them both, I will be forever indebted and grateful.

In large collaborative efforts such as MACRO and EAS-TOP, the contribution of any individual is built upon the work of many others, and I gratefully acknowledge all members of both collaborations, who are listed in Appendix A, and many of whom have become very good friends. I wish to thank particularly the other members of the MACRO/EAS-TOP analysis team: F. Arneodo, G. Battistoni, M. Carboni, M. Monteno, G. Navarra, V. Patera and P. Vallania. I thank the Caltech contingent of MACRO collaborators, fellow students (in particular J.T. Hong) and support staff for contributing to making the Institute such a unique and stimulating place to work. I wish to thank M. Spinetti and the Istituto Nazionale di Fisica Nucleare of Italy for some generous travel support.

Finally, I thank my family for giving me the crucial early support in life, and most of all my wife Meng-Lin, for not only her constant love and support, but also for her admirable understanding in putting up with so many months of separation during long trips to Italy.

Note

The collaborative venture between the EAS-TOP and MACRO experiments is unique, in that the two are separate and distinct, with no overlap in terms of collaborators, and altogether different sets of physical goals. An analysis team with members from both collaborations was formed (including the author of this thesis - a member of the MACRO collaboration - and the persons acknowledged above), and the work was carried out under a protocol whereby only fully reconstructed information, event by event, was exchanged between the two experiments; the EAS-TOP researchers were entirely and solely responsible for all aspects of the EAS-TOP experiment and for the reconstructions of parameters of air showers at the ground surface, and *vice versa* for the MACRO experiment and reconstructions of muon events deep-underground. Within the analysis team, the author of this thesis has been responsible for the identification of coincident and anticoincident events and their MACRO reconstructions, with subsequent extensive comparison with the EAS-TOP reconstructions. The Monte Carlo analysis has been a true team effort, with responsibilities distributed among the various members of the analysis team. Some of the results presented in this thesis have previously been published (see Reference [1]) whereas others will be published in the near future (Reference [2]), under the combined authorship of the entire MACRO and EAS-TOP collaborations.

Abstract

Two components of cosmic-ray-induced air showers are measured simultaneously at the Gran Sasso Laboratory: the electromagnetic shower at the ground surface by the EAS-TOP extensive air shower array, and the deep-underground muons by the MACRO experiment. The two independent data sets collected during 96.3 days of simultaneous running are combined, and underground muon multiplicity distributions are obtained for anticoincident events (no surface trigger) and high-energy, coincident events. These categories correspond to ranges in primary energy from about 2×10^3 GeV to a few times 10^5 GeV, and from about 1.5×10^5 GeV to about 10^7 GeV, respectively.

The experimental shower size and muon multiplicity distributions, as well as the distribution of mean muon multiplicity as a function of shower size ($\overline{N}_\mu - \log(N_e)$ relation), are compared to the ones obtained with detailed Monte Carlo calculations (with a generator based on recent hadronic accelerator data) using various trial compositions as input. This is done in an effort to discriminate between these models of primary cosmic-ray mass composition at and above the "knee" in the all-particle spectrum, where contradictory experimental evidence exists and where a knowledge of the composition would bear upon possible mechanisms for cosmic-ray acceleration and propagation.

Detailed studies of simulated anticoincident event rates (which arise from a region of primary energy where the composition has been measured directly by satellite and

balloon experiments) uncover problems with the generator used, with between 25 and 40% too few high-energy muons created. This, combined with the dependence of absolute event rates on the assumed differential primary energy spectra, hampers the interpretation in terms of composition of underground muon or surface air shower data taken separately. However, the $\overline{N}_\mu - \log(N_e)$ relation is independent of the spectra or overall Monte Carlo normalization problems. The simulated $\overline{N}_\mu - \log(N_e)$ relation for coincident events is found to be inconsistent with the possibility that the cosmic ray flux becomes proton-dominated at and above the knee.

Table of Contents

List of Figures

List of Tables

Chapter 1

Primary Cosmic Ray Composition

In this chapter, we begin by describing the measured differential energy spectrum of cosmic rays of all types. We then describe the mass composition of cosmic rays as directly measured by balloon-borne and satellite detectors. Then, at higher energies, we mention the efforts at determining the cosmic ray composition by studying the end products of air showers produced by cosmic rays: electromagnetic air showers observed on the ground surface, or deep-underground muon bundles. We then summarize the current status of theoretical work concerning the origin, acceleration and propagation of cosmic rays. Finally, we introduce the MACRO/EAS-TOP approach to studying the composition, linking it with other topics covered in the chapter.

1.1 All-particle differential energy spectrum

The differential energy spectrum of primary cosmic rays of all types (the "all-particle spectrum") is shown in Fig. 1.1, with the flux values on the ordinate axis scaled by a factor of $E^{2.5}$ (where E is the total primary energy in GeV) to enhance its details. It spans many decades in energy, and has been measured over a period of many years by several different experiments utilizing different techniques. Only some represen-

tative experiments are shown: the direct PROTON satellite measurements (see Reference [3]) and direct JACEE balloon-borne measurements (see Reference [4]), and two indirect, air shower array measurements (Tien Shan, Reference [5], and Akeno, Reference [6]). The spectrum falls very steeply with energy, following a power law $E^{-\gamma}$, with $\gamma \simeq 2.6 - 2.7$, for several decades in energy, but further steepening to $\gamma \simeq 3.0$ for energies greater than a few times 10^6 GeV. This steepening, or change in the spectral index $\zeta = (1 - \gamma)$, is traditionally called the "knee" of the cosmic ray spectrum. Cosmic ray acceleration and propagation models attempt to reproduce this power law behavior and to explain the knee; we will return to this in Section 1.4. (In the remainder of this thesis, the expressions "below the knee" and "above the knee" are taken to refer to primary energies smaller or greater, respectively, than that at which the steepening occurs.)

At energies below a few times 10^5 GeV, the absolute all-particle flux has been measured directly, and is therefore known to good accuracy (about 10%). However, higher energy measurements are obtained indirectly, typically by sampling the electromagnetic component of the cosmic-ray-induced air shower with an array of counters on the ground surface, and then attempting to determine the primary energy corresponding to a reconstructed total shower size. This procedure requires many assumptions and much Monte Carlo modelling, and therefore results in uncertainties in the absolute flux, typically on the order of 20 to 30 % (see Reference [7]). As balloon-borne and satellite detectors become ever larger and are exposed for increasing periods of time, the directly measured flux approaches the knee, and some doubt is being cast on whether the slope change around the knee is as abrupt as determined by indirect air shower experiments (see Reference [8]). However, there is still much uncertainty in these measurements, as the balloon-borne detectors are typically stacks of emulsion chambers separated by metallic absorbers, and much of the parent energy leaks out of the bottom of the detector at high energies, making a

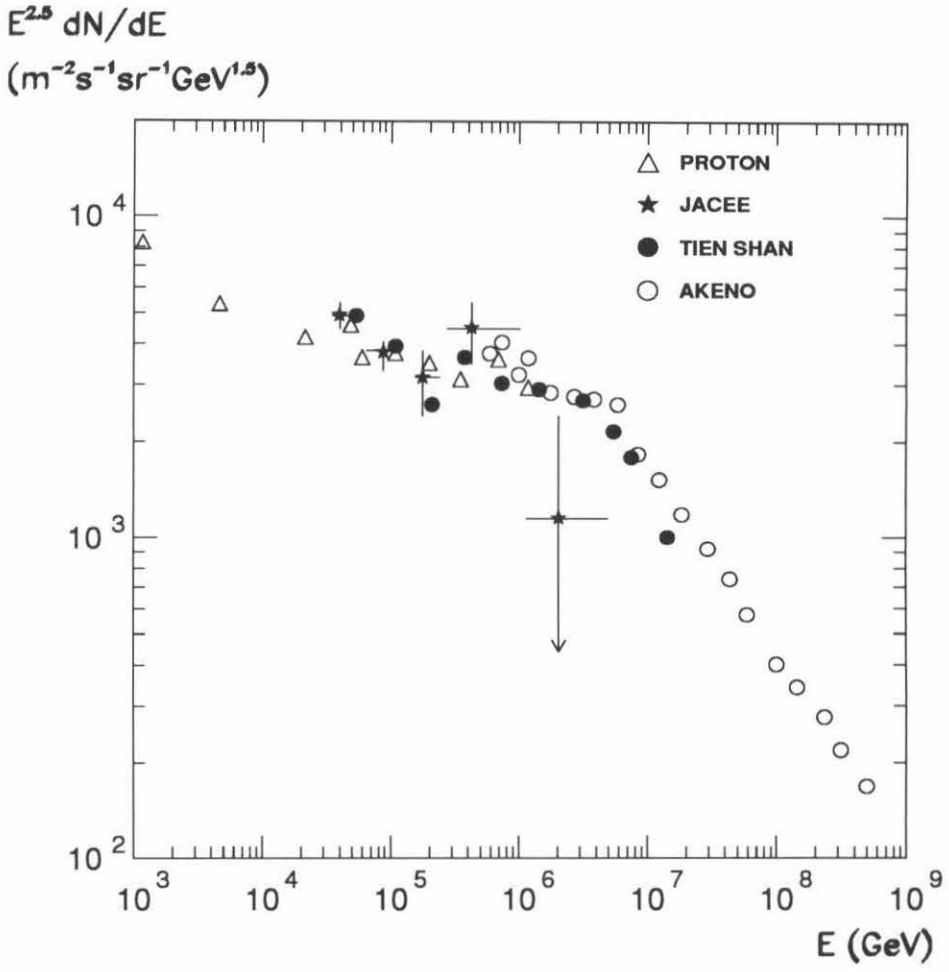

Figure 1.1: All-particle, primary cosmic ray differential energy spectrum, with the ordinate axis values scaled by a factor of $E^{2.5}$. The data are from the PROTON satellite experiments (see Reference [3]), the JACEE balloon experiments (see Reference [4]), the Tien Shan air shower array (see Reference [5]) and the Akeno air shower array (see Reference [6]).

precise energy estimate difficult.

Note that the measured spectrum extends below and above the range plotted in Fig. 1.1. In Section 1.2.1 we describe primary composition in the low-energy region. At energies greater than 10^9 GeV, and indeed up to about 10^{11} GeV, lie the most energetic particles ever observed. Interesting questions are whether the cosmic ray spectrum cuts off due to photopion interactions of the primaries with the 2.7 K cosmic microwave background (see References [9] and [10]), and whether cosmic rays of such high energies originate from outside our galaxy (see Reference [11]). This highest energy region is beyond the purview of this thesis, and we shall not discuss it any further.

1.2 Direct primary composition measurements

1.2.1 Low-energy cosmic ray composition

In Reference [12], the elemental cosmic ray composition at low energies (from 0.07 GeV/amu to 2 GeV/amu) is extensively reviewed. Fig. 1.2, taken from it, shows the abundances of the elements He to Ni, in cosmic rays and in the solar system, all relative to the abundance of Si (set to 10^2). The solar system abundances are calculated using data from terrestrial, lunar and meteoritic samples, and from solar spectroscopic measurements (see Reference [12] and references therein). Both the cosmic ray and solar system data show an even-odd effect, where nuclei with even charge Z, being more tightly bound, are more abundant. Nuclei with Z>1 are at least about ten times more abundant relative to protons in the cosmic rays than in the solar system. Although this is not fully understood, it could be related to the fact that hydrogen is relatively hard to ionize for injection into cosmic accelerators. Another important difference is that several elements such as Li, Be and B on the one hand, and Sc to Mn on the other, are orders of magnitude more abundant

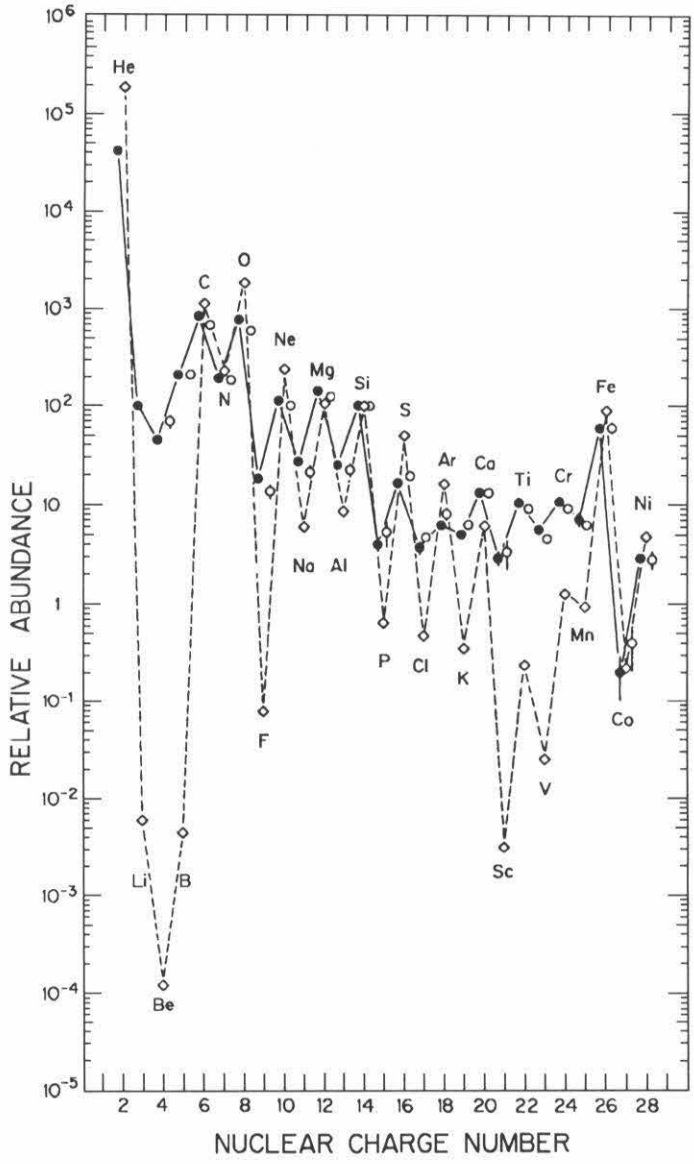

Figure 1.2: Measured abundances of elements He to Ni in low-energy cosmic rays at the top of the Earth's atmosphere, compared to solar system abundances (taken from Reference [12]); all abundances are relative to Si. Solid circles: data in the energy range 0.07 to 0.28 GeV/amu; open circles: data in the range 1 to 2 GeV/amu; diamonds: solar system abundances.

in the cosmic rays than in the solar system. These elements essentially do not appear as end results of stellar nucleosynthesis, but they are created in cosmic rays as spallation products of heavier primaries (C and O on the one hand, and Fe on the other) colliding with interstellar material. As mentioned in Reference [13], p. 8, knowledge of the spallation cross-sections can be invoked to deduce that such cosmic rays have traversed on the order of 5 to 10 g/cm^2 of material in propagating from their source to us, and that this corresponds to a distance traveled of at least about 1000 kpc (compared with the galactic disk thickness of about 0.2 kpc). Cosmic rays are therefore confined by galactic magnetic fields for a long time, spending much of their time in the diffuse galactic halo, before possibly escaping the galaxy.

Note that particles other than nuclei are produced in interstellar collisions, but they account for only a very small fraction of the total cosmic ray flux. For example, electrons and positrons comprise less than about 2%, and gammas about 10^{-3}, of the total flux (see Reference [14], p. 7).

1.2.2 High-energy cosmic ray composition

At total primary energies from a few GeV up to about 10^6 GeV, it is often convenient to classify primaries into five mass groups: p (A = 1), He (A = 4), C-N-O (A = 14), Ne-Mg-Si (A = 24) and Fe (A = 56). Other primaries are also present, but to a lesser extent that becomes increasingly negligible with primary energy (see Reference [8]). The differential energy spectrum below 10^6 GeV for each primary mass group is shown in Fig. 1.3, together with the all-particle spectrum in the same energy region. The legend for Fig. 1.3 is as follows: 1) five mass groups: (diamonds: Ormes and Webber, Reference [15]), (filled stars: Ryan *et al.*, Reference [16]), (filled circles: JACEE, Reference [4]), (crosses: Kawamura *et al.*, Reference [17]), (filled triangles: HEAO-3-C2, Reference [18]), (triangles: Simon *et al.*, Reference [19]), (circles: CRN, Reference [20]), (stars: Ichimura *et al.*, Reference [8]); 2) all-particle spectrum:

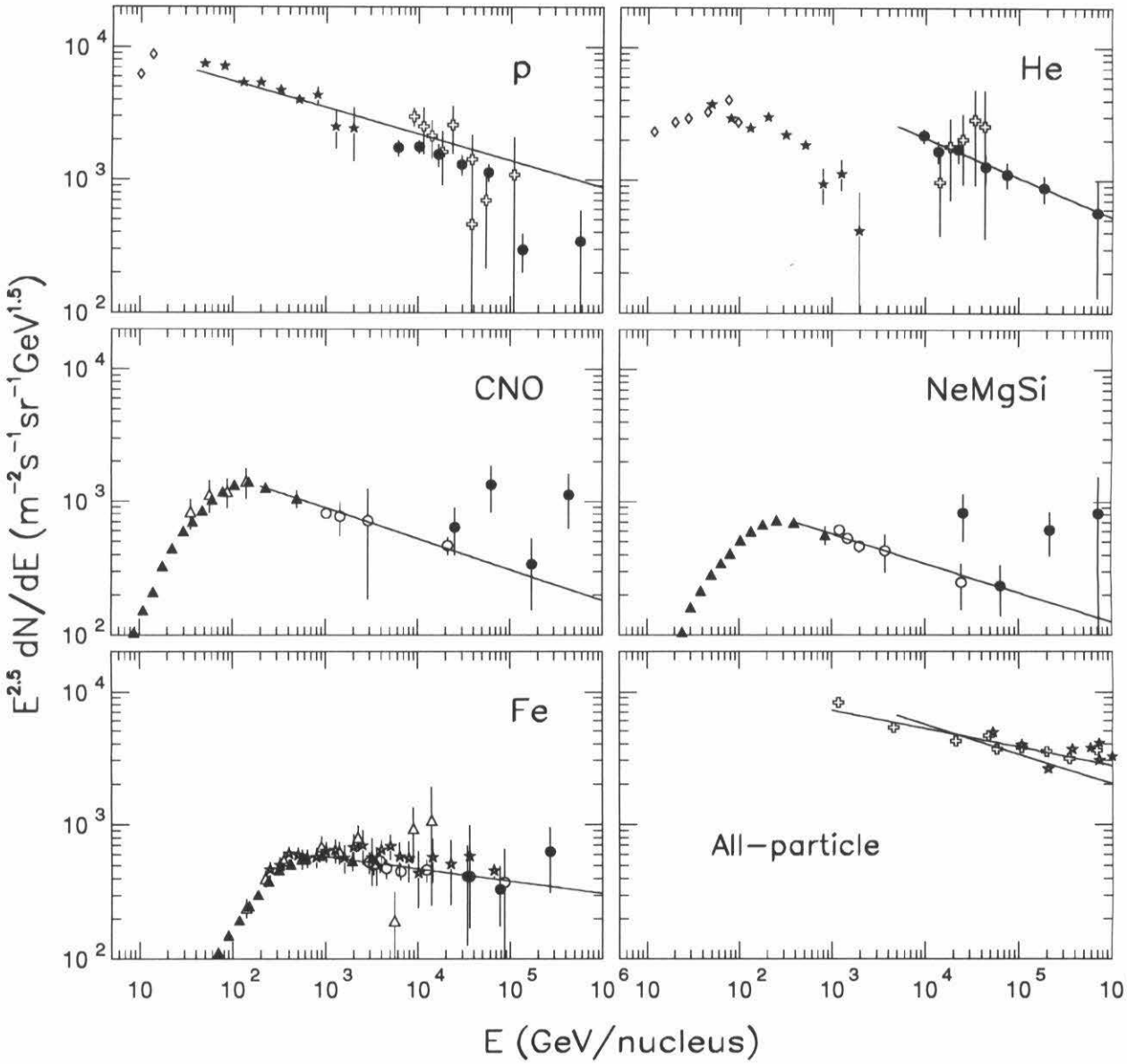

Figure 1.3: Experimental differential energy spectra below 10^6 GeV for the five primary mass groups p, He, CNO, NeMgSi and Fe, and all-particle spectrum. Fluxes are scaled by $E^{2.5}$. See text for references and a description of the curves.

(crosses: PROTON, Reference [3]), (stars: Tien Shan, Reference [5]), (filled stars: Akeno, Reference [6]). For the He spectrum, the data below 4000 GeV does not extrapolate well to the higher energy region, and there could be some normalization problem with either the older, lower-energy data or more recent, higher-energy measurements. However, uncertainties above 4000 GeV are fairly large, and will shrink with time with longer-duration flights. The curves drawn through the five mass groups spectra are power-law fits (disregarding the JACEE data for the CNO and NeMgSi fits). The JACEE data seem to indicate a steepening in the p spectrum at the highest energies attained, whereas they indicate a flattening of the CNO and NeMgSi spectra. For the all-particle spectrum, the flatter curve is a power-law fit, whereas the steeper curve is that obtained by summing the fits for the five mass groups. Good agreement is achieved, especially given the large uncertainties at high energies. However, if the flattening of the CNO and NeMgSi spectra observed by JACEE is real, an extra component could account for the difference.

1.3 Indirect primary composition studies

1.3.1 Underground studies

As larger detectors are flown to the top of the atmosphere for increasingly extended periods of time, the cosmic ray mass composition is directly measured at ever higher energies. However, the knee in the all-particle spectrum, at a few thousand GeV, where the composition could drastically change (see Section 1.4), remains an unattained goal. Therefore, at energies around and above the knee, indirect methods have to be used to study the primary composition.

When a cosmic ray primary nucleus strikes the Earth's atmosphere, it interacts hadronically with atmospheric nuclei, typically nitrogen or oxygen. In the ensuing cascade, many secondary particles are produced, some of which decay and some fur-

ther interact to feed the hadronic core of the air shower (an overview of air showers can be found in Reference [13], Chapter 14). Pions and kaons are produced copiously, and neutral pions decay to two gammas. These gammas initiate an electromagnetic air shower that accompanies the hadronic shower (a classic discussion of electromagnetic air showers is that of Reference [21]). Some of the charged pions and kaons decay to high-energy (TeV) muons. The latter are nearly stable and quite penetrating, so that they can be detected deep underground, at depths of the order of, say, one kilometer, whereas the rest of the shower has since been absorbed.

The high-energy muons bear information closely related to the parent itself, as they originate from the very early stages of the cascade. For instance, they still travel along trajectories that are quite parallel to that of the parent; in fact, multiple muons from the same primary spread out over on the order of a few meters, even after travelling on the order of forty kilometers (see Reference [22] and Figs. 5.6 and 5.7). The relative rate of events of various muon multiplicities can be used as a basis for comparison with different models. Sensitivity to composition arises from the fact that heavy primaries are more efficient at producing large muon multiplicities than light primaries, provided that the energy per nucleon stored in the primary is large enough to yield high-energy muons (see Reference [22]). For a very high-energy primary of mass A, the muon multiplicity underground is roughly proportional to $A^{0.243}$ (see Reference [13], p. 209). Typically, the comparison between experimental data and model predictions involves large and complex Monte Carlo calculations where the early interactions are simulated, and the high-energy muons created, propagated through the atmosphere and the rock above the detector, and then sampled by the finite-sized simulated apparatus. Various primary composition models are assumed, and the resulting calculated muon multiplicities are compared with the experimentally measured distribution in an attempt to discriminate between models. This approach is hampered by the necessity of making many assumptions, such as

extrapolating known physics to energies heretofore unexplored by accelerators. Another difficulty is that a given multiplicity underground can arise from a proton of a certain energy, or a heavy primary of a higher energy, and any observed multiplicity distribution receives contributions from primaries of a wide possible range of energies (several orders of magnitude). Convoluted with this is the finite size of the detector, which can cause biases in multiplicity estimates. Moreover, a good knowledge of the rock overburden is necessary, which can be problematic.

An example of the application of this method is a MACRO study (see Reference [23]), where experimental muon multiplicity distributions are compared with those obtained with two primary composition models, one where a predominantly light composition is assumed, and another, heavy composition model. The result is shown in Fig. 1.4. Both the light and heavy composition models are normalized to agree with the all-particle spectrum shown in Fig. 1.1. The study shows a preference toward a light composition, with a large proton component, in a primary energy window from about 5×10^4 GeV to several times 10^6 GeV.

The Fréjus detector is also well-suited to the study of underground muon bundles (see Reference [24]). In comparing various composition models with this data, in Reference [25], it is also found that a light, proton-rich composition agrees best with the experimental results in the region of the knee. In Reference [26], the Homestake collaboration also concludes that a light composition around the knee is necessary to explain its observed muon rates.

The Baksan and NUSEX experiments are two other underground detectors suitable for muon detection. In Reference [27], a Baksan multiplicity distribution is compared with that from NUSEX (see Reference [28]), and the one from Fréjus mentioned above. It is concluded that a constant mass composition model is consistent with the multiplicity distribution of all three experiments, *i.e.*, one where the composition at and above the knee is a simple extrapolation of lower-energy composition

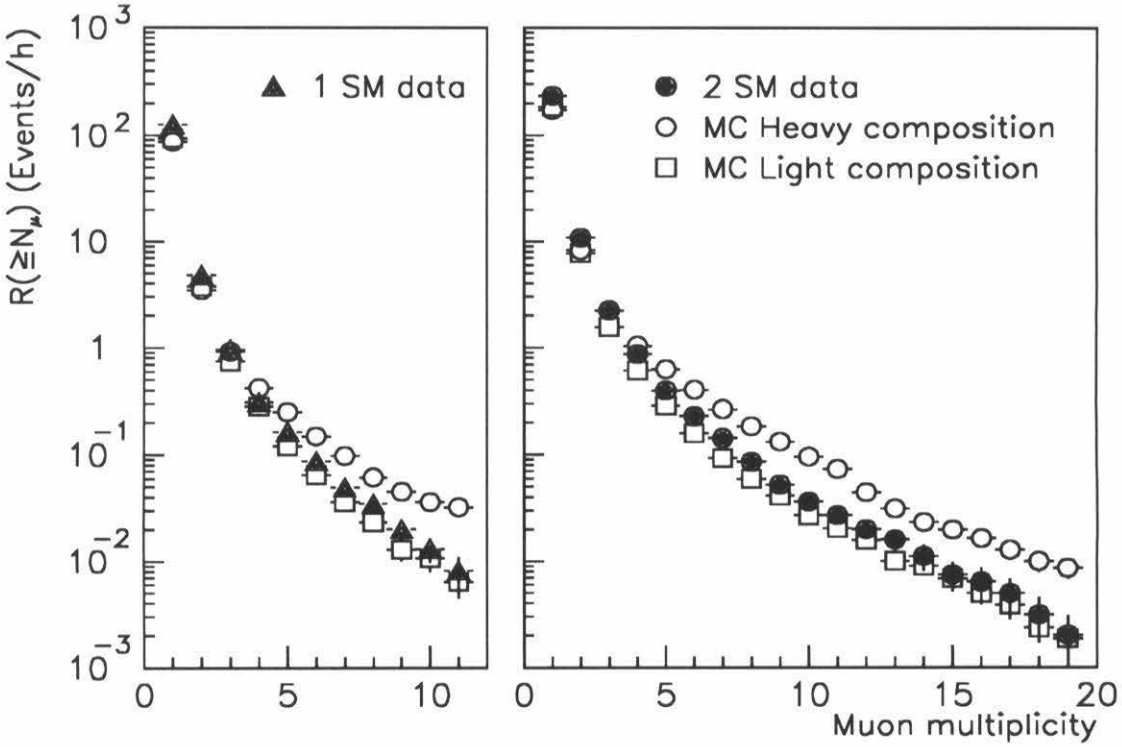

Figure 1.4: Integral muon multiplicity distributions recorded by MACRO with one and two supermodules (see Chapter 2) in operation, compared with Monte Carlo calculations assuming a light or heavy primary composition (taken from Reference [23]).

measurements (such as those from Fig. 1.3), with a constant relative proportion of each mass group.

In Reference [29], an analysis of shallower muon data from three experiments (Tien Shan, Moscow State University and Kolar-gold-field) concludes that the data are consistent with a composition dominated by heavy primaries around the knee, although it is pointed out that the discriminatory power between various models is not great.

1.3.2 Surface studies

In an air shower, the electromagnetic shower front has spread out over hundreds of meters by the time it reaches ground level (assuming the total amount of energy available to the shower is large enough that the cascade does not get expended entirely in the atmosphere), and can be sampled by an array of scintillation counters. From the particle densities sampled by the counters, various characteristics of the primary cosmic ray, and in particular the total shower size, can be reconstructed. Air shower arrays are often equipped with a number of muon counters buried at a shallow depth underneath the array. By comparing shower size and low-energy muon lateral distributions for the experimental data with those obtained with Monte Carlo calculations assuming various composition models, some discriminatory power is achieved. In this manner, the Ohya experiment (see Reference [30]) concludes that protons account for $\sim 80\%$ of the total flux at 10^6 GeV and progressively less with energy to $10 \sim 20\%$ at 10^7 GeV, whereas heavier nuclei become dominant.

At high altitudes, *e.g.*, on mountains, emulsion chambers are used to study the hadronic and gamma-ray content of air showers. Again, observed quantities such as number of particles and lateral distributions thereof are compared with extensive Monte Carlo calculations. In Reference [31], the Mt. Fuji and China-Japan collaborations conclude from their work that at energies between 10^6 and 10^7 GeV,

cosmic rays are 30 - 40% protons and He nuclei (in equal proportions), with 60 - 70% heavy nuclei. In another mountain experiment (Reference [32]), this one looking for delayed hadrons as a signature for heavy nuclei, it is estimated that iron-group nuclei account for about 40% of the total flux at energies between 10^4 and 10^6 GeV. Another, similar experiment (Reference [33]), this one at sea level, concludes that the primary flux at 10^6 GeV cannot be dominated by protons.

Cerenkov light emitted by air shower particles travelling through the atmosphere can be detected on the ground, and used to extract information on the longitudinal development of a shower, particularly the height at which the shower reaches maximum development. Fluctuations in the height of shower maximum can be used to discriminate statistically between showers initiated by light or heavy primaries, where heavier primaries tend to yield a higher shower-maximum height and smaller fluctuations in this height than lighter ones. In Reference [34], data from the Dugway atmospheric Cerenkov light detector is used to conclude that the primary flux is predominantly iron-like at 10^7 GeV, becoming lighter with energy. At 10^8 GeV, using the same technique, the Fly's Eye collaboration concludes in Reference [35] that the composition cannot be dominated by protons. In Reference [36], a similar analysis concludes that depth of shower maximum fluctuations are consistent with a constant mass composition at energies 1.5×10^8 GeV and greater.

It is clear from the experimental overview presented in this Section that the evidence is contradictory and that the composition near and above the knee is unknown. We now review briefly the theoretical situation.

1.4 Cosmic ray acceleration and propagation models

Models of cosmic ray origin, acceleration and propagation are constrained by the experimentally determined all-particle energy spectrum of Fig. 1.1, and by the direct composition measurements below the knee (Fig. 1.3). In particular, acceleration mechanisms should be capable of explaining the observed power-law dependence of the flux on primary energy, and the change in spectral index at the knee. At the highest observed energies, it becomes a serious challenge to find any mechanism at all capable of accelerating charged particles to such energies.

The most widely accepted theoretical scenario, currently, is that cosmic rays are accelerated by a diffuse Fermi process at astrophysical shocks, such as those emanating from supernova explosions, up to energies below and around the knee. The knee itself is thought to be due to the onset of rigidity-dependent escape from the galaxy (the so-called "leaky-box model"). At energies above the knee, acceleration at compact objects such as pulsars and X-ray binary star systems is invoked, with the possibility of a contribution from active galactic nuclei. In the following, we briefly review this scenario. (A useful review that summarizes this is Reference [37].)

1.4.1 Acceleration below the knee

The details of diffuse Fermi acceleration at supernova shock fronts are reviewed in Reference [38].

With an estimated energy density stored in cosmic rays of about $\rho_E \sim 1$ eV/cm^3 (see Reference [13], p. 148), the volume of the galactic disk $V_D \sim 4 \times 10^{66}$ cm^3 and the residence time of cosmic rays in the disk of the galaxy $\tau_R \sim 6 \times 10^6$ years, the power required to supply all of the galactic cosmic rays is about $L_{CR} = V_D \rho_E / \tau_R$ $\sim 5 \times 10^{40}$ erg/s, whereas the power output from one 10 solar-mass type II supernova every 30 years ejecting material at 5×10^8 cm/s is about 3×10^{42} erg/s. The similarity

of these two estimates makes supernovae a likely source of high-energy cosmic rays; an efficiency of only a few percent in converting the blast energy to cosmic ray kinetic energy would suffice to account for the total cosmic ray flux.

In first-order Fermi acceleration, as a charged particle (moving through a yet unshocked gas) encounters the approaching magnetized plasma from a supernova blast, it can undergo a series of magnetic scatterings on the shocked side of the front and reemerge with an energy increased by an amount proportional to its initial energy. Specifically, if u_1 is the speed of the shock front in the laboratory frame and u_2 is that at which the shocked gas recedes from the shock front, then the energy gained in the encounter is given approximately by $\Delta E = \xi E$ where $\xi = 4(u_1 - u_2)/(3c)$ (see Reference [13], Chapter 11). If the probability of escape from the accelerating region per encounter is P, then the total number of particles accelerated to energies greater than E from an initial energy E_0 is proportional to $P^{-1}(E/E_0)^{-\zeta}$, with $\zeta = 3/(u_1/u_2 - 1)$. If the speed of sound in the unshocked gas is c_1, then a shock can form if $u_1 > c_1$, and the Mach number of the flow is $M = u_1/c_1$. For a monatomic gas and a strong shock, $\zeta \simeq 1 + 4/M^2$.

To summarize, this model predicts a power-law energy dependence of the cosmic ray flux after acceleration, with a universal spectral index that can take on reasonable values (as we will see in Section 1.4.2, the leaky-box model requires a differential spectral index of about 2.1 from the source, which corresponds to an integral spectral index $\zeta \sim 1.1$). However, this acceleration mechanism results in a maximum energy of about $E_{max} \leq Z \times 3 \times 10^4$ GeV (see Reference [13], p. 159) due to the finite lifetime of the supernova blast as a strong shock, where Z is the charge of the particle. Therefore, other mechanisms have to be invoked to account for particles of higher energies. A byproduct of this effect is that higher Z particles would have a higher maximum energy, and the composition could become progressively richer in heavy primaries.

1.4.2 Leaky-box model of the galaxy

There is significant evidence that most of the cosmic rays observed originate within our own galaxy (from studies of anisotropies in cosmic ray arrival directions, see Reference [39], or from searches for gamma-ray emissions from the Small Magellanic Cloud, see Reference [40]). However, a study of the low-energy cosmic rays created by spallation of heavier nuclei (see Section 1.2.1 and Reference [13], Chapter 9) suggests that they have traveled distances thousands of times greater than the thickness of the galactic disk, and therefore must have diffused in a containment volume including a significant fraction of the galaxy (with galactic magnetic fields, on the order of μG-strong, being the agent of such confinement), and perhaps the galactic halo as well. If the galactic magnetic field (expressed in μG) is B, a relativistic particle of charge Z and energy E (expressed in 10^6 GeV) has a Larmor radius $r_L = 1.08E/(ZB)$ parsecs (see Reference [37]), and therefore more highly charged primaries are more tightly confined than light, less charged particles.

Reviews of cosmic-ray confinement in the galaxy can be found in References [41] and [42]. In the leaky-box model, cosmic rays propagate freely in a containment volume, with a constant escape probability per unit time. A diffusion equation for cosmic-ray creation and propagation can be written (see Reference [13], p. 117) that takes into account diffusion, energy loss or gain (by, say, ionization or acceleration), convection, a source term, losses of particles due to collisions and decay, and finally cascading processes such as nuclear fragmentation. The equation can be solved by neglecting energy gains and losses (assuming that acceleration has already taken place and is decoupled from propagation) and convection, and using experimental input such as fragmentation cross sections. The final result is that measured cosmic ray abundances of C and O and their spallation secondaries Li, Be and B on the one hand, and Fe and its spallation secondaries Sc, Ti, V, Cr and Mn on the other, can all be understood in terms of a single parameter λ, interpretable as an energy-

dependent mean distance traveled before escaping from the galaxy, and given by $\lambda = 10.8\beta(4/R)^{0.6}$ g/cm^2, where β is the particle's speed and R is the rigidity R = pc/Ze, p being the particle's momentum (the formula for λ above is valid for R > 4 GV). In the case of protons, for example, if feed-down from the breakup of heavier nuclei is neglected, the solution of the transport equation yields a primary flux proportional to $E^{0.6}Q(E)$ where Q(E) is the source spectrum. Since the observed differential spectrum is proportional to $E^{-2.7}$ (see Section 1.1), this model predicts that the source spectrum must be proportional to $E^{-2.1}$. Another prediction of the leaky-box model is that the escape length λ is rigidity-dependent, and proportional to $Z^{0.6}$; in other words, lighter primaries would get depleted sooner than heavier, more highly charged nuclei. If the knee in the primary spectrum is indeed due to leakage of primaries from the galaxy, it might therefore be expected that the composition becomes heavier at and above the knee. Unfortunately, one difficulty of the leaky-box interpretation is that each primary mass group has its own knee energy, and the overall knee should be somewhat smeared, whereas it appears to be rather sharp and well-defined (see Fig. 1.1).

At the highest direct measurements by JACEE of the proton component (see Fig. 1.3 and Reference [4]), a steepening of the spectrum has been observed, which could herald the onset of proton escape from the galaxy. However, this measurement needs to be confirmed and extended to higher energies. In Reference [43], a leaky-box calculation with a source spectrum proportional to $E^{-2.2}$ is found to yield differential spectra for C, O, Ne, Mg, Si and the Fe group that are in good agreement with the CRN and HEAO-3 measurements (References [20] and [18], respectively).

1.4.3 Acceleration at the knee

In both References [8] and [43] it is stressed that a summation of the experimentally measured spectra for the different mass groups agrees well with the independently

determined all-particle spectrum at energies up to about 10^5 GeV/nucleus (see also Fig. 1.3), but that extrapolations of the sum to higher energies yield a deficit compared to the all-particle spectrum. The reason for this could be that the source spectra change at higher energies, but an intriguing possibility is that a new source of cosmic-ray nuclei emerges. In Reference [44], it is predicted that at 10^7 GeV, and possibly up to 10^{10} GeV, a significant fraction of cosmic rays could originate in the central regions of active galactic nuclei (AGN). Here, the acceleration mechanism is a first-order Fermi process at a shock in an accretion flow onto a supermassive black hole. The predicted cosmic-ray spectrum from such a source peaks suggestively near the knee, and under certain assumptions a spectrum above the knee following a $E^{-3.0}$ power law is possible. Some experimental evidence even points to a "bump," or "knee-cap," an enhancement in the flux at the knee (see Reference [45]), which could be explained by this new component. In the AGN scenario, heavy primaries would be accelerated as well as protons, but entirely broken up into constituent nucleons in the central region of the AGN, so that the primaries observed in our galaxy from such a source would be entirely protons.

1.4.4 Acceleration above the knee

If heavy primaries are present in the cosmic-ray flux at energies above the knee, then the AGN scenario mentioned in the previous section cannot account for the entire flux. However, the diffuse first-order Fermi acceleration at supernova shocks that is successful at energies below the knee has a cutoff beyond which acceleration is not possible (see Section 1.4.1). Therefore other sources of high-energy particles are sought, typically in compact objects such as pulsars or X-ray binary star systems. A review of the topic can be found in Reference [46].

Enough energy is stored in the rotation of neutron stars at the core of supernova remnants that they are a potential site for high-energy particle acceleration. Particles

would be provided by the material ejected by the supernova, including heavy nuclei. Acceleration would occur at a shock front, such as at the interface between a shocked pulsar wind and the expanding ejecta from the supernova. This mechanism might accelerate particles up to about 10^8 GeV.

Another possible source is a close binary star system with a neutron star accreting matter from its companion; the gravitational energy released could be transferred to accelerating particles. There exist several mechanisms for this energy transfer to occur, some involving shocks similar to those mentioned above. One different mechanism is a dynamo effect, where the strong magnetic field lines from the neutron star intersect the accretion disk, giving rise to a $\mathbf{v} \times \mathbf{B}$ electric field capable of accelerating charged particles up to an estimated energy of a few times 10^7 GeV.

The short review of theoretical models of cosmic-ray creation, acceleration and propagation presented in this Section stresses that predictions abound for either light or heavy compositions at and above the knee, and that clear experimental input is required. We now briefly introduce the MACRO/EAS-TOP approach to the composition problem.

1.5 Simultaneous surface-underground studies

The discussion of the previous two Sections is not meant to be exhaustive, but to illustrate the fact that the primary mass composition at energies around and above the knee is still somewhat controversial and not really known. Conflicting indirect experimental evidence for either light or heavy compositions exist, whereas theoretical models are capable of explaining either instance. Increasingly, it has become recognized that it is highly desirable to measure as many air shower parameters simultaneously as possible, on an event-by-event basis. For example, the combination

of electromagnetic air shower measurements at the ground surface with simultaneously detected deep-underground muons can provide, event-by-event, a total surface shower size (and therefore an estimate of the primary energy), an underground muon multiplicity and lateral distribution, and a double estimate of the direction of the primary. Extensive use of Monte Carlo simulations is still required in comparing distributions with those obtained with various primary composition models, but the availability of more parameters can help in reducing the systematic uncertainties this involves. Besides, the uncertainties introduced in comparing a given muon multiplicity to simulations from primaries with energies spanning orders of magnitude are reduced, as it now becomes possible to group the data in various bins of surface shower size, corresponding to various bins of primary energy. If, moreover, the underground detector is large enough to contain large multiplicity events, the multiplicity bias introduced by the finiteness of the detector is reduced and sensitivity to composition is improved. Finally, composition studies based on underground muon data or surface shower size measurements alone are reliant on calculations of absolute event rates, which depend on the primary energy spectra utilized and are subject to possible normalization errors in the Monte Carlo calculations; on the other hand, a distribution of deep underground muon multiplicities as a function of simultaneous surface shower sizes (or equivalently primary energies) is independent of absolute rates and insensitive to normalization errors.

The combination of deep-underground muon information with surface air shower measurements was performed as early as 1952 (see Reference [47]), although the primary energy window aimed at then has since been investigated directly with balloons and satellites. The Baksan underground muon telescope (mentioned above) and the Soudan detector are two examples of modern, deep detectors with some surface shower measurement capability. In Reference [48], coincident underground muons detected by the Soudan 1 detector and surface measurements are used to

compare with predictions from a light and heavy composition models at energies between 10^4 and 10^7 GeV, and a light composition is found to agree best with the data. However, this result was obtained with an underground detector of area 9 m^2, a surface detector of dimension 36 m^2 and a live time of 80 days. In Reference [49], preliminary results from coincident measurements between Soudan 2 and a surface detector are reported. The underground area for this work was about 80 m^2, the surface area 40 m^2 and the live time only 50.4 hours, and no composition determination is presented. The LVD detector at the Gran Sasso Laboratory is capable of detecting and reconstructing deep-underground muons in coincidence with the EAS-TOP surface array, and a feasability study is presented in Reference [50], but no composition study has yet been performed.

The situation of the MACRO underground detector and the EAS-TOP extensive air shower array is described in the remainder of this thesis, but for purposes of comparison, suffice it to mention here that the effective area of MACRO (in the configuration used in this thesis) is 288 m^2, the sensitive area of EAS-TOP is about 10^5 m^2 and the live time for the analysis presented here is 96 days, and therefore corresponds to an unprecedented scale for this type of study. The range of primary energies investigated by this experimental arrangement is from a few times 10^3 GeV (due to the requirement of penetrating TeV muons being created in the air shower to trigger MACRO), up to above the knee. Therefore the setup is well suited for composition studies, as it overlaps the lower energy region where the composition has been directly determined, which allows for calibration and tuning of the simulations, and it extends past the knee where so little is known, but where so much stands to be learned.

Chapter 2

The MACRO Experiment

In this chapter, we first describe the general features and components of the general-purpose MACRO experiment, mentioning in passing various physics topics that it investigates. Then we concentrate on its streamer tube system, a detector component of crucial importance to the primary composition studies performed in coincidence with EAS-TOP. After a physical description and analysis of the operational characteristics of the streamer tube system, we describe how it is used to reconstruct muon tracks through the detector. Finally, we present some distributions of quantities related to muon physics, some of which will be needed in further chapters.

2.1 Description of the detector

2.1.1 Detector location and generalities

MACRO (**M**onopole, **A**strophysics and **C**osmic **R**ay **O**bservatory) is a large, deep underground detector located at the Gran Sasso National Laboratory (see Reference [51]) in central Italy, under a mountain range including Monte Aquila and the Gran Sasso d'Italia, part of the Apennine range. Fig. 2.1 shows a map of central Italy and the location of the Gran Sasso Laboratory, excavated next to a highway tunnel

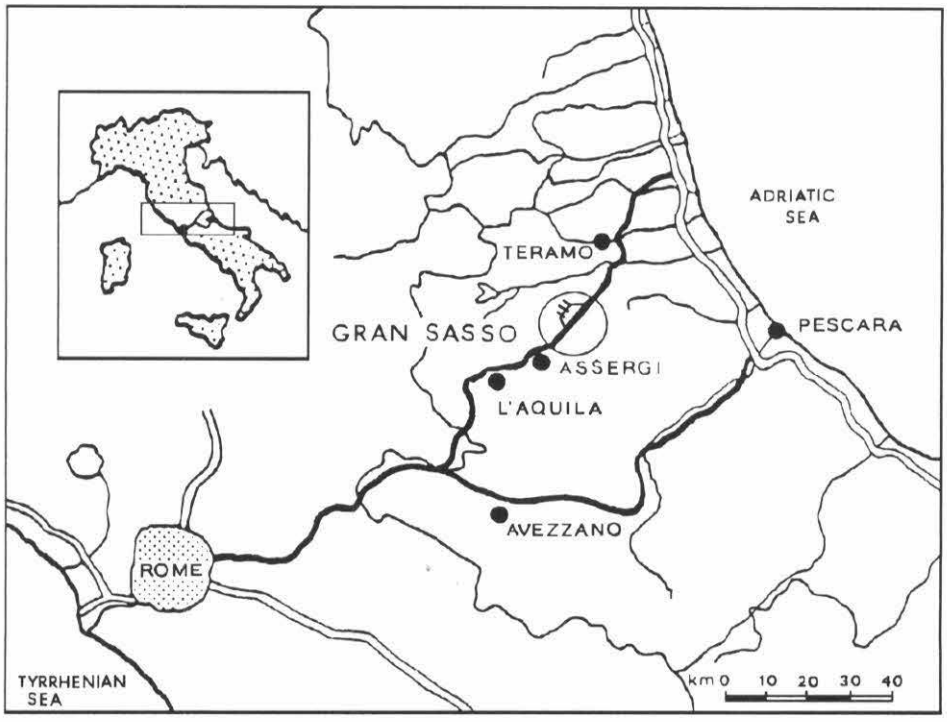

Figure 2.1: Map of central Italy showing the location of the underground Gran Sasso Laboratory (inside the circle), about 100 km northeast of Rome.

crossing the range, about 100 km northeast of Rome. Fig. 2.2 shows the layout of the Laboratory, with MACRO in Hall B. The underground laboratory, developed by the Istituto Nazionale di Fisica Nucleare (INFN), lies under a minimum rock overburden of about 1180 m, or about 3200 m.w.e. (meters of water equivalent). The mean rock density above the laboratory is (2.71 ± 0.04) g/cm^3.

As is pointed out in Reference [22], the depth of the Gran Sasso Laboratory is well suited for studies of the primary cosmic ray composition using high-energy muons, being great enough that the corresponding primary energy range of detected events is around and above the "knee" of the primary spectrum (see Fig. 1.1), but small

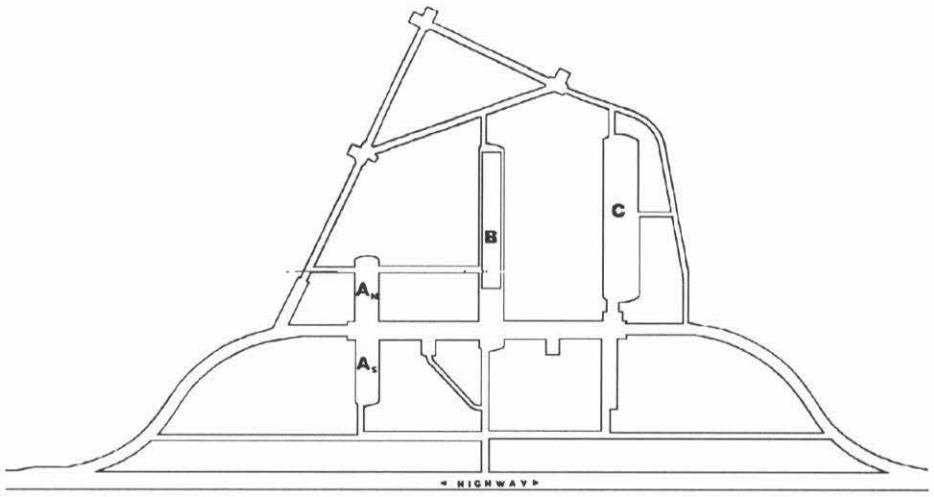

Figure 2.2: Layout of the Gran Sasso Laboratory showing one of the twin highway tunnels and the three underground Halls. MACRO is represented by the rectangle in Hall B.

enough that the rate of muon events is not prohibitively low. Indeed, the minimum muon energy at the ground surface required for a muon to traverse the mountain is about 1.4×10^3 GeV, corresponding to a primary energy of at least about 3×10^3 GeV (single muon) or 2×10^4 GeV (multiple muons). We will return to muon rates in Section 2.3.1.

2.1.2 Detector description

The detector is a large rectangular parallelepiped, 9 m-high, 12 m-wide and 72 m-long, as shown in Fig. 2.3. Its structure is modular, the basic unit, called "supermodule", being 9 m-high, 12 m-wide and 12 m-long. The six supermodules are instrumented and operated in three pairs, allowing for continuous operation of at least some part of the detector, while some other part is undergoing construction,

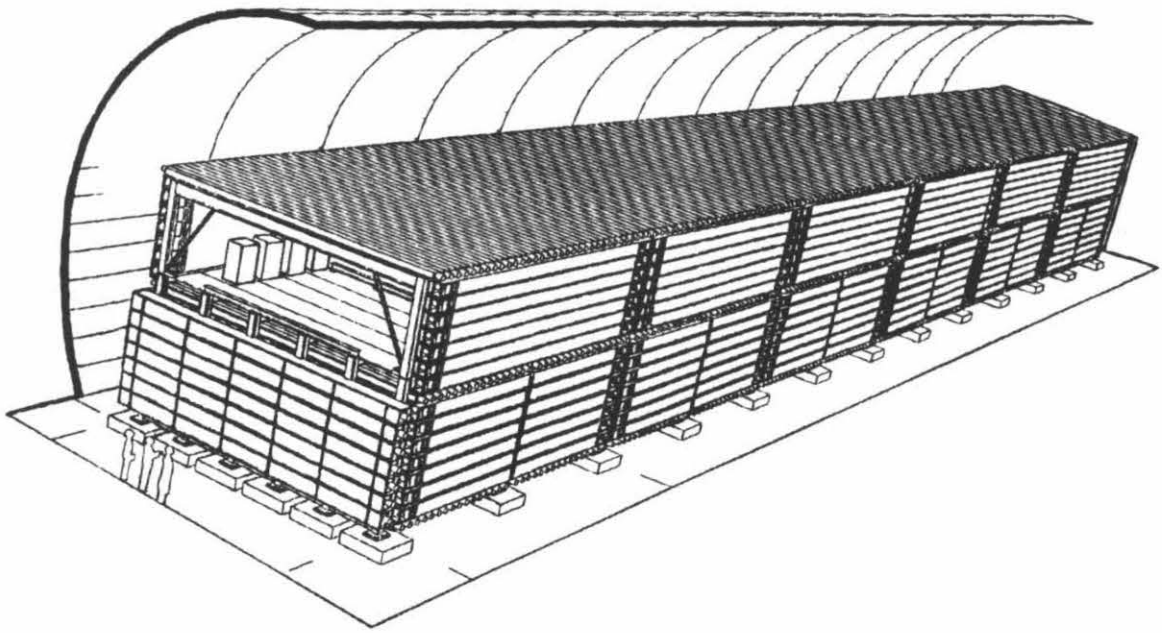

Figure 2.3: Perspective drawing of MACRO showing all six supermodules. The upper half of the detector (called the "attico") is hollow and contains the racks of electronics.

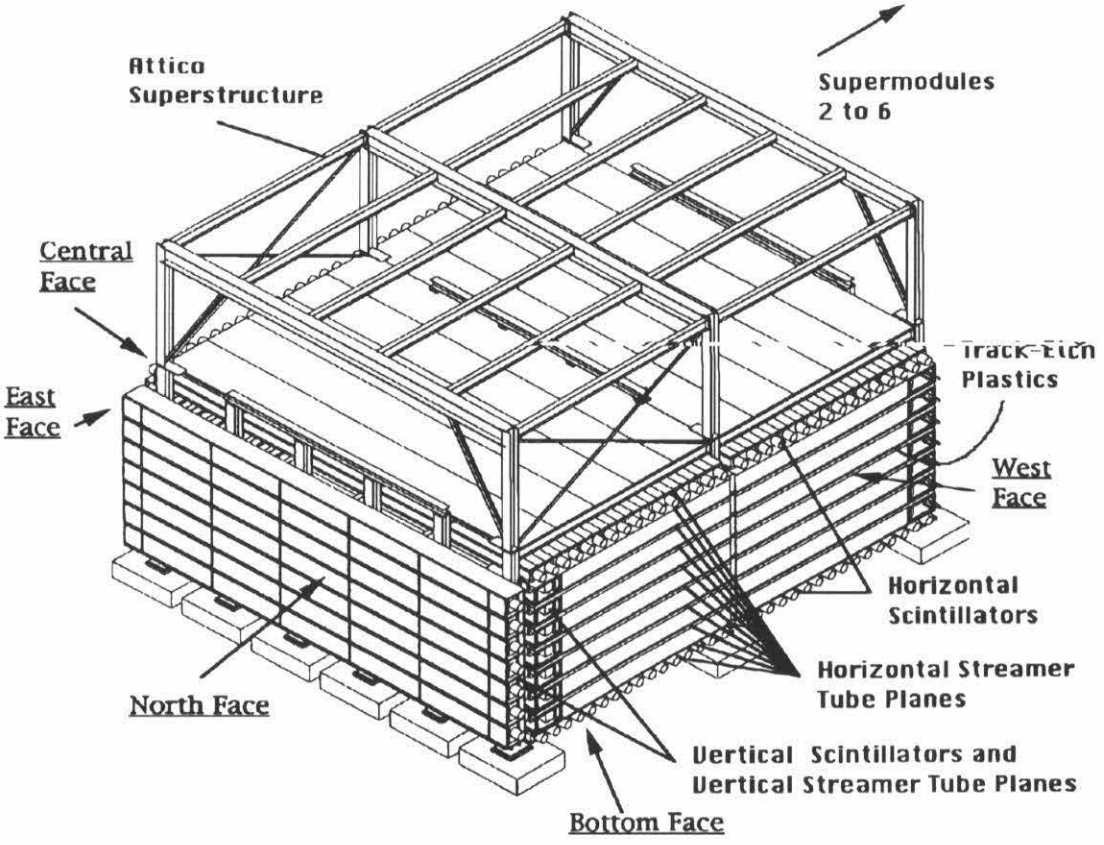

Figure 2.4: Perspective view of supermodule 1 before installation of the attico.

maintenance or calibration. Each supermodule consists of a lower part (4.8 m-high), and an upper, hollow part called "attico" (Italian for "attic"), inside of which resides the electronics for data acquisition. Fig. 2.4 is a perspective line drawing of supermodule 1 (with only the attico superstructure), and Fig. 2.5 schematically shows a cross-sectional end view of the lower part of one supermodule.

As described in detail in Reference [52], and as shown in Figs. 2.4 and 2.5, the three detector components are liquid scintillation counters, streamer tubes and plastic track-etch modules.

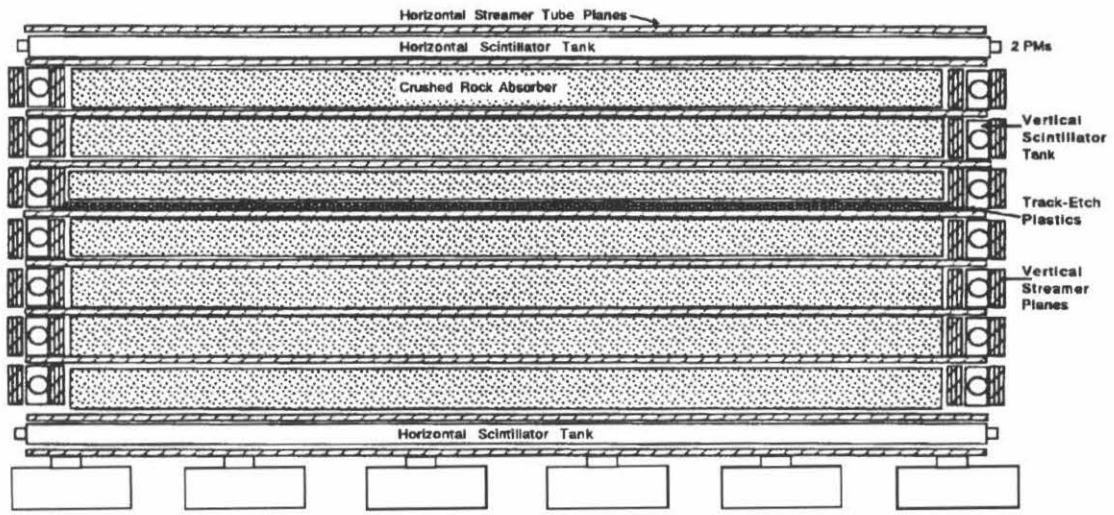

Figure 2.5: Schematic cross-sectional view of the lower half of one supermodule.

The liquid scintillation counters are of two types: horizontal counters (dimensions 75 cm $\times$ 26 cm $\times$ 1190 cm) and vertical counters (dimensions 23 cm $\times$ 49 cm $\times$ 1160 cm). For each supermodule, the horizontal scintillation counters are arranged in three layers of 16 counters each (the Bottom and Central faces of Fig. 2.4; the Top face would appear at the top of the attico) and the vertical scintillation counters are arranged in two layers of 14 counters each (the West and East faces of Fig. 2.4). In addition, supermodules 1 and 6 are each equipped with one extra vertical layer of 7 counters to partially cover the ends of the detector (the North face of Fig. 2.4 is an example). The counters are made of 0.63 cm-thick PVC, lined on the inside with a white vinyl-FEP material. They are composed of one main chamber at the center (1120 cm-long) separated from two small chambers at the ends by two transparent PVC windows. The main chamber is filled (up to a height of about 19 cm and 43 cm for horizontal and vertical counters, respectively) with a mineral-oil-based liquid

scintillator mixture (96.4% mineral oil, 3.6% pseudocumene, 1.44 g/l of PPO and 1.44 mg/l of bis-MSB), and the end chambers are filled with pure mineral oil, for improved optical coupling with the central chamber. Scintillation light from the passage of a charged particle propagates from the main chamber to the end chambers by total internal reflection at the scintillator/air and scintillator/FEP-lining interfaces. The attenuation length of the mineral oil base is in excess of 20 m at the wavelength of the scintillation light (about 425 nm), for a resulting attenuation length of about 12 m for the scintillator mixture. The end chambers are equipped with 20 cm-diameter hemispherical photomultiplier tubes, two per end (four per counter) for the horizontal counters, and one per end (two per counter) for the vertical counters. Light collection reflectors surround the phototubes to improve the light collection efficiency. Anode signals from the phototubes are used in various trigger configurations, and TDC, ADC and waveform data are recorded to obtain particle location within a counter (from time differences at the two ends), particle velocity (from transit time between layers, or from pulse duration within a counter for very slow particles) and energy deposition. We will return briefly to the scintillator system in Section 2.1.3, but will not dwell much on this detector component since it is not used in the study of MACRO/EAS-TOP coincident events.

The streamer tube system is used to track charged particles through the detector. Like the scintillation counters, the streamer tubes are arranged in horizontal and vertical planes. The tubes are built and installed in groups of eight, *i.e.*, eight tubes are formed from a single chamber (of dimensions 3.2 cm $\times$ 25 cm $\times$ 12 m) made of 1.5 mm-thick PVC, with each of the eight cells inside of cross-sectional dimensions 2.9 cm $\times$ 2.7 cm (see Fig. 2.6). For the lower part of each supermodule, the streamer tubes are arranged in ten horizontal planes of twenty-four 8-tube chambers each, and twelve vertical planes of fourteen 8-tube chambers each (for the upper part, the vertical streamer tube structure of the lower part is essentially repeated, and

the horizontal streamer tube structure consists of four planes, two above and two below the top layer of scintillation counters). The lower two and upper two horizontal planes sandwich the horizontal scintillation counters. The inner eight planes of streamer tubes are separated by seven layers of crushed rock absorber (see Fig. 2.5), each about 60 g/cm^2-thick. The vertical streamer tube planes sandwich the vertical scintillation counters, with three planes on each side of every counter. The North face (supermodule 1) and South face (supermodule 6) have, in addition, six planes of fourteen 8-tube chambers each, sandwiching the vertical scintillation counters. We will return to streamer tubes in more detail in Section 2.2.

The track-etch component of the detector consists of three 0.2 mm-thick layers of LEXAN, one 1 mm-thick layer of aluminum absorber and three 1.4 mm-thick layers of CR39, all sandwiched together in modules of dimensions 25 cm $\times$ 25 cm and arranged in one horizontal layer near the center of the lower half of the detector (another layer, vertical, is in the process of being added). In each supermodule, this horizontal layer contains 48 rows of 47 such track-etch modules. The track-etch arrangement is designed to passively record the passage of a slow, heavily-ionizing particle, which damages the material along its trajectory. The track is revealed by chemical etching of the plastics and subsequent examination with a microscope. This component of the detector is not used in the study of MACRO/EAS-TOP coincidences, and will therefore not be elaborated upon any further here.

At the time the data analyzed in this thesis were collected (1990), supermodules 4 to 6 were under construction, and construction of the attico had not yet begun. Therefore only the streamer tubes for supermodules 1 and 2, and only the scintillation counters for supermodule 1 were operational.

2.1.3 The physics of MACRO

MACRO is designed as a general-purpose detector, with much redundancy, optimized for the study of rare phenomena. The thick scintillators are well suited for a large scale search for slowly moving, heavily ionizing GUT magnetic monopoles and other exotic particles (such as nuclearites). The track-etch system provides an independent means of searching for the same particles. The streamer tubes allow us to expand the sensitivity for such searches to high velocities. References [53] and [54] are reports of searches for monopoles and nuclearites conducted so far.

The large amount of scintillator in the detector (about 600 metric tons, with a potential upgrade to 1000 tons) provides for excellent sensitivity to neutrino bursts from gravitational stellar collapse within the galaxy, where a $\overline{\nu}_e$ is detected via the reaction $\overline{\nu}_e + p \rightarrow n + e^+$. A search for such neutrino bursts has been conducted and reported in Reference [55].

The large area and good resolution of the tracking system (see Section 2.3) make the detector well suited for studying cosmic ray muons. For example, References [56] and [57] report on an all-sky survey of muon directions in a search for point sources of high-energy cosmic rays and for anisotropies in their arrival direction distribution. In Reference [58], the structure of muon event times of occurrence is studied. Timing from the scintillator system allows the unambiguous discrimination between downward-going muons from standard cosmic ray primaries and upward-going muons from neutrino interactions in the rock below the detector. The latter events are studied in searches for neutrino point sources and as a signature for WIMP-$\overline{\text{WIMP}}$ annihilation at the center of the Earth or the Sun (reports are in preparation). The primary mass composition at very high energies is studied through the multiplicity distribution of multimuon events (see Reference [23]), and through their decoherence function (see Reference [59]).

Finally, the combination of deep underground muon information with surface

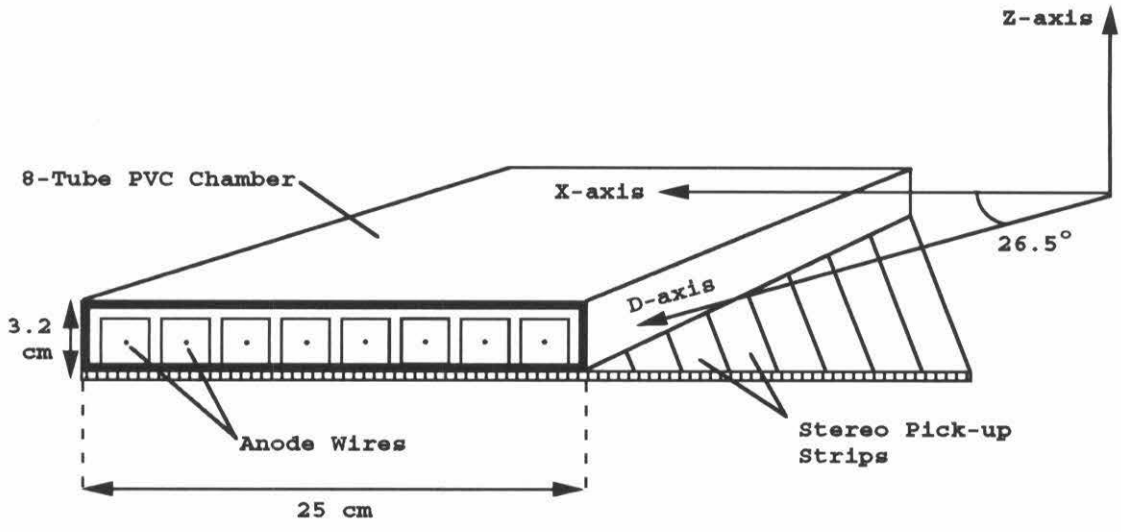

Figure 2.6: Configuration of the streamer tubes, showing a short length of one 8-tube chamber with the stereo pick-up strips underneath.

electromagnetic shower data can be used to study the mass composition of primary cosmic rays at ultrahigh energies. This is the topic of References [60] and [1], and of this thesis.

2.2 Streamer tube characteristics

The general structure and arrangement of the streamer tubes used in MACRO was described in Section 2.1.2. In this section, we return to them in more detail. A thorough description can be found in Reference [52].

Fig. 2.6 shows a short length of one 8-tube chamber, together with the aluminum stereo pick-up strips (see below). Three walls of every cell (or tube) inside a PVC chamber are coated with low-resistivity graphite ($\leq 1 k\Omega$/square) and act as a cathode, while the fourth wall is made of 1.5 mm-thick PVC. The graphite cathode

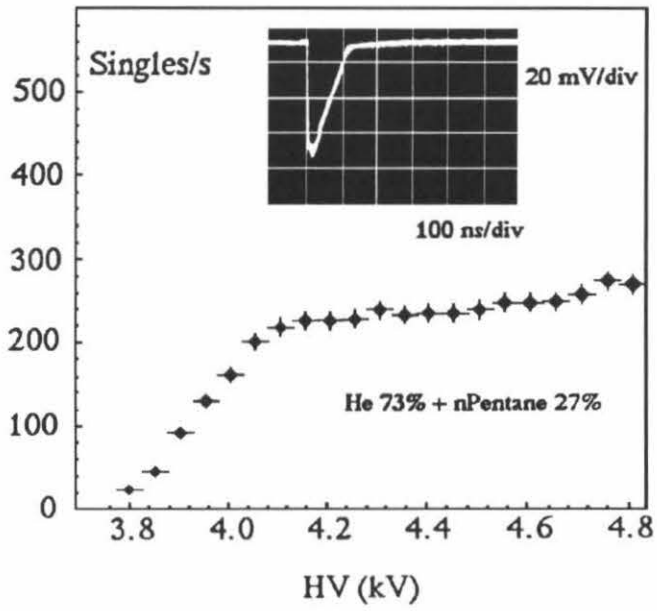

Figure 2.7: Measured singles' rate as a function of high voltage for a 50 cm-long streamer tube test chamber with the gas mixture used. The insert shows a typical wire pulse (with 50 Ω termination).

is grounded. The central, 12 m-long, anode wire is made of silvered beryllium copper and has a diameter of 100 μm. The characteristic impedance of each streamer tube is 330 Ω, and it has a propagation time of about 3.3 ns/m. It is supported every meter by plastic inserts inside the cell.

The two ends of each 8-tube chamber are carefully sealed, and a helium (73%) – n-pentane (27%) gas mixture flows through it, at a rate of one complete volume change per five days. This gas mixture results in a wide range of anode high voltages within which the tubes perform at high efficiency, with low noise, as can be seen in Fig. 2.7, where the singles' rate as a function of high voltage is plotted for a streamer tube test chamber. Specifically, over a 700 V-wide plateau, very weakly-ionizing particles can trigger a streamer (with a measured efficiency of about 20% for single ionization electrons; see Reference [61]). The signal rate is dominated by ionizing particles from radioactive decays. Due to the special care taken in building the detector with low-radioactivity materials, this rate is about 40 Hz/m^2. The anode wires are kept at a high voltage of about 4.5 kV, near the center of the singles' plateau.

External pick-up strips are placed against the insulating PVC wall of the horizontal streamer tube cells, at an angle of 26.5° with respect to the wires (see Fig. 2.6). They pick up the streamer signal through the resistive cathode technique of Reference [62]. The strips provide a second coordinate for a two-dimensional reconstruction of the position of a charged particle traversing a streamer tube plane (the other coordinate being provided by the anode wires of the tubes). The strips are 3.1 cm-wide, 40 μm-thick ribbons of aluminum, laid on 1 mm-thick sheets of PVC, with a 40 μm-thick sheet of aluminum on the underside of the latter (grounded to provide a reference electrode). The strips are of varying lengths, being laid diagonally across a rectangular area, and therefore have varying, but high, readout efficiencies (97% for strips longer than 7.5 m and 100% for shorter ones, at a threshold setting of 1.8 mV). For the lower half of each supermodule, only horizontal streamer tubes are equipped

with stereo strips. Each vertical streamer tube plane provides only a one-dimensional reconstruction of the particle's location. The so-called X-view is that obtained by looking at the detector along the wires, and the D-view is that along the strips.

Signals from the wires and strips are read out by electronic cards mounted directly on the streamer tubes and strips. On the wire readout cards, the wire pulses from eight tubes of a chamber are discriminated, amplified, OR-ed together for triggering purposes (and also OR-ed with signals from other 8-tube chambers on the same plane – horizontal or vertical), and also read out through parallel-in, serial-out shift registers, as a pattern of hits and misses. The strips are similarly read out.

2.3 Muon triggers and track reconstruction

2.3.1 Muon triggers and rates

The OR signals from the streamer tube wire readout cards are input to a trigger circuit which analyzes the pattern of planes hit to make a trigger decision. For the lower half of each supermodule, ten OR signals are provided by the horizontal planes and six OR signals are provided by each of the West and East face vertical planes.

The triggering condition programmed into the circuit is the following:

(Majority coincidence of 6 out of 10 horizontal planes) OR
(Majority coincidence of 5 out of 8 contiguous horizontal planes, excluding 1st and 10th planes) OR
(3/10 horizontal AND 3/6 vertical East planes) OR
(3/10 horizontal AND 3/6 vertical West planes) OR
(3/6 vertical East planes AND 3/6 vertical West planes) OR
(5/6 vertical East planes) OR
(5/6 vertical West planes) OR

(For supermodules 1 and 6, six additional OR signals exist for the North or South

face vertical planes, but at the time the data pertaining to this thesis were collected they had not yet been inserted in the triggering scheme, although North face signals were read out.) The measured rate corresponding to this trigger configuration (for two supermodules) is (454 ± 1) events/hour. The uncertainty given on this as well as other rates in this section is that on the mean rate; the distribution of rates is approximately Gaussian (more accurately, a sum of Gaussians), with a RMS of about 60 events/hour.

In addition to the muon trigger provided by the streamer tube system, three fast particle triggers are provided by the scintillator system, based either on time differences between signals recorded in different planes of scintillation counters, or on the characteristics of the signals recorded at the two ends of any single counter. The measured total rate from the scintillator triggers (for two supermodules) is (277 ± 1) events/hour, 54% of which have also triggered the streamer tube system.

The offline criterion used for pre-selecting MACRO muon events in searching for time-coincidences with EAS-TOP events (see Chapter 4) is that at least four horizontal streamer tube planes have recorded hits in both the wire X-view and the strip D-view, regardless of trigger type, and that in each view the hits are lined up well enough to fit a straight-line track with a reasonable χ^2. This criterion results in an event rate of (379 ± 1) events/hour, 97% of which have triggered the streamer tube muon system and 3% of which have triggered the scintillator system but not the streamer tube system (these are mostly events which entered or exited the active two-supermodule volume through the North face of supermodule 1 or the South side of supermodule 2, such that only four or five horizontal streamer tube planes were hit).

The average dead time, due to the acquisition system, is about 0.6%.

2.3.2 Track reconstruction

Track reconstruction in three dimensions is performed by a software package called DREAM (**D**ata **R**eduction and **E**vent **A**nalysis for **M**ACRO). This package reconstructs tracks independently in each of the wire X-view and strip D-view by first identifying aligned hits from different planes, and then fitting a straight line through these hits to obtain a slope and an abscissa, and uncertainties on these parameters. Particular care is taken to identify and reconstruct multiple tracks for multi-muon events, where each track is treated separately, without parallelism requirements. When more than one track are reconstructed in either view, the slopes and abscissae are averaged for that view. The X and D slopes are combined with the 26.5° stereo angle between the wires and strips to obtain the spherical polar angles θ (zenith) and ϕ (azimuth) of the average track in space, where θ is measured from the local vertical and ϕ is measured counterclockwise from true North (see Fig. 4.15). The X and D abscissae and slopes are used to calculate the point of intersection (x,y) of the track with the floor of Hall B, where the x-axis is parallel to the longest dimension of the apparatus.

A "hit" on a streamer tube plane, used in reconstructing the track(s) in each view, is in reality a cluster of adjacent streamer tube channels which fired. Indeed, whereas a single particle traversing a streamer tube plane travels in general through only one streamer tube cell (or perhaps two if the track is inclined), adjacent cells often fire also, due to electromagnetic radiation accompanying the particle. Muons reaching the detector have an average energy of 180 GeV, close to the critical energy of about 500 GeV around which e^+e^- pair creation and bremsstrahlung become comparable to ionization as mechanisms for energy loss (see Reference [63], p. III.17). Fig. 2.8 shows an example of a single muon event, in both the X and D views, together with the tracks reconstructed by DREAM. The wide clusters of hits are evidence of electromagnetic shower activity accompanying the muon. The average cluster

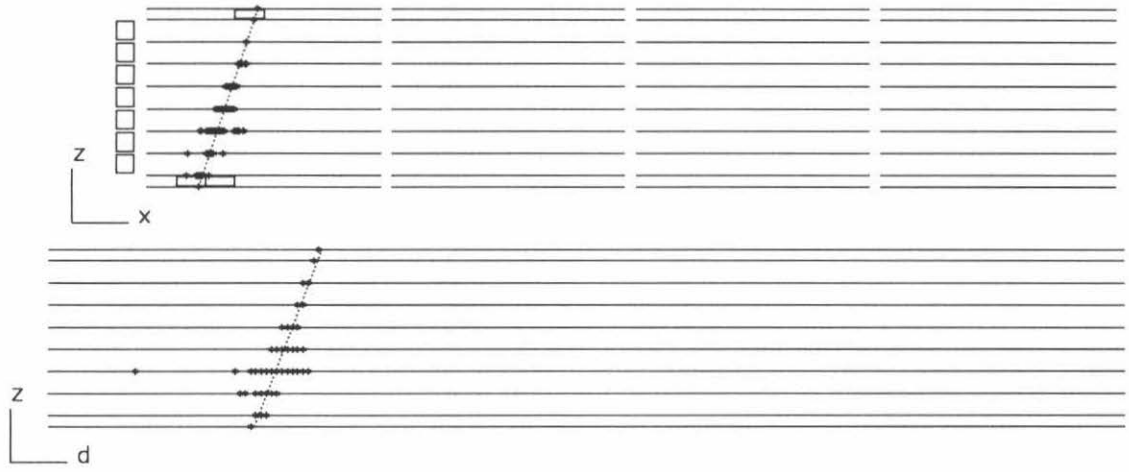

R= 2114 E= 1894 21-JUL-90 18:21:43 HT= 0000-0000-0000-3223 ST= 3 M= 1

Figure 2.8: Example of a single muon event, showing the X and D views of two supermodules and the tracks reconstructed by the DREAM package. This event shows some electromagnetic shower activity as clusters of hits along the track.

width for the wires is 4.50 cm, or 1.45 streamer tube cells. For strips, the induced signal is 8.96 cm-wide, on average, or 2.75 strips-wide. The residuals obtained by subtracting the position of the fitted track across a plane from the center of the cluster of hits on that plane are Gaussian, with a mean consistent with zero and a RMS of 1.1 cm in the wire view, and 1.6 cm in the strip view (compared with the predicted $4.5/\sqrt{12} = 1.3$ cm and $8.96/\sqrt{12} = 2.6$ cm one would obtain by assuming that the actual location of the hit is uniformly distributed over the width of the cluster). The cluster widths and track lengths determine the instrumental angular resolution to which muon directions can be reconstructed. The average uncertainties on the slopes for tracks with at least four planes hit are 0.14° in the X-view, and 0.29° in the D-view; the result of these is that 68% of muons have reconstructed directions within 0.4° of the true direction underground.

2.4 Some distributions of interest

In this section we present a few distributions related to MACRO, some of which will be useful in further chapters.

It is interesting to plot the distributions of angular directions of recorded muons, as such distributions reflect the shape of the mountain above the detector. Fig. 2.9 shows a distribution of the cosine of the zenith angle of recorded muon tracks, and Fig. 2.10 shows that of azimuth angles for the same events. These distributions are a negative map of the mountain thickness: a peak in the distribution (higher muon rate) corresponds to a direction of smaller rock thickness, and a valley in the distribution to a direction of greater thickness. Were the ground above MACRO flat, the $\cos\theta$ distribution would peak at 1., *i.e.*, the greatest observed muon rate would come from the zenith, where rock would be thinnest. However, the detector sits under a mountain, so that the direction of minimum rock thickness has a $\cos\theta$

of about 0.9. On both figures are indicated the angular range subtended by the effective area of the EAS-TOP air shower array (dotted arrow), as well as the area of the inner part of EAS-TOP corresponding to showers with the core within the array (solid arrow). We will mention these distributions again in Section 4.2.2 when we compare the reconstructions of coincident events by MACRO and EAS-TOP.

Muon multiplicity is the essential quantity studied in the composition problem. Fig. 2.11 shows a distribution of muon multiplicities observed with two supermodules in 1195 hours of live time (see Reference [23] and Table 4.3). In the case of events with large multiplicities, it is not always possible to unambiguously determine the number of tracks in the streamer tubes, due to a large number of hits. When this is the case, the largest and smallest multiplicities consistent with the activity in the event are estimated, and an equal fractional weight is assigned to each multiplicity in the range so defined (hence some non-integer numbers of events). The mean multiplicity is 1.06 ± 0.02, with a 19:1 ratio of single to multiple muon events. Error bars on the figure include statistical uncertainties as well as some estimated systematic uncertainties due to a visual scanning procedure. This distribution will be of use in Section 4.3.1, when we compare muon multiplicities for MACRO as a standalone detector with multiplicities for events simultaneously recorded by EAS-TOP at the ground surface.

In equating the direction of a primary cosmic ray to that of the deep-underground muons that result from it, an uncertainty is introduced because of the long series of intermediate phenomena involved, starting with the initial (and possibly subsequent) hadronic interaction(s) high up in the atmosphere followed by meson decay, muon propagation in the air and rock and finally detection underground. It is interesting to study such angular considerations to understand the absolute pointing ability of MACRO, as well as the relative pointing of MACRO and EAS-TOP. Fig. 2.12 shows a calculated distribution, that of angular deviations ξ from the primary axis of high-

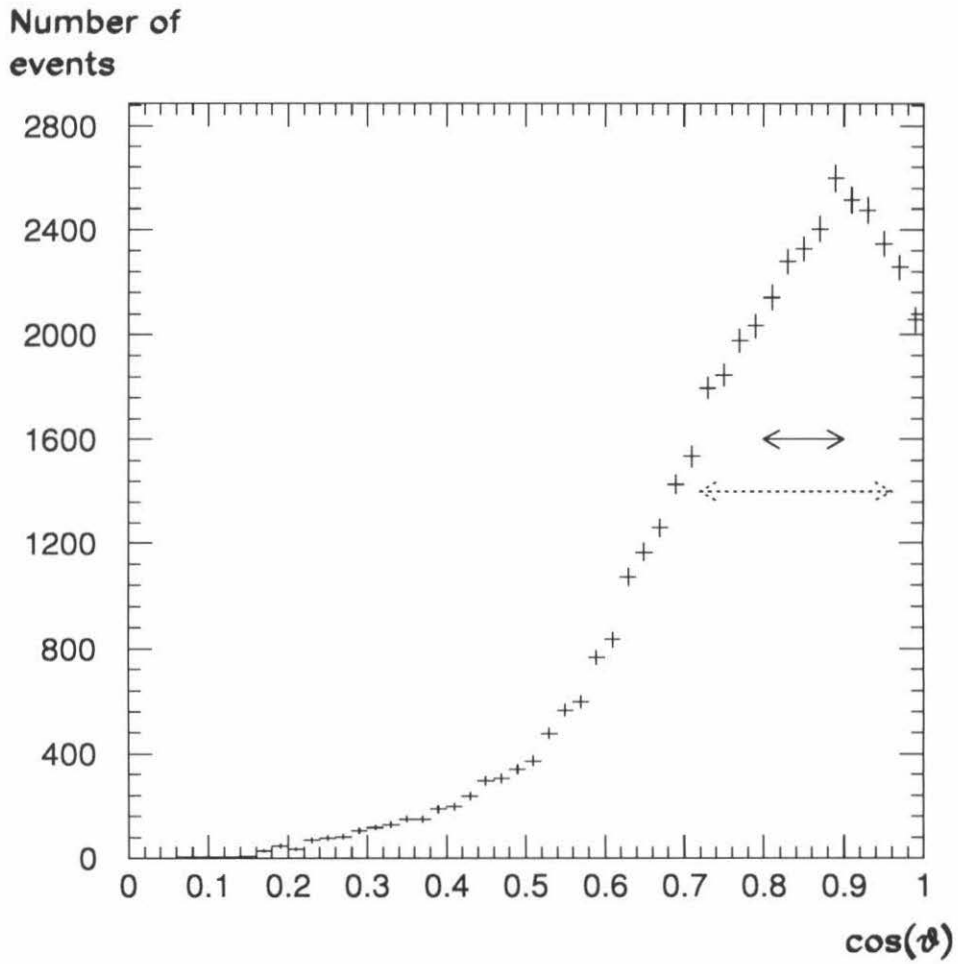

Figure 2.9: Distribution of the cosine of the zenith angle θ of recorded muon tracks. The dotted arrow shows the zenithal angular range subtended by the effective area of EAS-TOP (see Chapter 3) at MACRO, and the solid arrow shows that subtended by the inner area of EAS-TOP defining internal events.

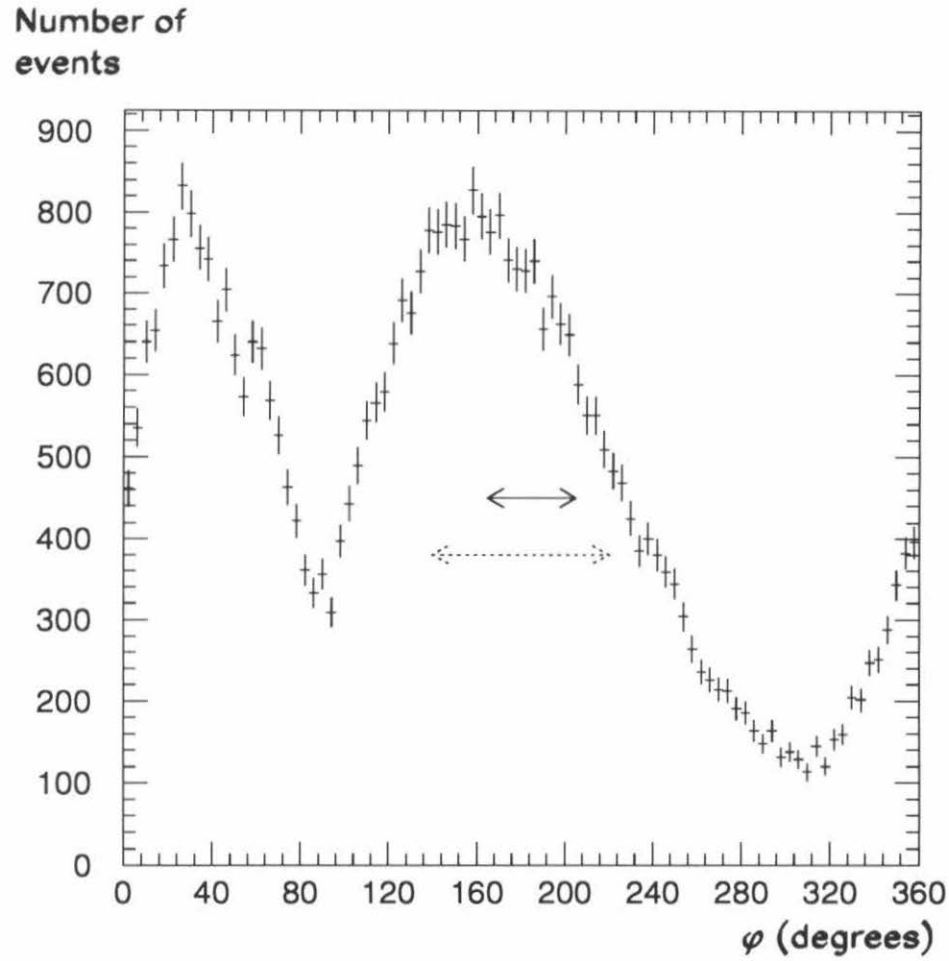

Figure 2.10: Distribution of the azimuth angle ϕ of recorded muon tracks. The dotted arrow shows the azimuthal angular range subtended by the effective area of EAS-TOP at MACRO, and the solid arrow shows that subtended by the inner area of EAS-TOP defining internal events.

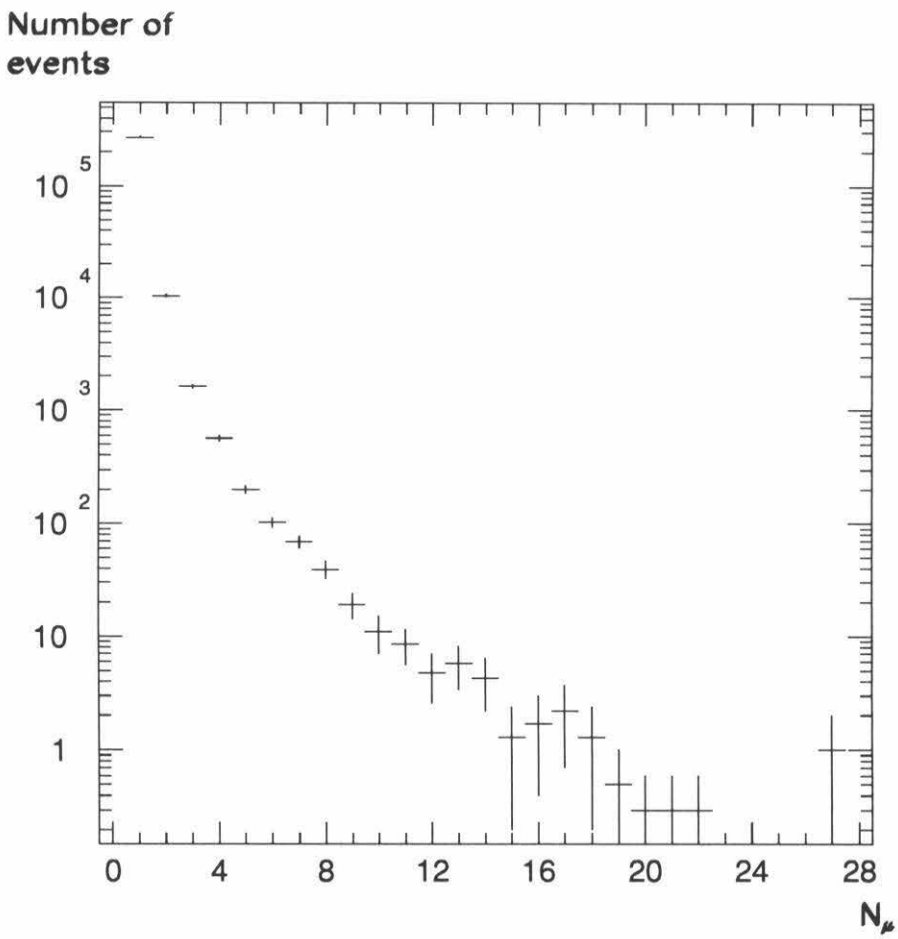

Figure 2.11: Muon multiplicity distribution recorded with two supermodules in 1195 hours of live time (see Reference [23]). The mean multiplicity is 1.06 ± 0.02.

energy muons deep underground. The muons are simulated using the HEMAS Monte Carlo code described in Chapter 5. This distribution is that obtained for proton primaries with energies and incidence directions relevant to the MACRO/EAS-TOP situation (these statements will be made quantitative in Chapter 5). The calculated mean deviation from primary axis is $(0.366 \pm 0.002)^\circ$. The pointing accuracy of the detector within its reference frame, or the accuracy with which the parent direction can be estimated from that of the muon, is obtained by convoluting this mean deviation with the detector resolution of about 0.4° mentioned in Section 2.3.2. This is done with a Monte Carlo calculation and yields a resolution of about 0.5°. The same result is obtained by adding the two effects in quadrature.

As a verification of this calculation, in Fig. 2.13 we show an experimental distribution, namely, that of the angular separation χ measured between the two muons of dimuon events, for events with a mean zenith angle satisfying $0.8 < \cos\theta < 0.9$, the range of zeniths relevant to the direction of the inner part of EAS-TOP seen by MACRO (see Fig. 2.9). The experimental distribution has a mean of $(0.74 \pm 0.02)^\circ$. This is in agreement with a simple Monte Carlo calculation, in which two tracks are allowed to scatter by 0.366° each (from Fig. 2.12), and then by 0.4° each (from the detector resolution of Section 2.3.2), and which results in a mean two-muon angular separation of 0.7°.

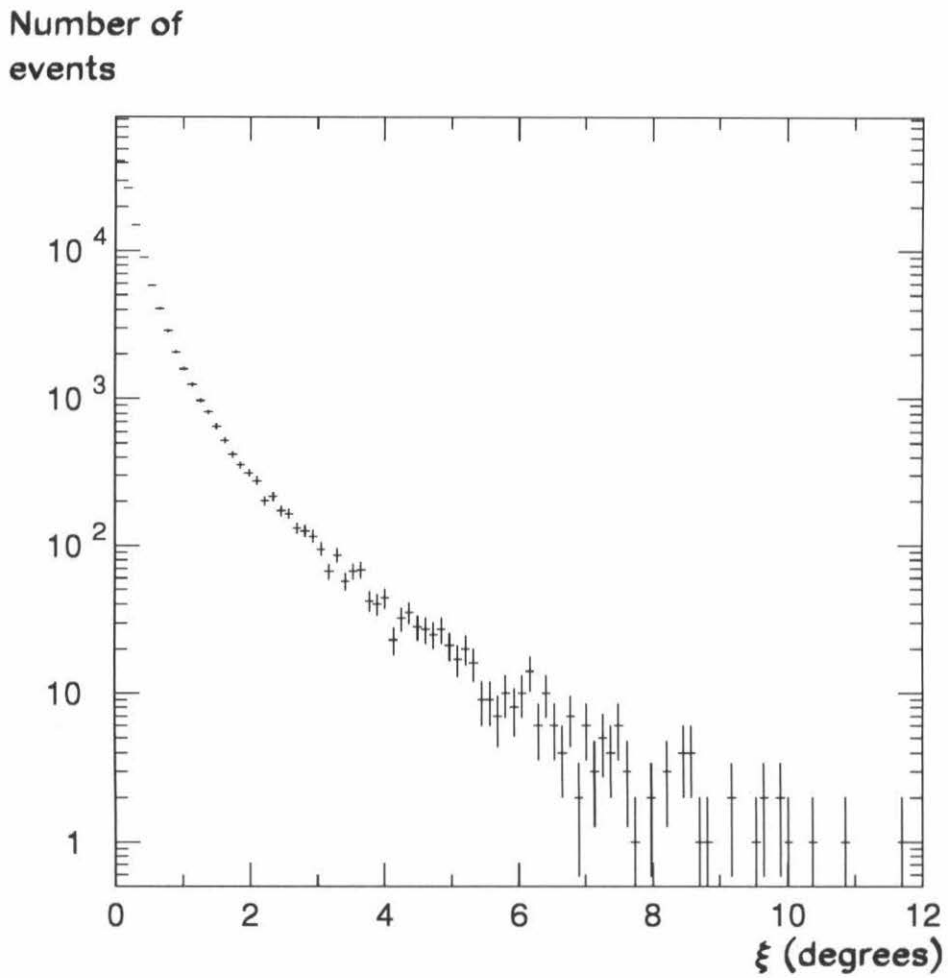

Figure 2.12: Distribution of angular deviations ξ from shower axis deep underground, for high-energy muons simulated using the Monte Carlo code described in Chapter 5. The mean deviation is $(0.366 \pm 0.002)°$.

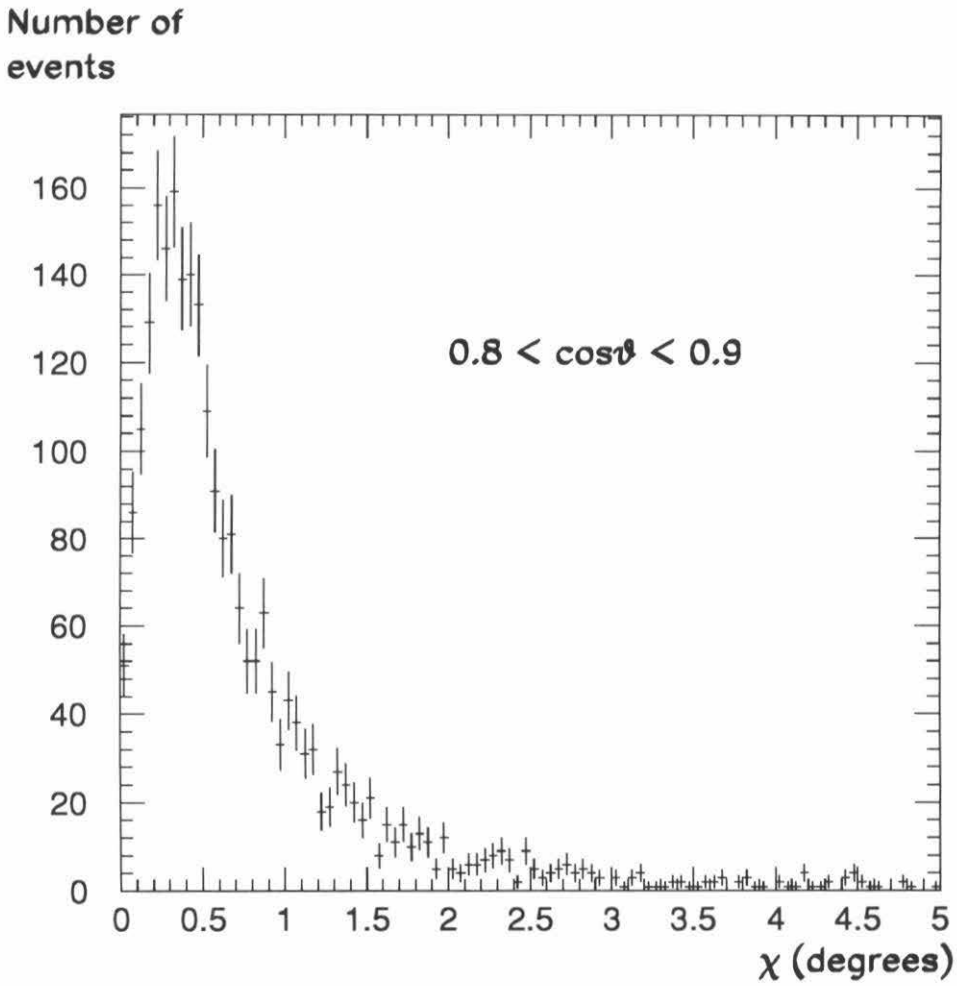

Figure 2.13: Distribution of angular separations χ between the two muons of dimuon events with a mean zenith angle satisfying $0.8 < \cos\theta < 0.9$. The mean separation is $(0.74 \pm 0.02)°$.

Chapter 3

The EAS-TOP Experiment

In this chapter, we begin by describing the features and components of the EAS-TOP experiment, mentioning briefly the physics topics that it investigates. We subsequently describe the various trigger configurations according to which events are categorized. Then we describe the procedure used in reconstructing the parameters of the air shower, namely, the zenith and azimuth angles of the primary, the ground impact location of the shower core and the total size and age of the shower. For each parameter, we mention the resolution of the apparatus.

3.1 Description of the detector

3.1.1 Detector description

EAS-TOP is an **E**xtensive **A**ir **S**hower array located on **TOP** of the Campo Imperatore, the mountain above the Gran Sasso Laboratory, at an altitude of about 2005 m above sea level, or a vertical atmospheric depth of 810 g/cm^2 (or a slant depth of about 990 g/cm^2 in the direction of the underground laboratory). The detector is described in References [64] and [65]. It consists of twenty-nine scintillation counter stations, each about 10 m^2 in area, covering a total effective area of about 10^5 m^2,

over which the electromagnetic component of a cosmic shower front is sampled. A schematic layout of the array is shown in Fig. 3.1. The stations are separated by about 17 m near the center of the array (coordinate (0,0)) and about 80 m elsewhere. Each station consists of sixteen scintillation counters 80 $\times$ 80 cm^2-large, housed in a metal shed for protection against harsh weather conditions. All scintillators are 4 cm-thick NE102A plastic. Each of the sixteen scintillators in a station is viewed by one XP3462B photomultiplier tube (PMT), with a risetime of 3 ns, set at high gain for timing measurements (and to count up to 500 particles from the signal's amplitude); in addition, the four central scintillators are viewed by one extra PMT set at low gain, for large amplitude measurements, covering a dynamic range up to 5000 particles. When a trigger condition occurs (see Section 3.2), a maximum of 29 ADC signals from the low gain PMT's, 29 ADC signals from the high gain PMT's and 74 TDC signals are read out (some stations, belonging to more than one trigger subarrays, are read out more than once). Calibrations of the relative timing between the various scintillator modules, of paramount importance in determining the shower axis direction (see Section 3.3), are periodically performed by measuring time differences between each scintillator and a small, portable reference scintillator counter carried to each counter (a coincidence between this portable counter and the counter under calibration is used as a trigger). The time delays with respect to this portable counter can be calibrated to better than 0.5 ns. Amplitude calibrations, necessary in determining the number of particles traversing any given counter (and therefore the total shower size; see Section 3.3), are performed by considering the single-particle spectrum. Specifically, the gain of a PMT is adjusted until the ratio R of the number of counts below the single-particle peak (but above a local minimum in the distribution) to that of the number of counts above the peak agrees with a standard value (see Reference [65]). In this manner, the PMT gain can be adjusted to about 1% without affecting the timing calibrations (which are insensitive to gain

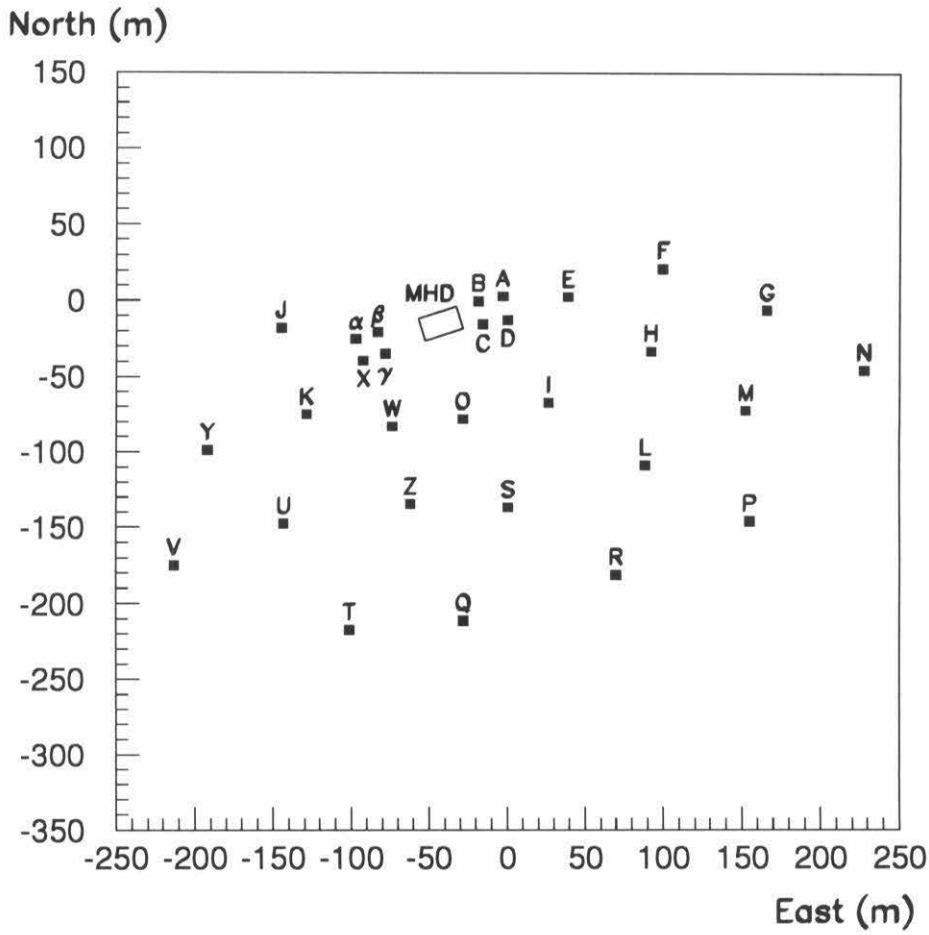

Figure 3.1: Layout of the EAS-TOP array. It consists of twenty-nine scintillation counter stations, labeled A through Z and α through γ. At the center of the array is a hadron and low-energy muon calorimeter, labeled MHD.

variations of up to 10%).

In addition to the scintillator stations, EAS-TOP is equipped with a muon and hadron calorimeter (labeled MHD in Fig. 3.1) located near the center of the array. It consists of two modules of area 12×12 m^2, each with nine active planes of streamer tubes interspersed with 13 cm-thick layers of iron absorber. It is designed to measure the energy spectrum, lateral distribution and time delay of the hadrons in the core of air showers up to TeV energies, and to count and track the low-energy muons ($E > 2$ GeV) accompanying the shower front. The calorimeter is described in Reference [66]. It was still under construction at the time the data used in this thesis were collected, and is therefore not discussed further here.

3.1.2 The physics of EAS-TOP

The array aims at determining the all-particle differential primary energy spectrum (such as that of Fig. 1.1) in the interesting region of the knee, where the details of the spectrum are still somewhat controversial (such as the existence of a "bump," or "knee-cap" – see Reference [45]). Anisotropies in the arrival directions of high-energy ($E > 10^5$ GeV) cosmic rays can be sought.

Various characteristics of air showers can be studied, such as the lateral and temporal developments of the electromagnetic component (see Reference [67]), or the characteristics of the hadronic core and low-energy muons (see Reference [66]).

Searches for point sources of γ-rays are conducted, and some results are presented in References [68].

Finally, as mentioned in Section 2.1.3, primary mass composition can be studied by combining surface measurements of air showers with TeV muons detected deep underground (see References [60], [1] and this thesis).

3.2 Trigger configurations, efficiencies and rates

3.2.1 Trigger configurations

For triggering purposes, the array is divided into eleven overlapping subarrays (SA) of at least six and up to eight stations each. The various trigger subarrays are summarized in Table 3.1, where the letters refer to the counters shown in Fig. 3.1. A

SA1	SA2	SA3	SA4	SA5	SA6	SA7	SA8	SA9	SA10	SA11
A	E	H	I	O	O	Y	J	γ	W	I
B	F	G	H	I	S	K	X	C	γ	C
C	G	N	M	L	Q	T	W	I	O	E
D	H	P	P	R	T	V	U	S	Z	H
X	I	M	L	Q	U	U	Y	W	U	L
γ	L	L	R	Z	W	Z	K	O	K	S
α	M		S	S	Z					O
β	A									

Table 3.1: Trigger subarrays (SA), where letters refer to the scintillator stations of Fig. 3.1.

minimal trigger condition is satisfied when, within 2 μs, each of any four neighboring stations receive a total energy deposit corresponding to at least about 0.3 vertical minimum-ionizing particles. Only stations belonging to subarrays that have triggered are read out. Triggers are divided into the following categories:

- **Trigger 0 (FAI)**: events for which the EAS-TOP reconstruction procedure (see Section 3.3) fails, owing to very small numbers of particles detected (**FAI**led reconstruction);

- **Trigger 1 (HEI)**: events where all stations of a subarray, except SA1, have fired, and for which the central station has recorded the greatest number of particles; this corresponds to high-energy events, with shower core within the boundaries of the array (**H**igh-**E**nergy, **I**nternal events);

- **Trigger 2 (HEE)**: events where at least six stations of a subarray, except SA1, have fired, but for which the central station has *not* recorded the greatest number of particles; this corresponds to high-energy events, with shower core outside the boundaries of the array (**H**igh-**E**nergy, **E**xternal events);

- **Trigger 3 (LEE)**: events for which the triggered subarray (except SA1) has at least four fired stations (including the station central to that subarray), but fewer than six, and for which at least two stations lie on the edge of the array; this corresponds to relatively low-energy events, with shower core outside the boundaries of the array (**L**ow-**E**nergy, **E**xternal events);

- **Trigger 4 (ITR)**: events which triggered subarray SA1 (**I**nner **TR**igger events);

- **Trigger 6 (LEI)**: events for which the triggered subarray (except SA1) has at least four fired stations (including the station central to that subarray), but fewer than six, and for which at most one station lies on the edge of the array; this corresponds to relatively low-energy events, with shower core within the boundaries of the array (**L**ow-**E**nergy, **I**nternal events).

3.2.2 Efficiencies and rates

The overall trigger rate for the entire array is about 35 Hz, and that for HEI events is about 1.5 Hz. The minimum primary energy required to trigger the array is about 5×10^4 GeV for ITR events (p-initiated), about 10^5 GeV for LE events, and

1.5×10^5 GeV for HE events. The trigger efficiency is estimated to rise from about 10% at 10^5 GeV to 100% at 6×10^5 GeV (shower sizes $N_e = 10^4$ and 10^5, respectively). The acquisition system requires about 1 ms to read out and record each event, for a dead time of about 3.5%.

3.3 Event reconstruction and resolutions

3.3.1 Angular reconstruction

The zenith and azimuth angles of the shower axis are reconstructed by fitting a planar shower front to the distribution of times at which the various stations fired relative to each other. This hypothesis of a flat shower front is acceptable for internal events; in the case of external events, the curvature of the shower front becomes important and has to be taken into account in reconstructing the direction of the axis. However, in this thesis, the events analyzed will be mostly restricted to the HEI category. The thickness of the shower front increases with distance from the core. As discussed in Reference [65], at distances between 40 and 120 m from the shower axis (or an average particle density of 6 particles per station), the measured thickness of the front is on the order of 1.5 m (5 ns), and dominates timing fluctuations (instrumental interstation timing uncertainties are less than 0.5 ns).

The angular resolution is a function of primary energy and trigger configuration. For events that have fired many stations (*e.g.*, HEI events), say seven, the direction can be determined twice by using four stations each time (one station is used twice), as in Reference [65]. Comparing the two directions obtained, one can infer an angular resolution of about 0.8°. This improves to 0.6° for $N_e > 10^5$. Alternately, as described in Reference [69], a deficit in the rate of events from the direction of the Sun or the Moon (shadowing effect) can be measured. For HEI events within 40° of the zenith, angular bins 4° × 3.2° (more precisely ±2° in declination and

$\pm 1.6°$ in right ascension), centered on the Sun or the Moon, are used to accumulate events ("ON" source). The angular diameter of both objects is 0.52°. The number of counts obtained in the bin is compared to the average number of counts in the two surrounding bins of the same size at the same declination ("<OFF>" source). Each angular bin is divided into $0.1° \times 0.1°$ pixels. The observed deficit (Sun and Moon data added), of significance 2.7 standard deviations, is plotted in Fig. 3.2 as (ON – <OFF>)/<OFF>. The angular resolution deduced from this is $(0.8 \pm 0.1)°$ (for HEI events). For the other trigger configurations, corresponding to either lower energy primaries or external core events, the angular resolution is worse. It is estimated to be on the order of 4° for HEE, LEE and LEI events, and 6° for ITR events.

After the zenith and azimuth coordinates of the shower axis are determined, the coordinates of the twenty-nine stations are transformed into a plane orthogonal to the shower direction, and the core location as well as lateral particle density profile are determined in this coordinate system.

3.3.2 Core location

A first estimate of the location of the core of the air shower is obtained by calculating the center of gravity of the distribution of hits in the four stations with the highest counts, using the particle densities as the weights. A more refined computation is subsequently performed, with an NKG profile (see next section) fitted to the lateral density distribution. For HEI events, the accuracy with which the core location can be determined with this method is estimated to be better than 10 m (for a total shower size $N_e > 10^5$).

3.3.3 Shower size and age parameter

The remaining shower parameters, the total shower size N_e and age parameter s, as well as a more refined core location, are obtained by minimizing the χ^2 of the

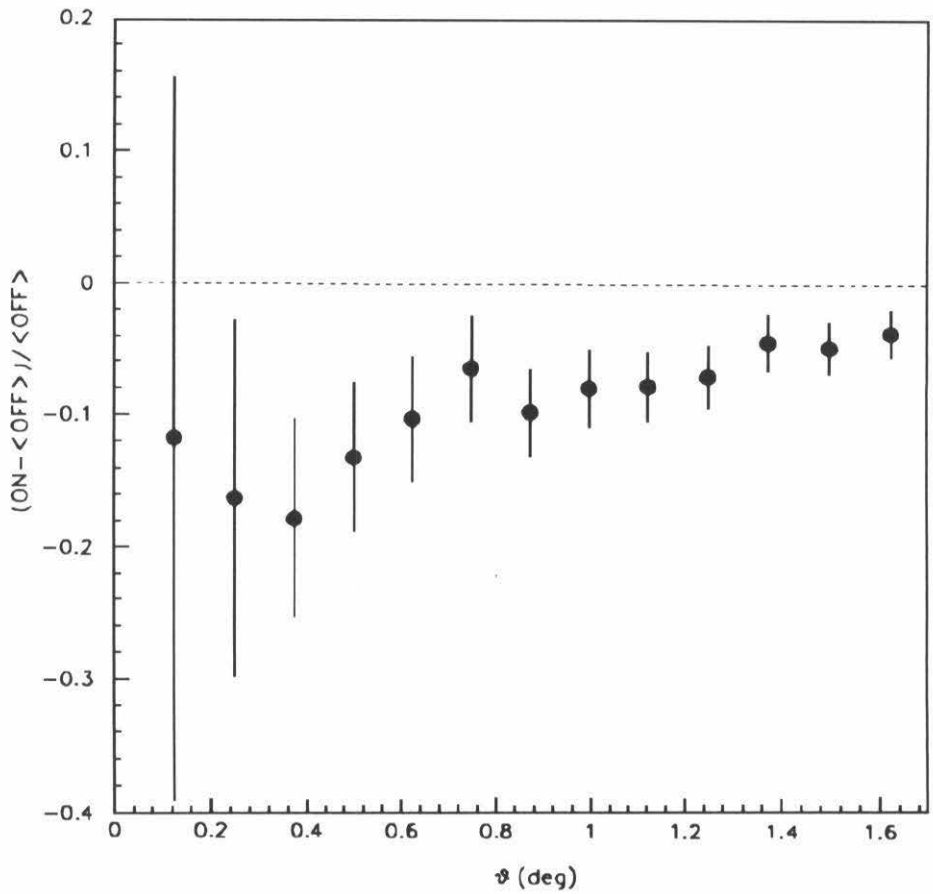

Figure 3.2: Shadow of the Sun and the Moon: deficit in the number of events pointing to within a $4° \times 3.2°$ window centered on each cosmic-ray sink ("ON" source), compared to adjacent angular bins ("OFF" source).

difference between the measured particle densities as a function of distance from the core (the lateral distribution function) and the NKG (Nishimura-Kamata-Greisen) shower profile (see Reference [70]):

$$\rho(r) \propto N_e \left(\frac{r}{r_0}\right)^{(s-2)} \left(1+\frac{r}{r_0}\right)^{(s-4.5)} \tag{3.1}$$

where $\rho(r)$ is the surface density of e^+ and e^- at distance r from the core (where r is itself a function of the core location (X_c,Y_c)), N_e is the shower size, or total number of charged particles (mostly e^+ and e^-) in the shower at the level of the detector, r_0 is the Molière radius (100 m at the depth of EAS-TOP) and s is the shower age parameter (related to the atmospheric depth t, in number of radiation lengths, the primary energy E_p and the critical energy for electrons in air E_c by, approximately: $s \simeq 3t/(t+2\ln(E_p/E_c))$). Although this NKG distribution was derived in the context of relating shower parameters to the lateral distribution of electrons of all energies, the experimental situation is usually different, in that only charged particles of energy above a certain threshold (about 8 MeV for EAS-TOP) are recorded. In Reference [71], recent Monte Carlo calculations were found to agree with the general form of the NKG function for different electron detection thresholds, with some reinterpretation of the parameters (for example, the Molière radius is reduced by one half). The interpretation of the parameters reconstructed by fitting the NKG function to the experimental data is further complicated by the fact that in the experimental setup, a fraction of the photons in the shower convert to e^+e^- pairs in the metal roof of the shed or in the scintillator itself, therefore yielding a signal in the detectors. Low-energy muons and hadrons accompanying the shower front also deposit energy in the counters. The hadrons are concentrated near the core, and although the muons account for only about 10% of the total number of charged particles in the front, their lateral distribution is broader than that of the electrons (see Reference [13], Chapter 16).

A typical HEI event and its NKG reconstruction are shown in Fig. 3.3.

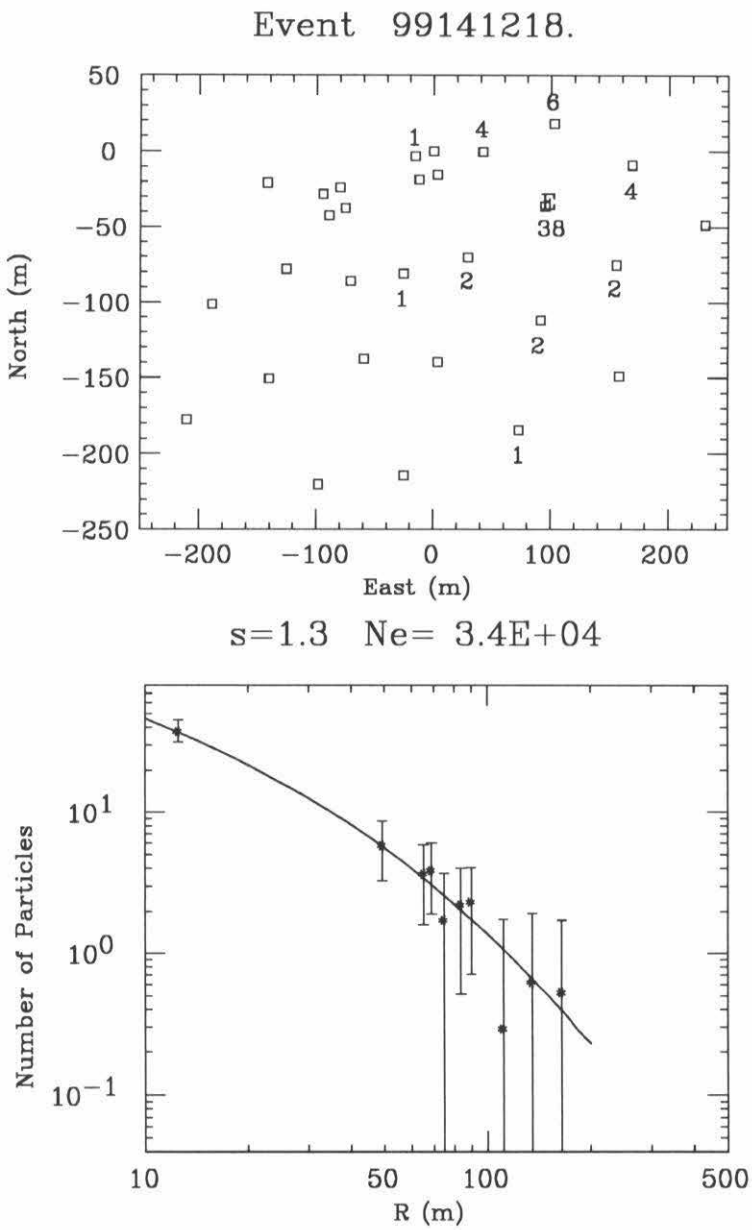

Figure 3.3: Example of a typical HEI event, showing the array and the number of particles recorded by each station (stations with no hits have no number shown next to them). The core location is identified by the E. The NKG reconstruction for this event yields $N_e = 3.4 \times 10^4$ and s= 1.3.

Uncertainties on the numbers of particles determined from ADC measurements arise from Landau fluctuations in the energy deposited, PMT gain drifts and errors in the conversion factor from ADC to number of particles (where the conversion factor is measured for single, minimum-ionizing muons). In addition, at a distance r from the core, Poissonian fluctuations in the number of particles detected further increase the variances used in the definition of the χ^2 variable to be minimized (more details on this can be found in References [72]). The estimated accuracies to which the shower size and age can be reconstructed are $\Delta N_e/N_e < 20\%$ and $\Delta s < 0.1$.

Chapter 4

Coincidences and Anticoincidences

Coincident events are cosmic-ray events that are observed essentially simultaneously by EAS-TOP (as an electromagnetic shower reaching the ground) at the surface, and by MACRO (as a bundle of parallel muons) deep underground. The electromagnetic shower and high-energy muons are two components of the same cosmic-ray event. Anticoincident events are muon events seen by MACRO, pointing in the direction of EAS-TOP, but not having triggered the surface array because the electromagnetic showers accompanying the high-energy muons are below its sensitivity threshold.

MACRO and EAS-TOP had operated simultaneously for about 46 days in 1989, at which time the feasability of combining the independent data sets of the two detectors to identify 347 coincident events was demonstrated (see Reference [60]). Since then, several improvements were carried out, including doubling the operational size of MACRO from one to two supermodules, the installation by EAS-TOP of a 1 μs atomic clock to replace a 100 μs quartz clock previously used, and the full instrumentation of 29 counters by EAS-TOP, as opposed to 22 previously. This thesis concerns itself with data collected during a second period of combined data taking of 96 days in 1990, with the improvements mentioned above.

In this chapter, we first describe the method by which coincident events are re-

covered from the two separate data sets of MACRO and EAS-TOP on the basis of timing information and we estimate the background of chance coincidences. Then, concentrating on one class of coincident events, we compare the independent event reconstructions performed by the two experiments, and use them to identify and eliminate the background. We subsequently present the distributions of muon multiplicities and shower sizes for the coincident events. After this, we define and describe anticoincident events and present their muon multiplicity distribution. Finally, we summarize and draw some conclusions.

4.1 Coincident event definition and identification

4.1.1 Time differences and clock drifts

The relative positions of MACRO and EAS-TOP are shown schematically, to scale, in Fig. 4.1. EAS-TOP lies in the direction of minimum rock thickness above MACRO. Fig. 4.2 shows the two detectors and the Gran Sasso Laboratory superimposed on a topographic map of the Campo Imperatore area. MACRO and EAS-TOP operate completely independently from each other, and there is no real-time data link between them. Events are recorded and stored separately, and coincident events are identified offline on the basis of the absolute time at which each has occurred.

The two detectors are each equipped with a 10 MHz Rubidium oscillator atomic clock, stable against long term frequency drifts to within about 1 part in 10^{11}, with which the time of occurrence of individual events is determined to a precision of better than 1 μs. The two clocks are periodically synchronized with Universal Time by first measuring deviations from television synchronization signals, and then comparing with a similar measurement performed by the Italian time standard institution (Galileo Ferraris), relative to Universal Time (see Reference [52]). At the end of each day, an automatic procedure sorts through all MACRO events recorded during the

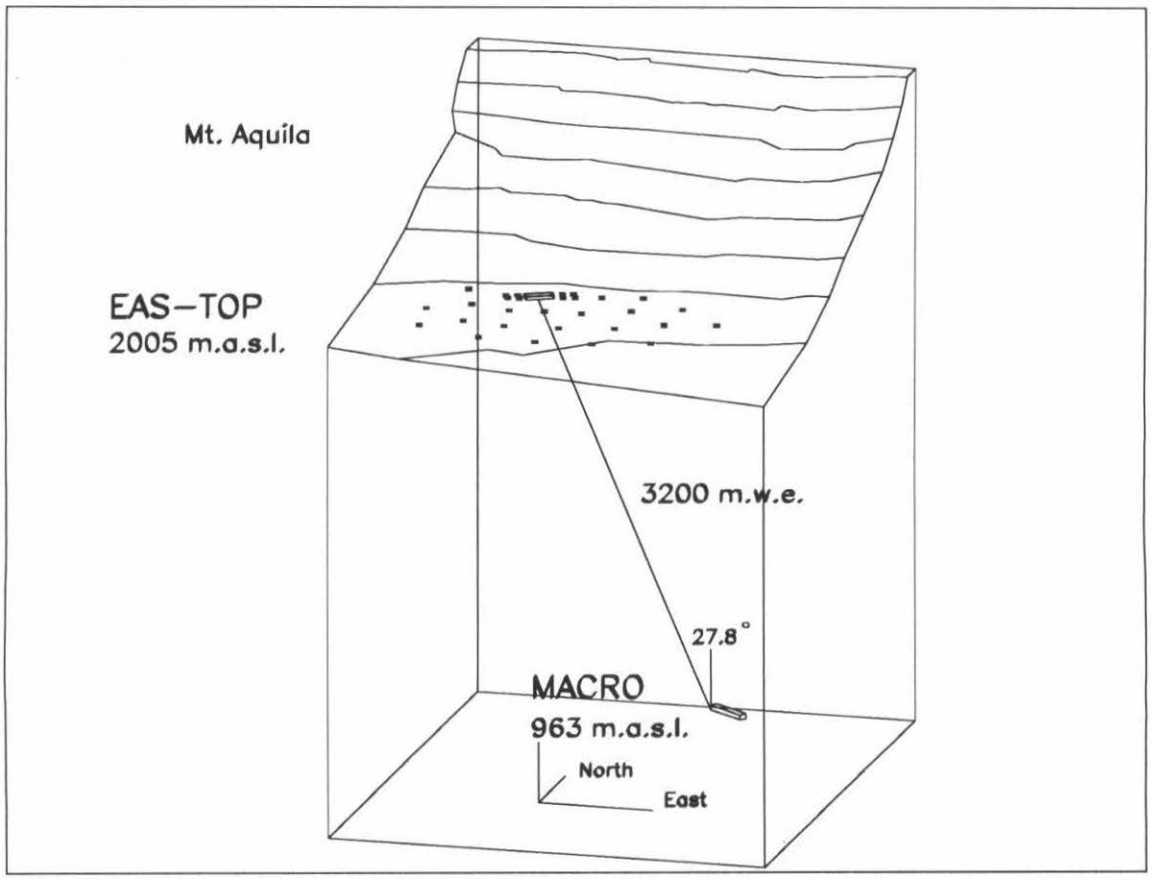

Figure 4.1: Relative positions of the two detectors. The origins of the MACRO and EAS-TOP coordinate systems are at altitudes of 963 and 2005 meters above sea level (m a.s.l.), respectively, and are separated by 3200 m w.e. of rock. The line joining the two is at 27.8° from the vertical, and its projection onto a horizontal plane makes a 6.45° angle from North (Eastward).

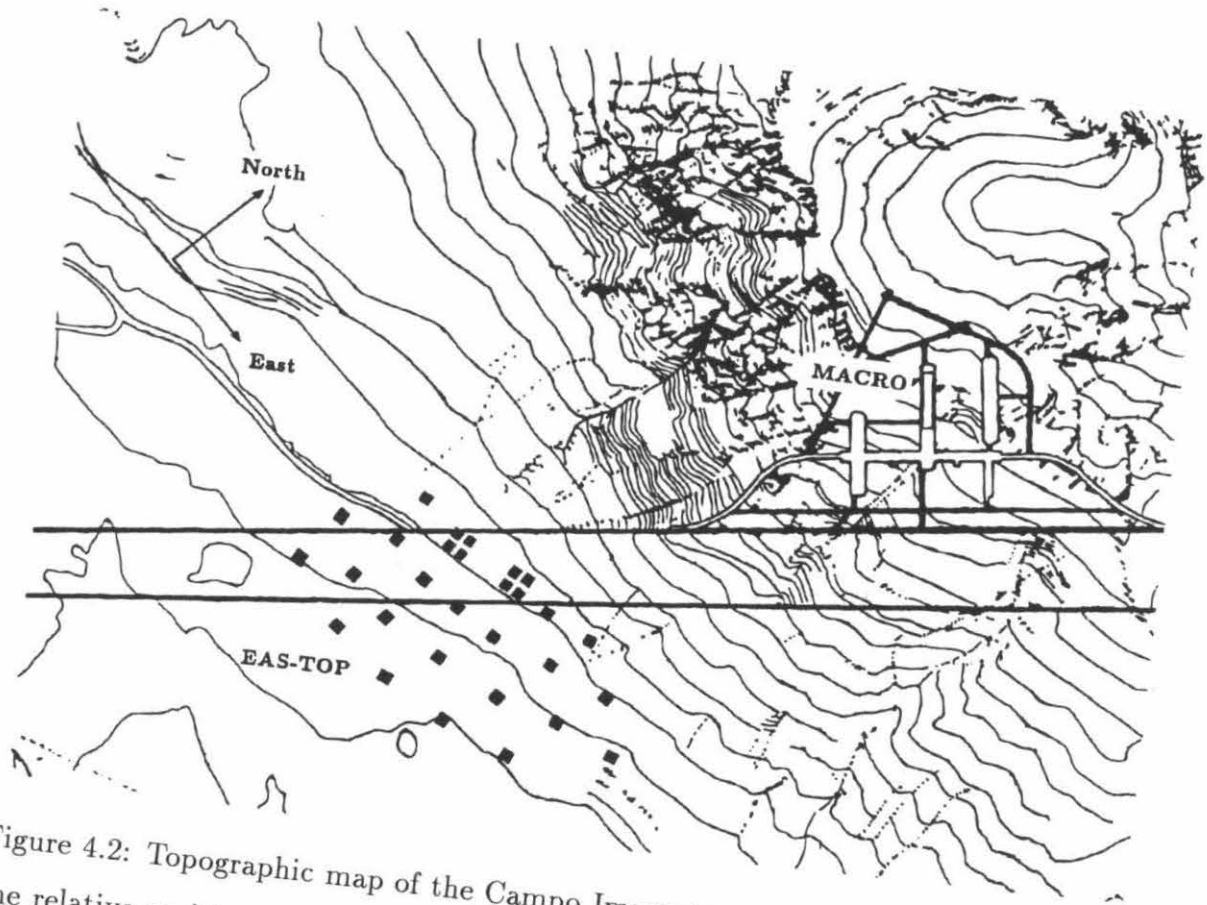

Figure 4.2: Topographic map of the Campo Imperatore and Monte Aquila showing the relative positions of MACRO, EAS-TOP and the Gran Sasso Laboratory. The vertical distance between consecutive contour lines is 20 m. The EAS-TOP counters are drawn larger than they should appear at this scale, for visibility reasons. The two thick lines across the picture are the twin highway tunnels traversing the mountain.

day, selects events having satisfied the muon pre-selection requirements defined in Section 2.3.1, and for each, scans EAS-TOP data looking for events having occurred in a 6 ms time window around it. This window is large enough that no coincidences are lost. Indeed, the relativistic time of flight between the two detectors is about 3 μs, the maximum timing drift between the two clocks due to slightly different oscillator frequencies is about 10 μs/day, and catastrophic offsets introduced in the EAS-TOP clock are of at most 1.5 ms (see Fig. 4.4 and discussion below for more on the last two points).

The events selected by the above procedure are classified by MACRO runs, each of maximum duration about 12 hours. Fig. 4.3 shows the distribution of differences between the MACRO muon event times and EAS-TOP event times in a 6 ms window, for one MACRO run. A one-bin peak (actually 4 μs-wide) due to real coincident events clearly stands out from a background of chance coincidences within the time window. For each MACRO run, the location of the time coincidence peak is determined to a precision of about 5 μs. By plotting the coincidence peak location as a function of calendar time, as is done in Fig. 4.4, the secular relative drift of the two atomic clocks can be monitored, and corrected for. We divide the MACRO runs plotted in Fig. 4.4 into thirteen regions, defined according to the smoothness of peak drift with time. They are separated by sharp discontinuities associated with disruptions in the power to the atomic clocks (when powered on again, the clocks were independently resynchronized once with the television signal, introducing variable offsets). For each region, a linear least squares fit is made to parametrize the coincidence peak location as a function of time. Two such regions are shown in Fig. 4.5 with the corresponding fits. The fit parameters are summarized in Table 4.1. The relative drift of about 10 μs/day prior to run 2546 was due to slight differences in the oscillator frequencies of the two clocks. After the frequencies were finely tuned, the relative drift became less than 1 μs/day, in agreement with the rated clock stability

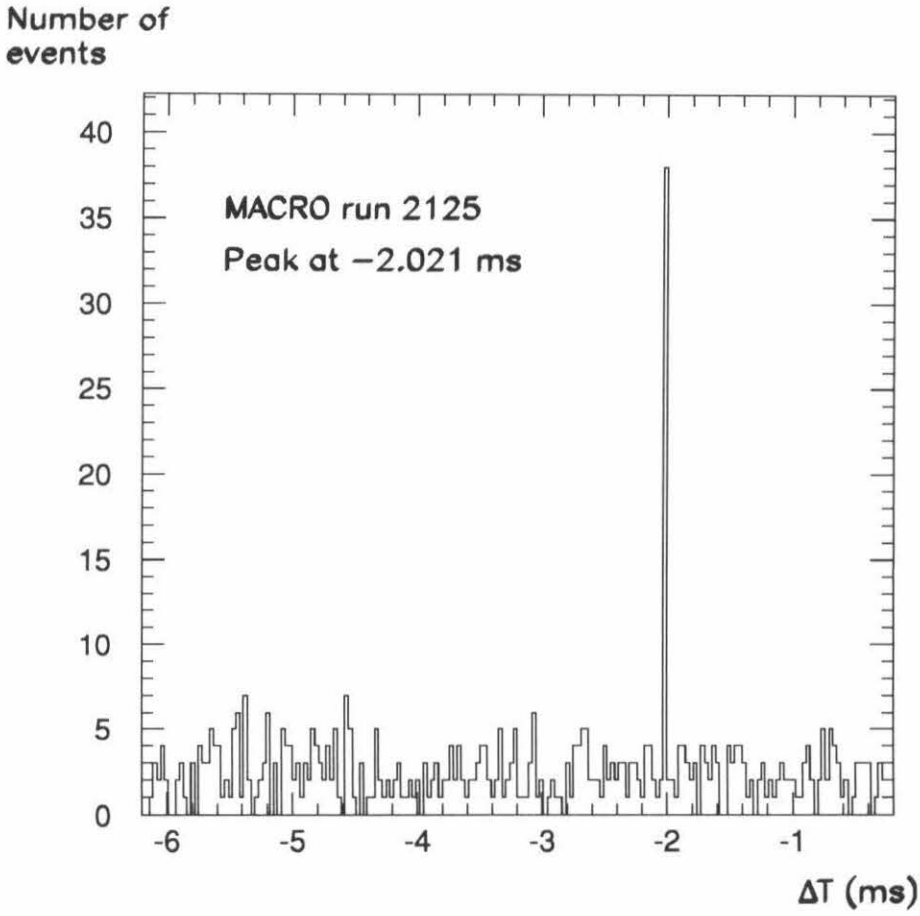

Figure 4.3: Distribution of time differences $\Delta T = T_{MACRO} - T_{EAS\text{-}TOP}$ for an initial time coincidence window of 6 ms, for an 8.2 hours-long MACRO run. Each bin is 30 μs-wide for visual clarity, but the peak is actually 4 μs-wide. The location of the peak at about –2 ms rather than 0 ms is a result of the variable offset of the two clocks.

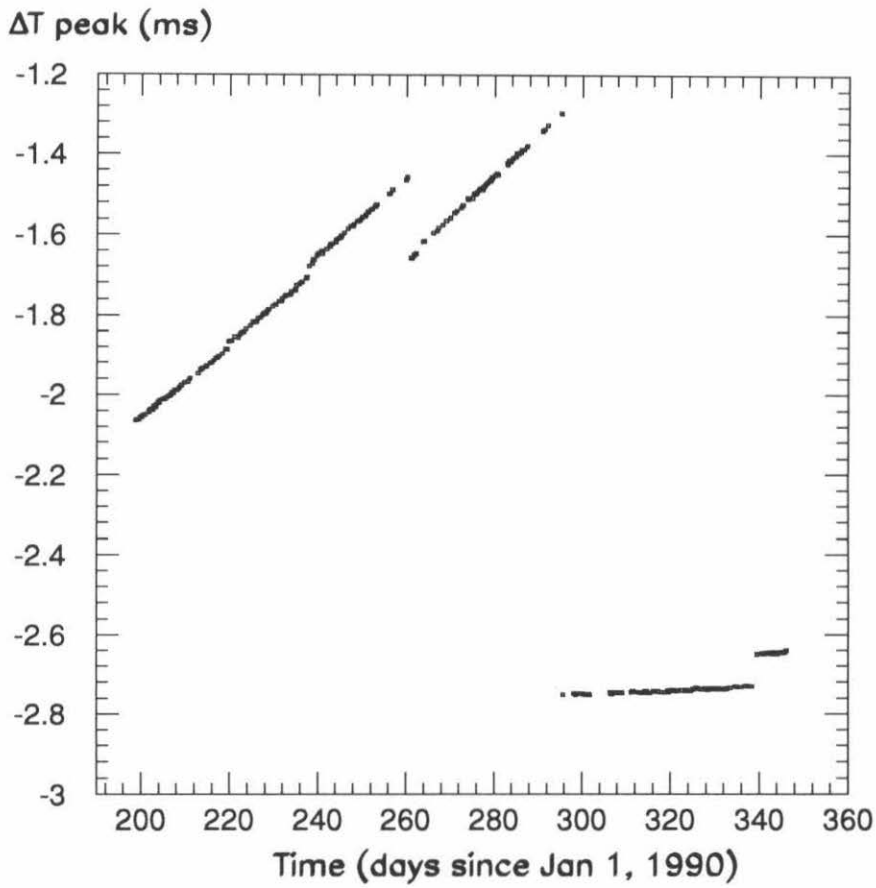

Figure 4.4: Location within the 6 ms time window of the coincidence peak as a function of time. Each data point represents one MACRO run for which the coincidence peak was defined by at least 5 events, which corresponds to a run at least about 1.5 hours long.

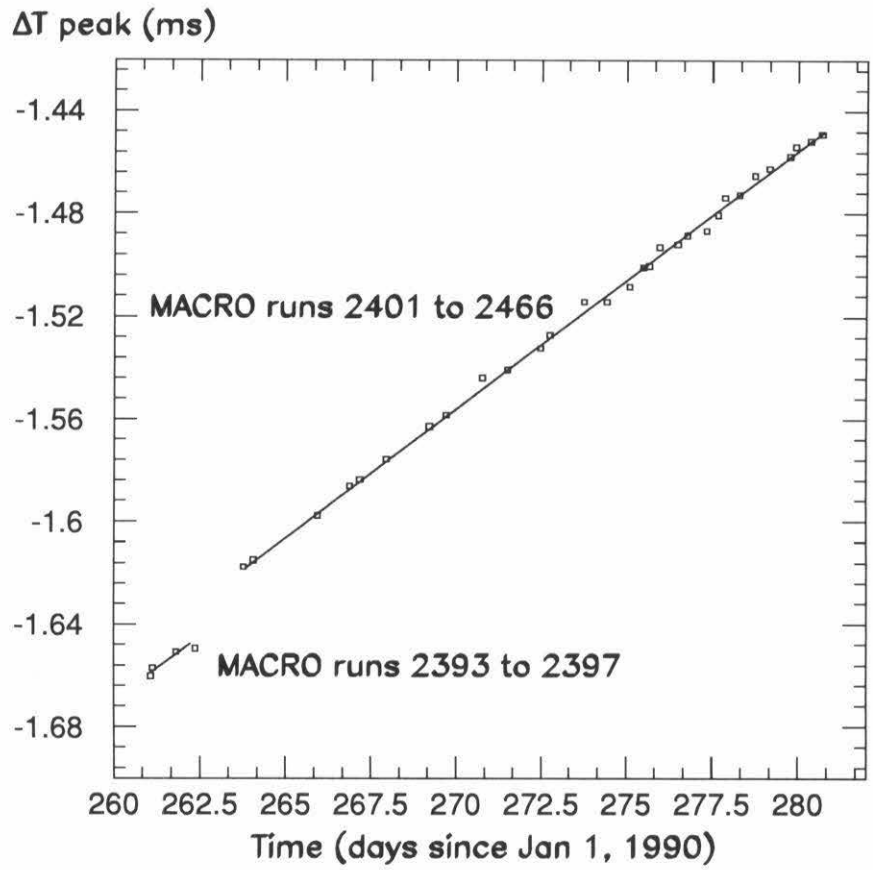

Figure 4.5: Time coincidence peak position as a function of time, for two of the thirteen regions described in the text. The relative clock drift rates were 9.8 μs/day and 10.1 μs/day for the lower-left and upper-right regions, respectively (see Table 4.1).

MACRO run range	Median time of first run (days since Jan 1, 1990)	A (μs/day)	B (μs)
2100 – 2157	198.66	8.53 ± 0.04	–3761 ± 7
2158 – 2214	208.59	8.67 ± 0.06	–3790 ± 10
2225 – 2226	218.97	4.94 ± 0.00	–2969 ± 0
2227 – 2295	219.80	9.09 ± 0.03	–3868 ± 7
2297 – 2298	237.91	9.55 ± 0.00	–3949 ± 0
2300 – 2375	238.89	9.51 ± 0.02	–3935 ± 6
2393 – 2397	261.06	9.8 ± 0.6	–4200 ± 200
2401 – 2466	263.86	10.05 ± 0.04	–4270 ± 10
2480 – 2539	281.46	10.48 ± 0.05	–4390 ± 20
2546 – 2563	295.95	0.18 ± 0.05	–2800 ± 20
2572 – 2629	306.13	0.38 ± 0.02	–2865 ± 6
2631 – 2693	319.44	0.66 ± 0.01	–2955 ± 3
2696 – 2728	339.60	0.93 ± 0.04	–2970 ± 10

Table 4.1: Linear least squares fit parameters for the thirteen periods of simultaneous running of MACRO and EAS-TOP defined in the text. At time t measured in days since January 1, 1990, the time coincidence peak location ΔT_{peak} in μs is given by: $\Delta T_{peak} = At + B$.

of 1 part in 10^{11}, which results in drifts of 0.86 μs/day.

The differences between MACRO and EAS-TOP times are all corrected to account for the relative drifts of the two clocks, using the fits of Table 4.1. We plot in Fig. 4.6 the time difference distribution for all events in the 6 ms window after the clock drift corrections. Fig. 4.7 shows a scatterplot of the corrected time differences within $\pm 6\mu$s of zero, as a function of time. The three-sigma region defining coincidences (see below) is outlined. The structure that can be seen beyond the 297^{th} day is due to the resolving of individual μs clock ticks, which are not smeared by the small relative drifts over time (see Table 4.1). Fig. 4.8 is a projection of Fig. 4.7 onto the ΔT axis, or equivalently, an expanded view of the region near the peak of Fig. 4.6. It shows the corrected time difference distribution within a 10 μs window. The experimental distribution is very well fitted by a Gaussian with a standard deviation of (0.684 ± 0.006) μs, riding on a constant background of chance coincidences. We define an event to be a coincidence if the absolute value of its corrected time difference is less than 2.1 μs, or:

$$|\Delta T_{\text{corr}}| \equiv |T_{\text{MACRO}} - T_{\text{EAS-TOP}} - \Delta T_{\text{peak}}| \leq 2.1\mu\text{s} \qquad (4.1)$$

4.1.2 Coincidence rates

The two detectors operated simultaneously from July 18 to December 13, 1990, at which time data taking was interrupted when several EAS-TOP counters were severely damaged by snow avalanches. The total combined live time during that period was (96.3 ± 0.4) days (a 64.7 % efficiency). The live time was estimated by adding the time differences between the last and first events of each simultaneous running period (100.0 days), correcting for short periods between run beginning and first event, and last event and run end (0.4 days), and correcting for the combined

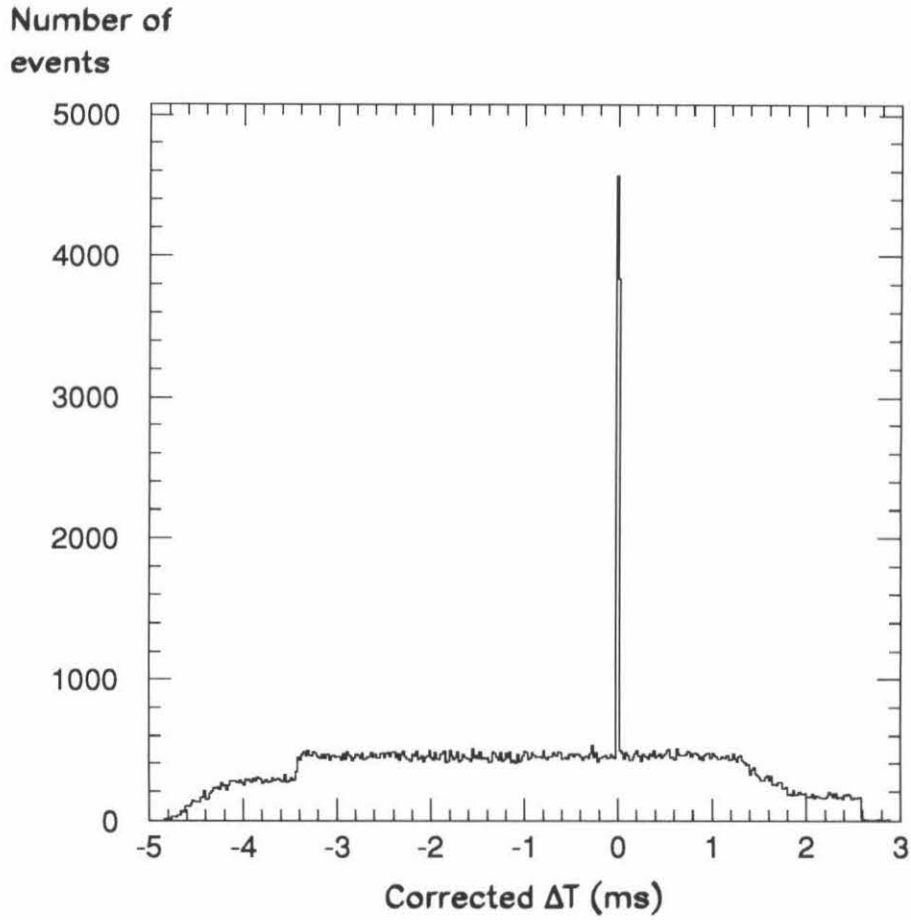

Figure 4.6: Distribution of time differences in the 6 ms window after correction for relative clock drifts. Each bin is 20 μs-wide for visual clarity, but the peak is actually 1.37 μs-wide (see Fig. 4.8). The structure below –3.4 ms and above 1.4 ms is due to the correction process and is of no significance.

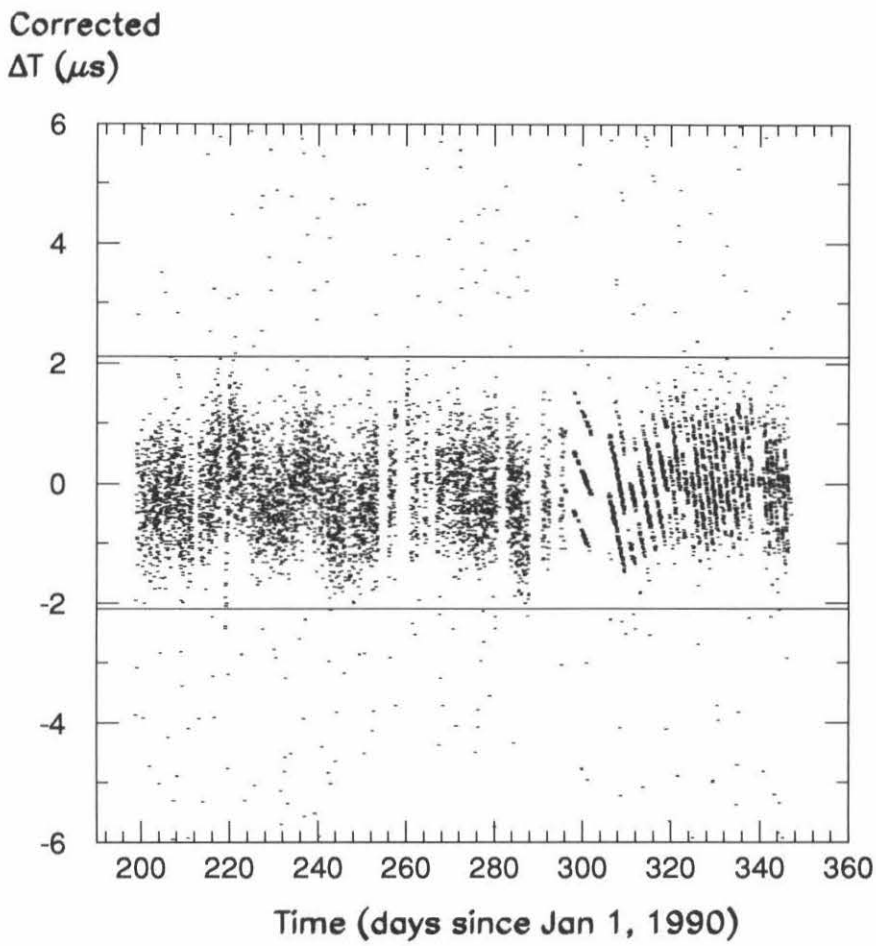

Figure 4.7: Corrected time differences within ± 6 μs of zero, as a function of time. The two horizontal lines delimit the three-sigma cut $\pm 2.1 \mu$s. Each point represents an individual event.

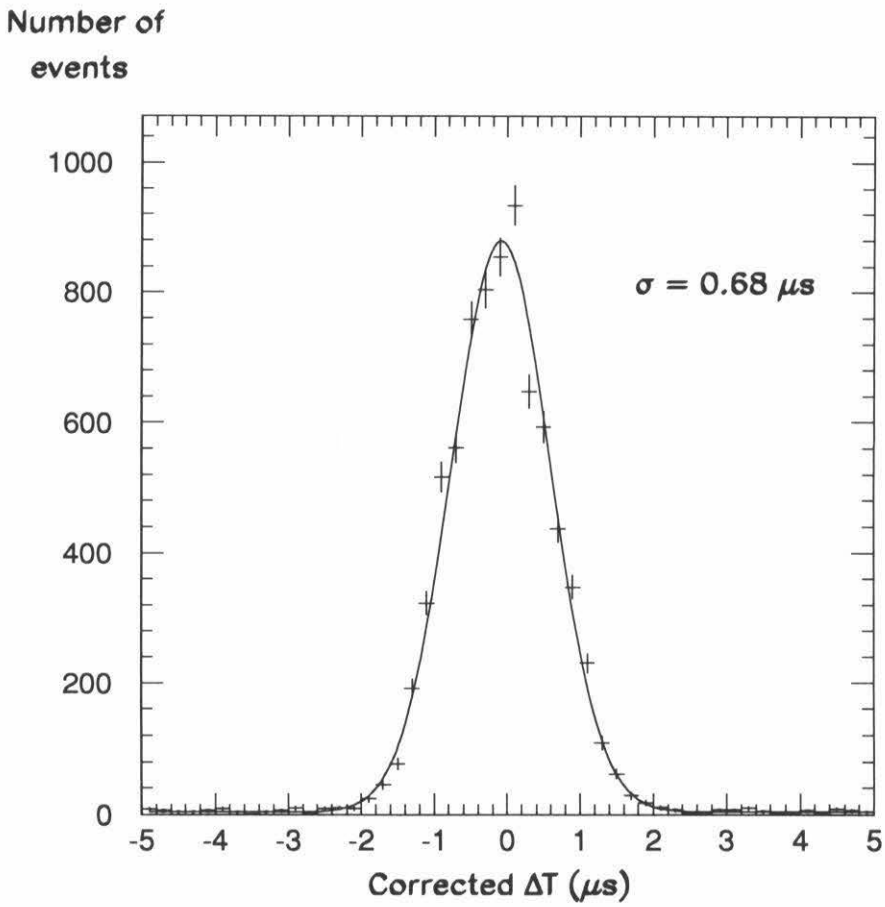

Figure 4.8: Corrected time difference distribution in a 10 μs window. The curve is a Gaussian fit riding on a constant background. The standard deviation of the Gaussian is (0.684 $\pm$ 0.006) μs, and the fitted background is (20 $\pm$ 2) events/μs. There are 7644 coincident events satisfying the three-sigma cut $|\Delta T| \leq 2.1\mu$s.

dead time of the two detectors (4.1%). Fig. 4.9 shows the distribution of time differences between consecutive coincident events, which is exponential, as expected for a constant coincidence rate (see Reference [58]). The time constant of the exponential is $\tau = (0.301 \pm 0.004)$h, and this represents the average time between events. Indeed, multiplying this average time between coincident events by the total number of coincidences (7644, see below), one obtains an estimated live time of (96 $\pm$ 1) days, in agreement with the dead time-corrected live time mentioned above. In Fig. 4.9, a lone pair of events is separated by 3.2 hours. Nothing wrong could be found with either detector during that time, but the probability of such a long gap without coincidences is so low ($\exp(-3.2/0.301) = 2.4 \times 10^{-5}$) that we take this gap as a source of uncertainty on the live time (the remainder of this uncertainty comes from uncertainty on the dead time).

During the 96.3 days of simultaneous running, 7644 coincident events were recorded, for an average rate of (79 $\pm$ 1) events/day (see Table 4.2). From Fig. 1.1, the total integrated primary flux between 2×10^5 GeV and 10^8 GeV is about 3×10^{-5} $m^{-2}s^{-1}sr^{-1}$. Thus, in 96 days, over an underground area of 288 m^2 and within a solid angle subtended by EAS-TOP at MACRO of about 0.1 sr, the number of coincidences expected is very roughly 7200, in agreement to within about 6% with our experimental results. That the coincidence rate remained constant with time to within the expected statistical fluctuations can be seen in Fig. 4.10, where we plot the rate (in events/day) as a function of time. On it, each data point represents one MACRO run. Fluctuations about the mean are due to the fact that the mean number of coincidences per MACRO run is about 26, and are therefore dominated by Poissonian statistics. Fig. 4.11 is a projection of Fig. 4.10 onto the rate axis, and shows that the distribution of rates is approximately Gaussian, as expected, and in agreement with the curve calculated from the average rate of (79 $\pm$ 1) coincidences/day (from the total number of events and the total live time) and the total number of

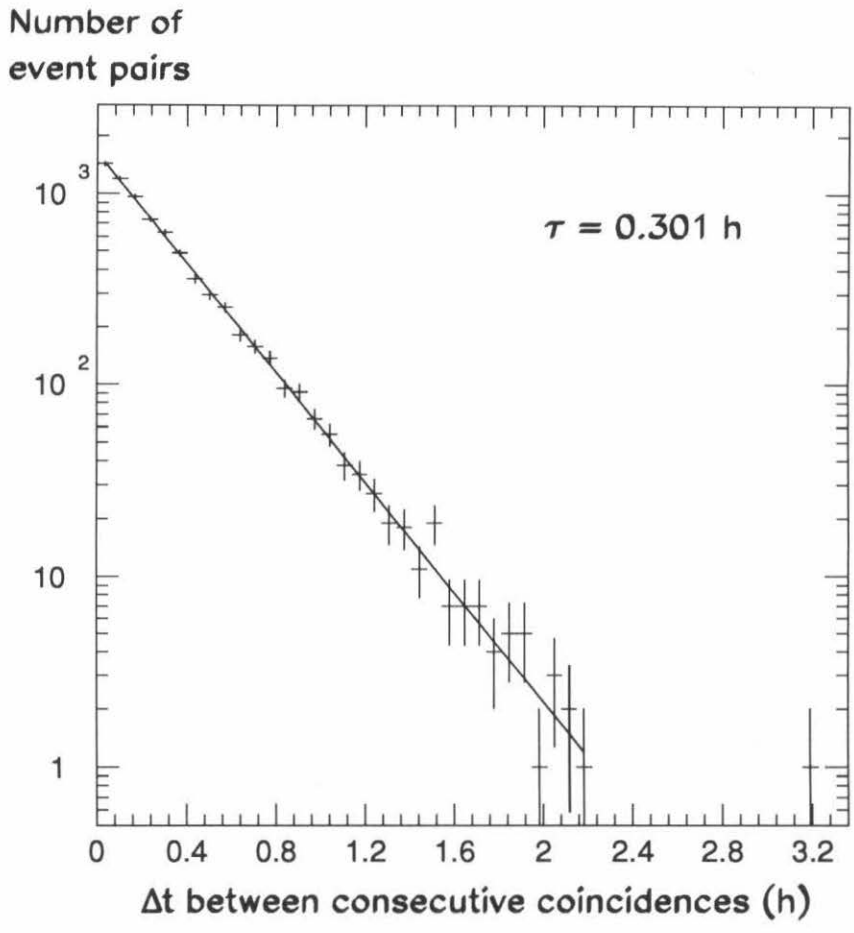

Figure 4.9: Distribution of time differences between consecutive coincident events. The curve is an exponential fit $N = N_0 \exp(-\Delta t/\tau)$, with $\tau = (0.301 \pm 0.004)$h.

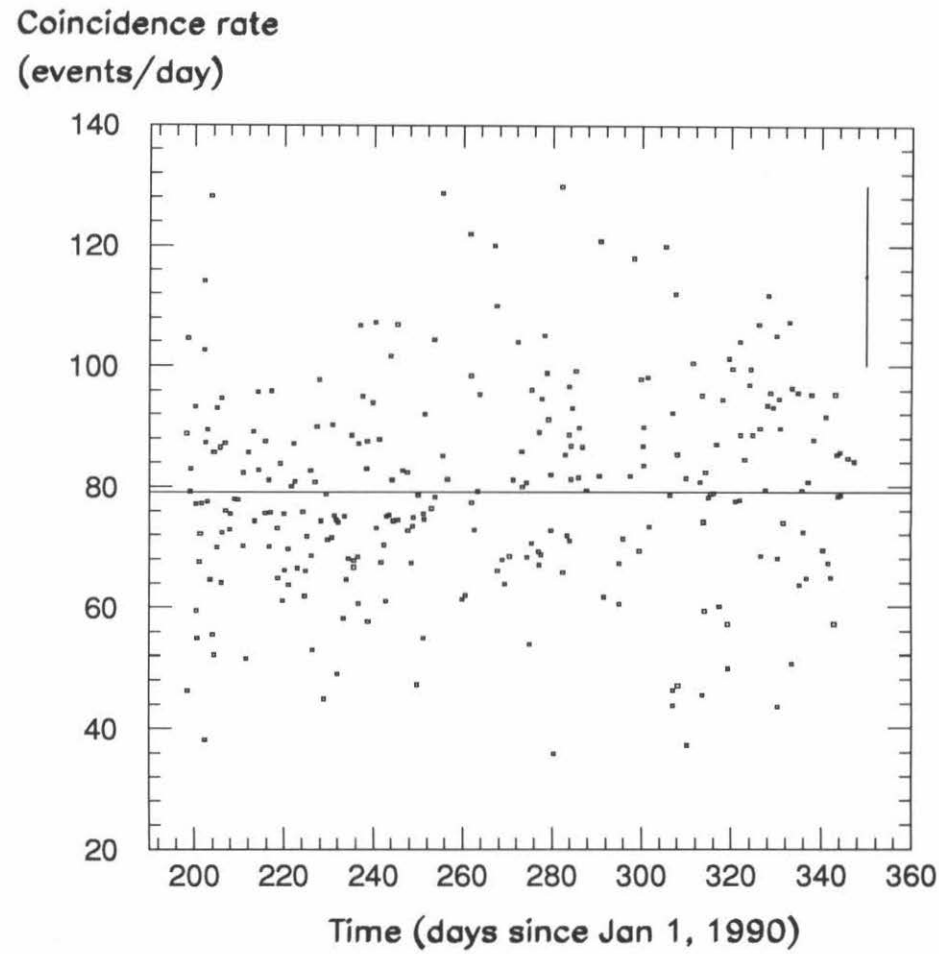

Figure 4.10: Coincidence rate as a function of time. Each point represents one MACRO run with at least 5 coincident events. For clarity, error bars are not drawn; however, a typical error bar is shown at the top right of the figure. The mean coincidence rate of 79 events/day (see Fig. 4.11) is represented by the horizontal line across the plot.

runs (264). Fig. 4.12 shows the distribution of the parameter $(N - RT)/\sqrt{RT}$, where N is the number of observed coincident events for a MACRO run, R is the average rate (79 ± 1) coincidences/day and T is the run duration (in days). As expected (for a sum of Gaussians with different widths for runs of different durations), the distribution is Gaussian with vanishing mean and unit width, indicative of good, stable operation of the detectors in coincidence.

As is apparent in Fig. 4.6, between a ΔT of –3.4 ms and 1.2 ms, there is a constant background of chance coincidences. In fact, there are (90000 ± 300) such accidental coincidences, in a time window $-3.0 \text{ ms} < \Delta T < 1.0 \text{ ms}$ (but excluding a 20 μs region centered on 0 ms), for a background of (22.61 ± 0.08) accidentals per μs bin (in agreement with the fit of Fig. 4.8). Therefore, we expect that in the 4.2 μs-wide coincidence window there are (95.0 ± 0.3) accidental coincidences. Compared with 7549 coincidences (7644 – 95), this represents a signal-to-background ratio of about 79 : 1 (or a 1.2% background contamination). Incidentally, the background rate is in agreement with a rough prediction from the individual trigger rates of the two experiments. The rate of underground muons at MACRO is roughly 1 muon/hour/m^2 (see Section 2.3.1). Therefore, in 96 days and over an area of 288 m^2, about 7×10^5 muons hit the detector. The EAS-TOP trigger rate is about 35 Hz (see Section 3.2.2), and thus the probability for an EAS-TOP event to happen within 4 ms of any given moment in time is 0.14. Consequently, we expect a grand total of about $0.14 \times 7 \times 10^5 = 98000$ events in a four ms window around the times of MACRO events, in agreement to within about 8% with the total number observed (90000).

Table 4.2 shows the mean coincidence rates for events falling under the various EAS-TOP trigger configurations defined in Section 3.2.1.

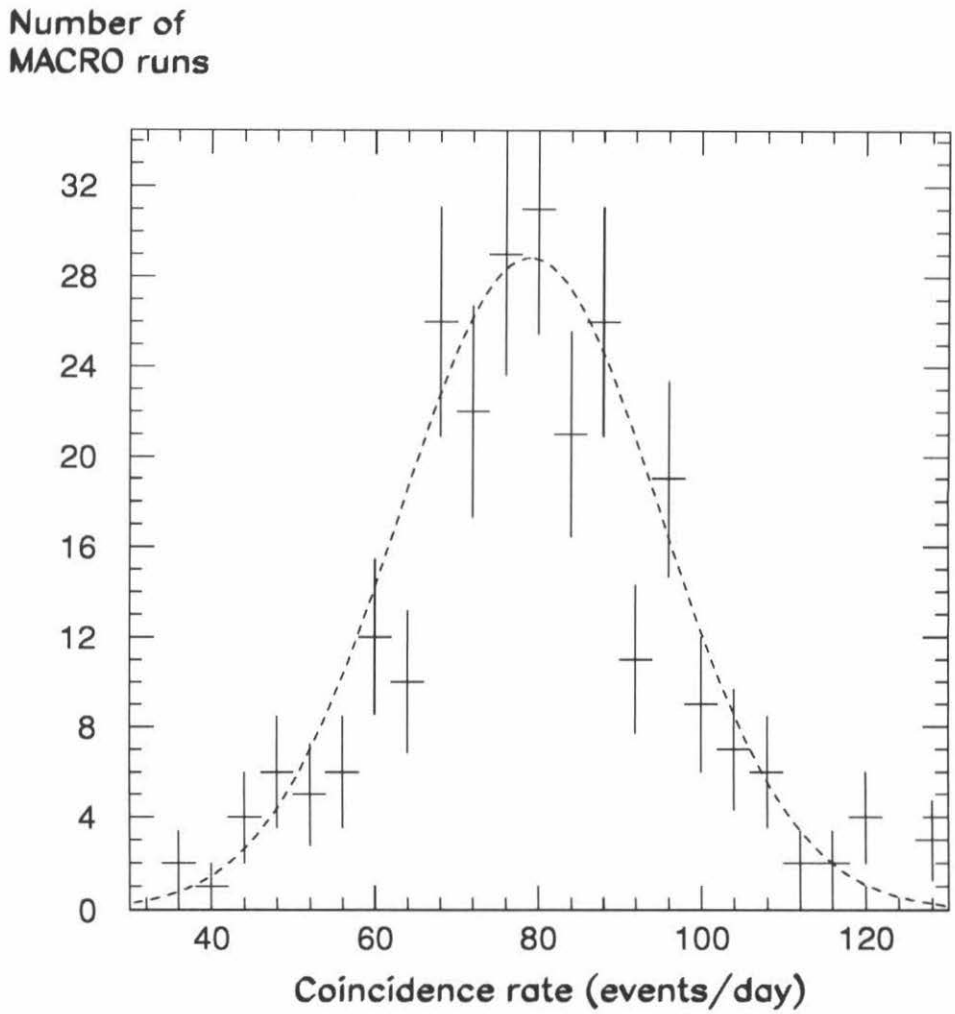

Figure 4.11: Distribution of coincidence rates. The curve is a Gaussian calculated by using the average rate of (79 ± 1) coincidences/day (from the total number of events and the total live time), and has a standard deviation of (16 ± 1) coincidences/day.

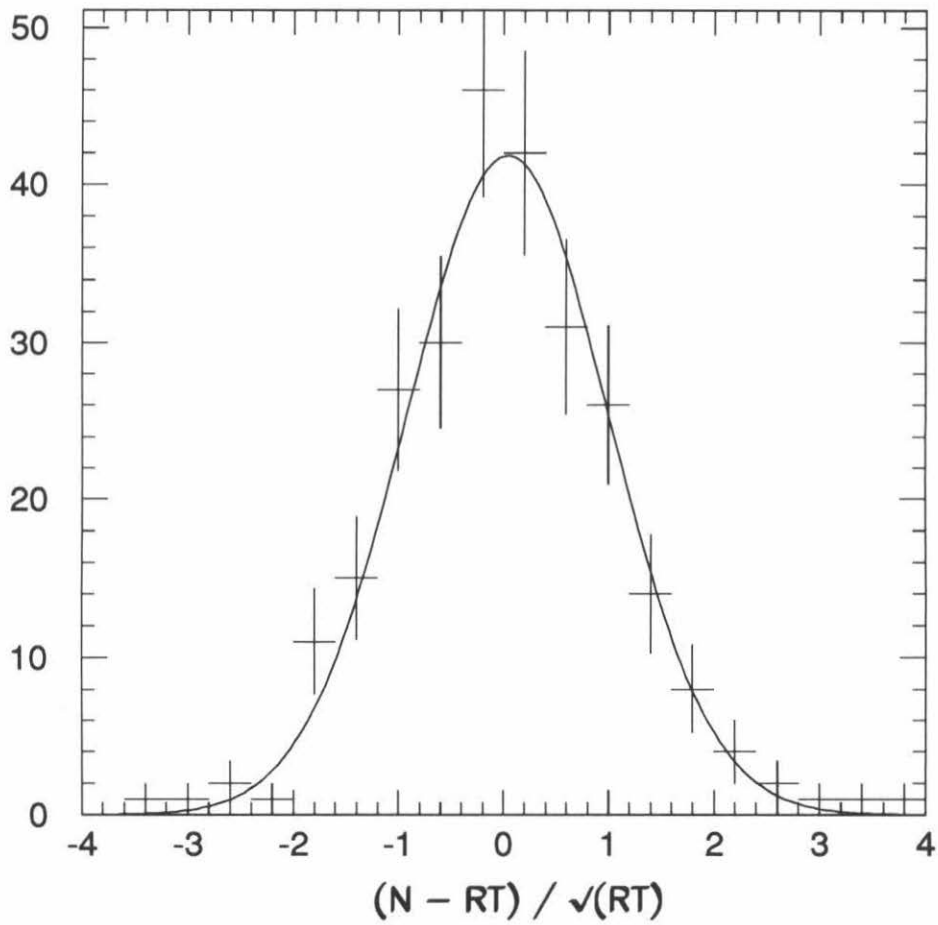

Figure 4.12: Distribution of the parameter ρ =(N–RT)/$\sqrt{\text{RT}}$, where N is the number of observed coincident events for a MACRO run, R is the average rate (79 ± 1) coincidences/day and T is the run duration (in days). The curve is a Gaussian fit with mean (0.04 ± 0.04) and standard deviation (0.96 ± 0.04).

EAS-TOP trigger	Number of coincidences	Rate (events/day)
0 (FAI)	310 ± 18	3.2 ± 0.2
1 (HEI)	582 ± 24	6.1 ± 0.3
2 (HEE)	3129 ± 56	32.6 ± 0.6
3 (LEE)	2411 ± 49	25.1 ± 0.5
4 (ITR)	778 ± 28	8.1 ± 0.3
6 (LEI)	434 ± 21	4.5 ± 0.2
all	7644 ± 87	79 ± 1

Table 4.2: Mean coincidence rates for the various EAS-TOP trigger configurations (defined in Section 3.2.1). The total combined live time is 96.3 days.

4.1.3 High-energy internal events

In most of the following analysis, we will concentrate on a special class of coincidences, namely, that of High-Energy events with a shower core Internal to the boundaries of EAS-TOP, or the so-called "trigger 1" (or HEI) events of Section 3.2.1 (see also Fig. 4.23). This is because these events are the ones best reconstructed by EAS-TOP (see Section 3.3). Fig. 4.13 shows the corrected time coincidence peak between –30 and 30 μs for these HEI events. An expanded view of the peak between –4 and 4 μs is shown at the top right corner, together with a Gaussian fit with standard deviation $(0.66 \pm 0.02)\mu$s. There are 582 such events satisfying the coincidence definition. There are 42 events in the (–30μs, 30μs) window excluding the 4.2 μs-wide coincidence region, for a background of (0.8 ± 0.1) accidentals per μs bin. In the 4.2 μs window, we therefore expect that there are (3.4 ± 0.4) background events. This represents a 170 : 1 signal-to-background ratio, or a 0.58 % background contamination. That this is less than the 1.2 % overall background (see Section 4.1.2) can be understood

from the fact that HEI events originate from higher energy primary cosmic rays than overall triggers, and therefore have a greater triggering efficiency (see Section 3.3), as well as a higher probability of yielding a high-energy muon. Therefore, a muon seen underground by MACRO coincidentally with a high-energy shower seen by EAS-TOP has a greater probability of being a true coincidence.

4.2 Comparison of the independent MACRO and EAS-TOP reconstructions

4.2.1 Example of a coincidence and details of the reconstructions

In Fig. 4.14, we depict the HEI event with highest muon multiplicity recorded. We will analyze the reconstruction of this event in detail, as an example of the whole procedure and an introduction to the technique of combining the independent reconstructions.

Firstly, this event was recorded on August 9, 1990 (221^{st} day of the year), at 14:49:18.593974 (solar time) by the MACRO clock and at 14:49:18.595836 by the EAS-TOP clock, for a $\Delta T = -1862$ μs. It occurred during MACRO run 2229, at time t = 220.6176 days since January 1, 1990, and thus using Table 4.1, we calculate that the coincidence peak location at that time was $\Delta T_{peak} = 9.09 \times 220.6176 - 3868 = -1862.6$ μs. This event satisfied Eq. 4.1: $|\Delta T_{corr}| = 0.6$ μs ≤ 2.1 μs, and was thus labeled as a coincidence.

The tracking algorithm used in DREAM to automatically reconstruct this event (see Section 2.3.2) partially failed as the algorithm reconstructed many wrong tracks due to the unusually high number of hits in the streamer tubes. However, this event was carefully scanned visually, and a study of enlarged displays of it allowed the multiplicity of tracks to be unambiguously set to 23 in each of the X and D views.

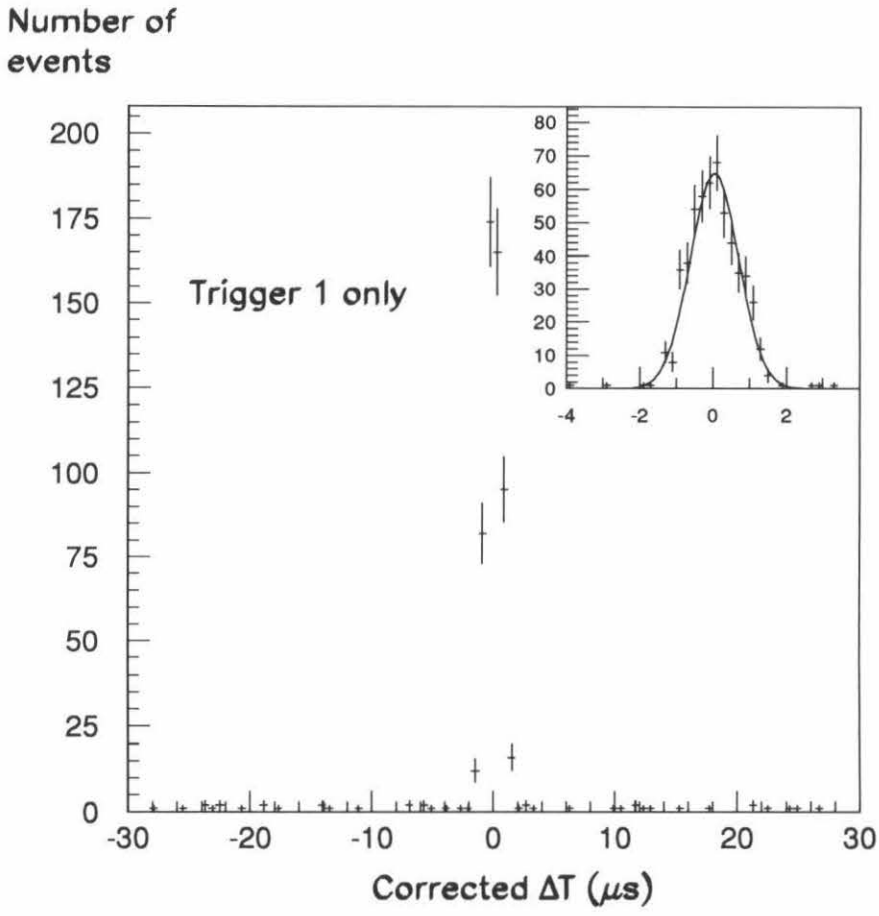

Figure 4.13: Time coincidence peak for the HEI events defined in Section 3.2.1. The top, right, plot is an expanded view of the central peak. The curve is a Gaussian fit with standard deviation $(0.66 \pm 0.02)\mu$s.

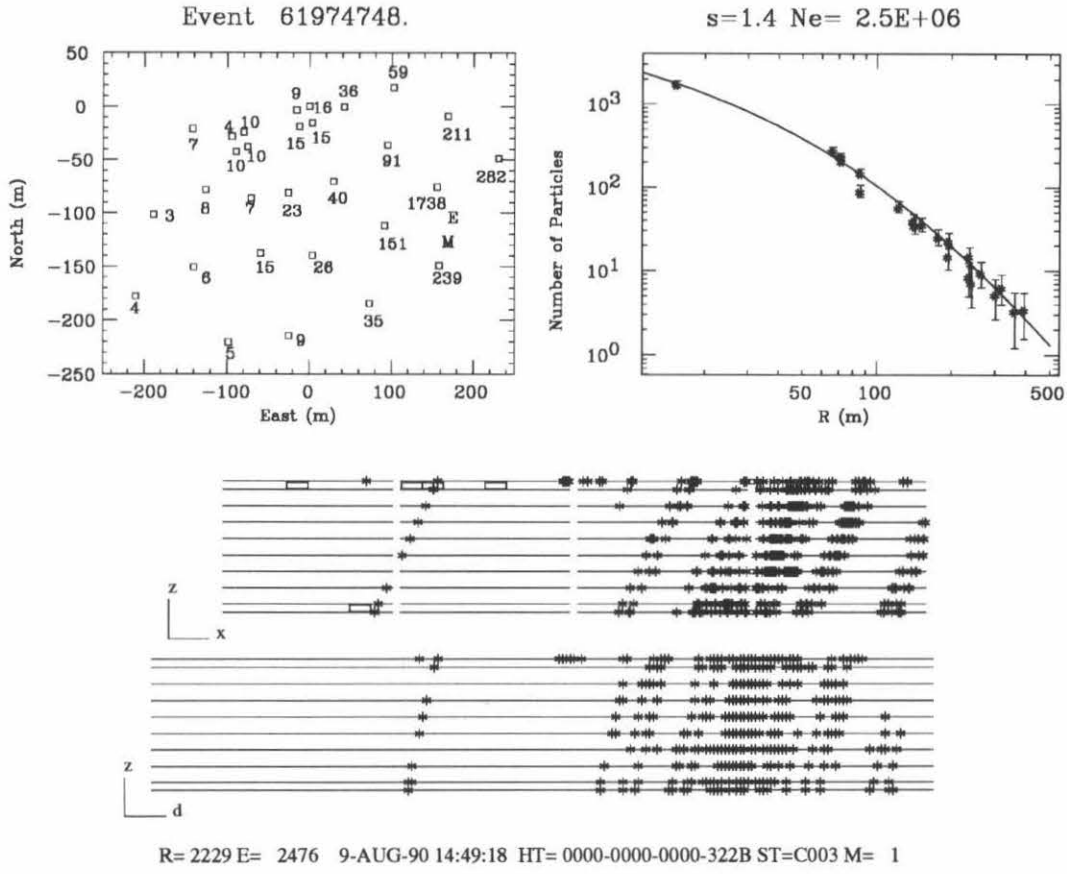

Figure 4.14: Example of a HEI (high-energy internal) event which satisfied the coincidence condition Eq. 4.1. This is not a typical event, but rather the highest multiplicity event recorded in coincidence. Shown are: 1) a map of the EAS-TOP counters giving the number of particles recorded by each, as well as the MACRO (M) and EAS-TOP (E) core locations for this event (near 180m East, –120m North), 2) the NKG reconstruction for that event, 3) a display of the muon hits recorded by MACRO along the X and D views (the resolution is much better than apparent on this picture, as the hits are drawn large for better visibility).

(In fact, all of the 582 HEI events, and all of the 434 LEI events were scanned visually so as to verify, and correct when necessary, the multiplicities assigned by the tracking algorithm.) The zenith and azimuth parameters were also wrongly determined, since their calculation utilized the mean slope of all the tracks in each view, some of which were spurious tracks caused by chance alignment of hits. Fortunately, many good tracks were reconstructed, such as the lone muon traversing the two halves of the first supermodule. Using these good tracks, the zenith and azimuth angles were recalculated (using the method of Section 2.3.2) to be $\theta_M = 34.3°$ and $\phi_M = 172.1°$.

From the distribution of hits recorded by its various counters (see Section 3.3.2), EAS-TOP reconstructs the position of the shower core to be, in a (East,North) coordinate system, $(X_E,Y_E) = (176\text{ m},-103\text{ m})$. It is marked by an "E" in Fig. 4.14. Since the counter with the greatest number of particles recorded is not on the edge of the array, this event is classified as an internal event, and since all stations of at least one subarray are hit, it is a high-energy event. Using the core location, the number of particles sampled by the various counters is plotted as a function of distance from the shower core. The NKG fit to this (see Section 3.3.3) yields a shower size of $N_e = 2.5 \times 10^6$ for this event. Timing information from the various counters is used to reconstruct the zenith and azimuth angles to be $\theta_E = 34.1°$ and $\phi_E = 168.0°$.

If ψ is defined to be the angle in space between the direction reconstructed by MACRO (θ_M,ϕ_M) and that by EAS-TOP (θ_E,ϕ_E), then ψ is given by (see Appendix B.1):

$$\cos\psi = \cos\theta_M \cos\theta_E + \sin\theta_M \sin\theta_E \cos(\phi_M - \phi_E) \tag{4.2}$$

Using this, we calculate that $\psi = 2.3°$ for this event.

Fig. 4.15 shows the relative positions and orientation of the coordinate systems used by the two detectors. It is possible to extrapolate the MACRO track (or the average track for multimuon events, see Section 2.3.2) back to the altitude of EAS-TOP to estimate the location of the shower core; this is useful because high-energy muons

are the progeny of mesons created with relatively low transverse momentum, and therefore remain close to the core even after propagating through tens of kilometers of air and one kilometer of rock (see Reference [14], p.129). A track intersecting the floor of the tunnel at MACRO coordinates (x,y) and with angular direction (θ_M,ϕ_M) extrapolates to the ground surface to yield a core location given by (in (East,North) coordinates):

$$\begin{cases} X_M = \Delta E + x \cdot \sin\alpha + y \cdot \cos\alpha + \Delta Z \cdot \tan\theta_M \sin\phi_M \\ Y_M = \Delta N - x \cdot \cos\alpha + y \cdot \sin\alpha + \Delta Z \cdot \tan\theta_M \cos\phi_M \end{cases} \tag{4.3}$$

where $\Delta E = E_M - E_E = 62$ m, $\Delta N = N_M - N_E = 544$ m and $\Delta Z = Z_E - Z_Z = 1041$ m are the separations between the MACRO and EAS-TOP origins along the East, North and Up directions, respectively, and $\alpha = 51.6°$ is the tilt of the MACRO y axis from North (these parameters were measured by a surveying firm; the estimated uncertainty on distances is on the order of 1 m). For the particular event studied here, the coordinates of the core location as determined by MACRO using Eq. 4.3 are (X_M,Y_M) = (169 m,–126 m). It is marked by an "M" in Fig. 4.14. Thus, the separation between the MACRO and EAS-TOP core locations is $\Delta R = \sqrt{(X_M - X_E)^2 + (Y_M - Y_E)^2} = 24$ m.

4.2.2 Comparison of the angular reconstructions

Fig. 4.16 shows a scatterplot of MACRO zenith angles versus azimuth angles for 580 of the 582 HEI coincidences (two events were unreconstructible because of an over-abundance of hits in the streamer tubes due to electronic noise). A clear grouping of events can be seen, corresponding to the solid angle window subtended by EAS-TOP at MACRO. The outlying events are due to muons having been deflected in propagating through the rock, because of bremsstrahlung, multiple Coulomb scattering, etc. However, two events (marked by arrows in Fig. 4.16) stand so far outside the group that they can be labeled as candidates for chance coincidences. Both events

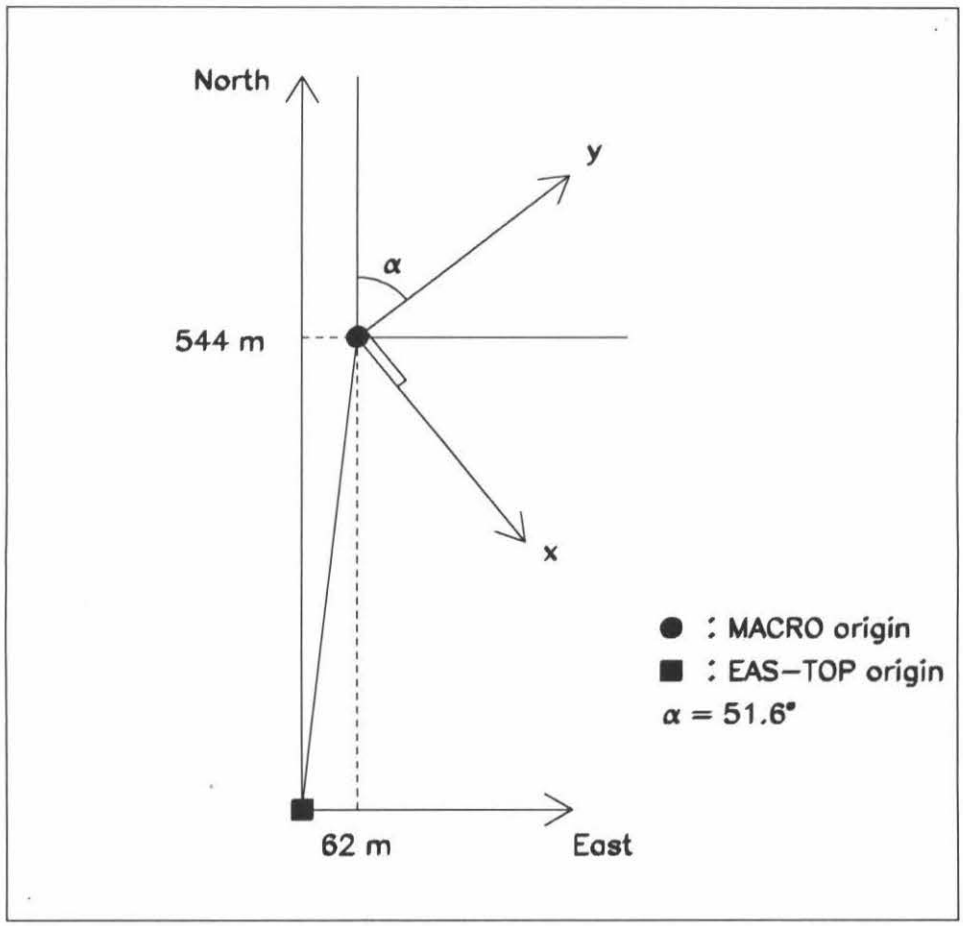

Figure 4.15: Relative positions and orientation of the MACRO and EAS-TOP coordinate systems. In MACRO, azimuth angles are measured counterclockwise relative to North, not to the MACRO x axis.

feature clean, well-reconstructed, single muon tracks. In fact, for this trigger configuration, we expect (3.4 ± 0.4) background events for 96 days of live time, as described in Section 4.1.3.

In contrast to Fig. 4.16, in Fig. 4.17 we show a scatterplot of MACRO zenith angles versus azimuth angles for events outside the 4.2 μs-wide time-coincidence window defined by Eq. 4.1. For clarity, only events from MACRO runs 2156 to 2190 (about 4% of the data) are shown. The structure that is apparent on the figure is due to the shape of the mountain above MACRO: regions of lesser density on this figure correspond to directions of greater rock thickness, and vice-versa (see Section 2.4). Since EAS-TOP lies in the direction of least overburden, the region around 190° in azimuth and 33° (see Fig. 4.16) is one of relatively high density. However, the absence of clustering on this figure around the roughly diamond-shaped region of Fig. 4.16 is an indication that this sample does not contain an appreciable number of coincident events, and that the timing cut of Section 4.1 identifies them efficiently.

Fig. 4.18 shows EAS-TOP zenith angles versus azimuth angles, for all 582 HEI events. Outlying events are due mostly to scattered muons; for these, showers reconstructed by EAS-TOP as not quite pointing to MACRO were accompanied by a muon that scattered in just the right direction so as to trigger the underground detector. The two candidate background events of Fig. 4.16 are also marked by arrows. For one of them, the reconstructed EAS-TOP direction lies clearly outside the "cloud" of coincident events. The other is marginal.

Fig. 4.19 shows the distribution of differences between the MACRO and EAS-TOP zenith angles, and Fig. 4.20 shows the corresponding distribution for azimuth angles. Each distribution is well fitted by a Gaussian. The mean zenith difference of $(0.06 \pm 0.05)°$ is consistent with there being no bias in the relative zenith angle reconstructions. However, the mean azimuth difference of $(0.94 \pm 0.09)°$ is not understood and is being studied. It could mean that the measured orientation of

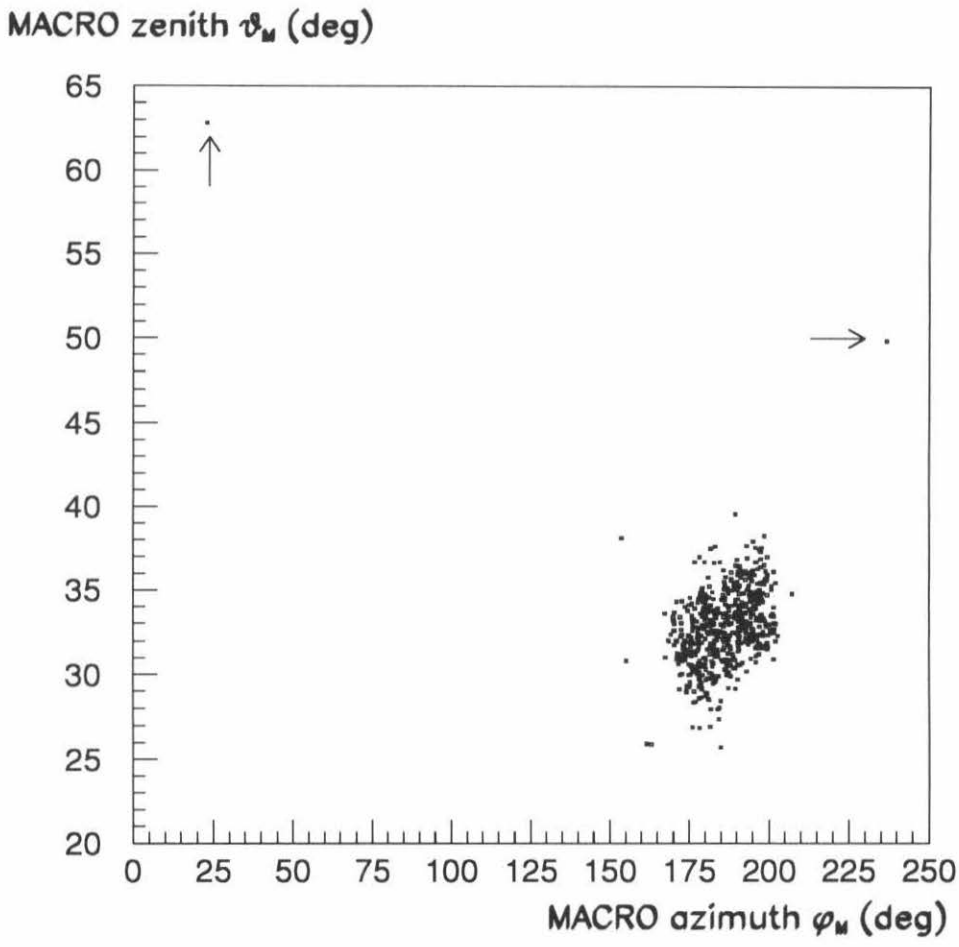

Figure 4.16: MACRO zenith angle versus azimuth angle for HEI coincident events. The arrows point to two candidate accidental coincidences.

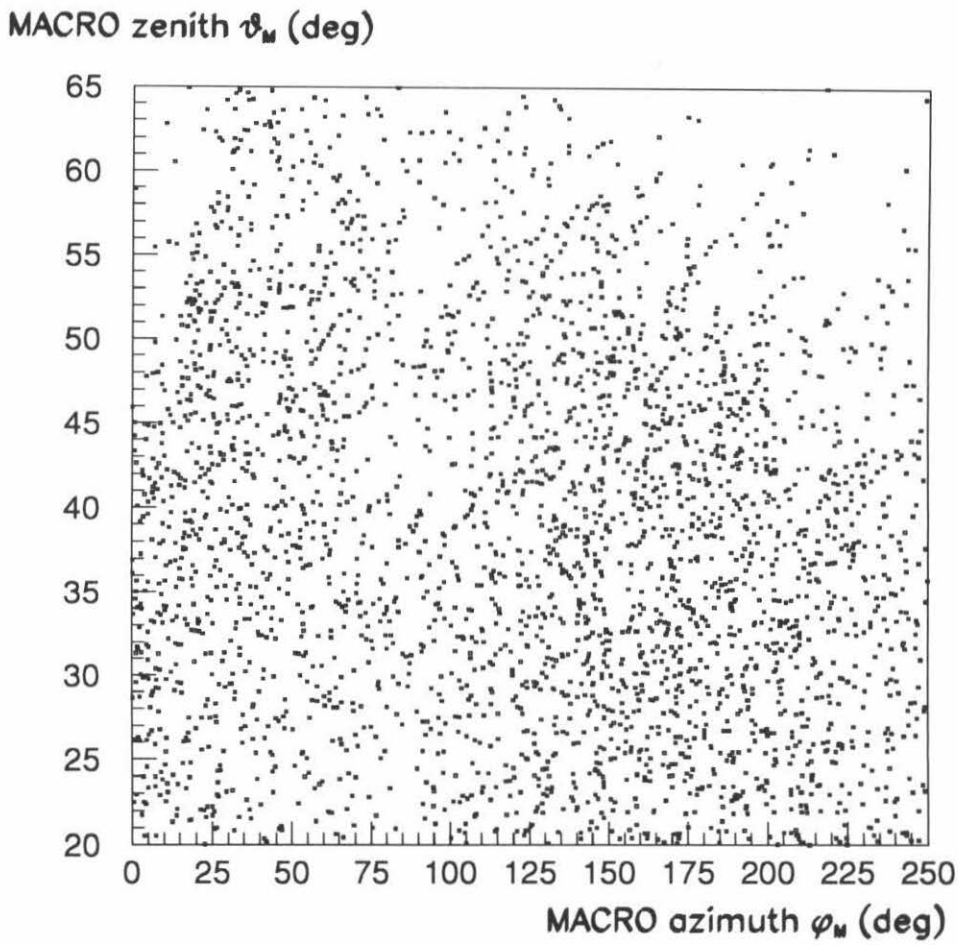

Figure 4.17: MACRO zenith angle versus azimuth angle for events outside the time-coincidence window defined by Eq. 4.1. The structure reflects the shape of the mountain above MACRO.

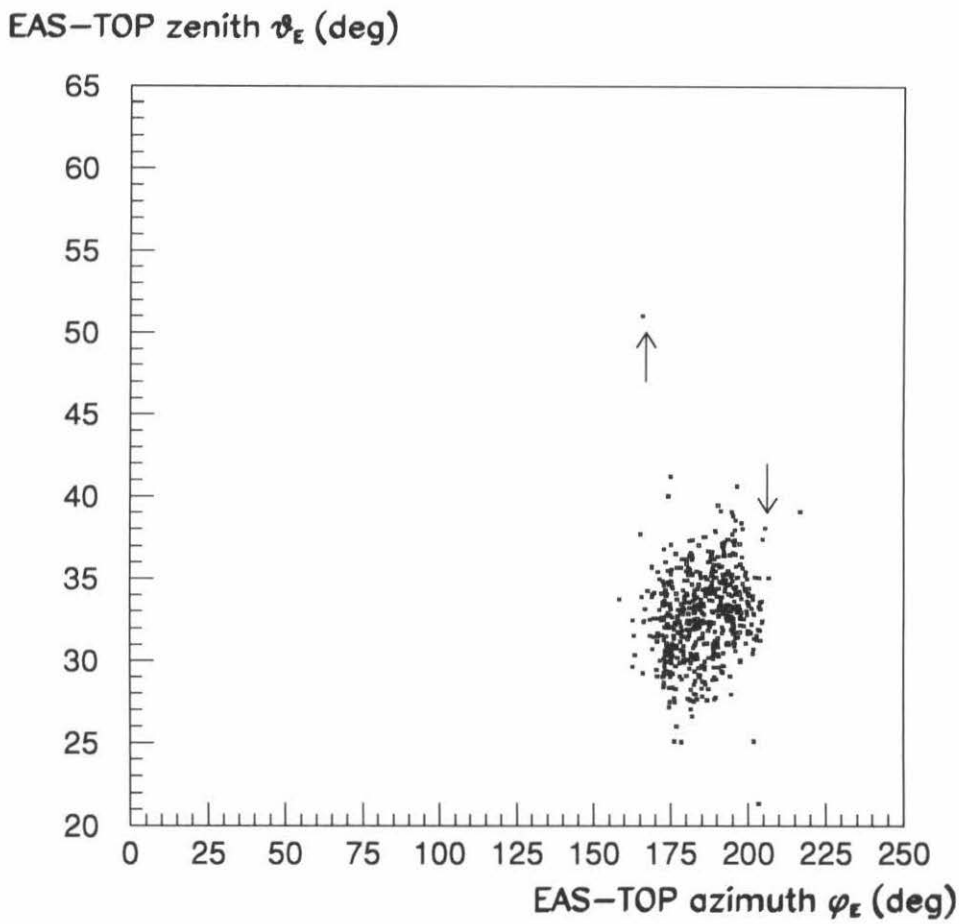

Figure 4.18: EAS-TOP zenith angle versus azimuth angle for HEI events. The arrows point to the two candidate accidental coincidences of Fig. 4.16.

MACRO with respect to North is wrong by one degree. EAS-TOP has been able to track the shadow of the Sun and the Moon (see Section 3.3.1), and has therefore demonstrated that its absolute orientation is known. Whatever the source of this bias, it is of no concern for this work, for it is of the same order as the angular resolutions (see Sections 2.4 and 3.3), and angular reconstructions are used only as a means of eliminating chance coincidences (however, it is a concern for MACRO muon astronomy studies such as that of Reference [56]). The values of $\Delta\theta$ and $\Delta\phi$ for the two candidate background events of Fig. 4.16 further support the claim that they are indeed accidental coincidences (see the captions of Fig. 4.19 and Fig. 4.20). The tails of the two distributions are non-Gaussian, owing to the systematic errors in the reconstructions discussed in Sections 2.3.2 and 3.3.

The distribution of ψ, the angle in space between the MACRO and EAS-TOP directions defined by Eq. 4.2, is shown in Fig. 4.21. The mean angle is $\overline{\psi} = (1.90 \pm 0.07)°$; 90% of all events are reconstructed to within 3.5°. The 1.9° mean angle is a convolution of the $\sim 0.5°$ accuracy with which MACRO reconstructs the primary direction in space from the muon tracks (see Section 2.4), and the EAS-TOP angular resolution of about 0.8° for HEI events (see Section 3.3.1).

In understanding the distribution of the directional differences, it is more transparent to study $(1 - \cos\psi)$ rather than ψ (see Appendix B.1; for small angles, this parameter is $\frac{1}{2}\psi^2$). Fig. 4.22 shows the experimental distribution of $(1 - \cos\psi)$. As expected, it is exponential, with a slope of $(4.4 \pm 0.2) \times 10^{-4}$, in agreement with the Appendix B.1 "prediction" of 4.6×10^{-4}. The departures from exponentiality at values of $(1 - \cos\psi)$ greater than about 0.002 are reflections of the non-Gaussian tails of the distributions of Figs. 4.19 and 4.20.

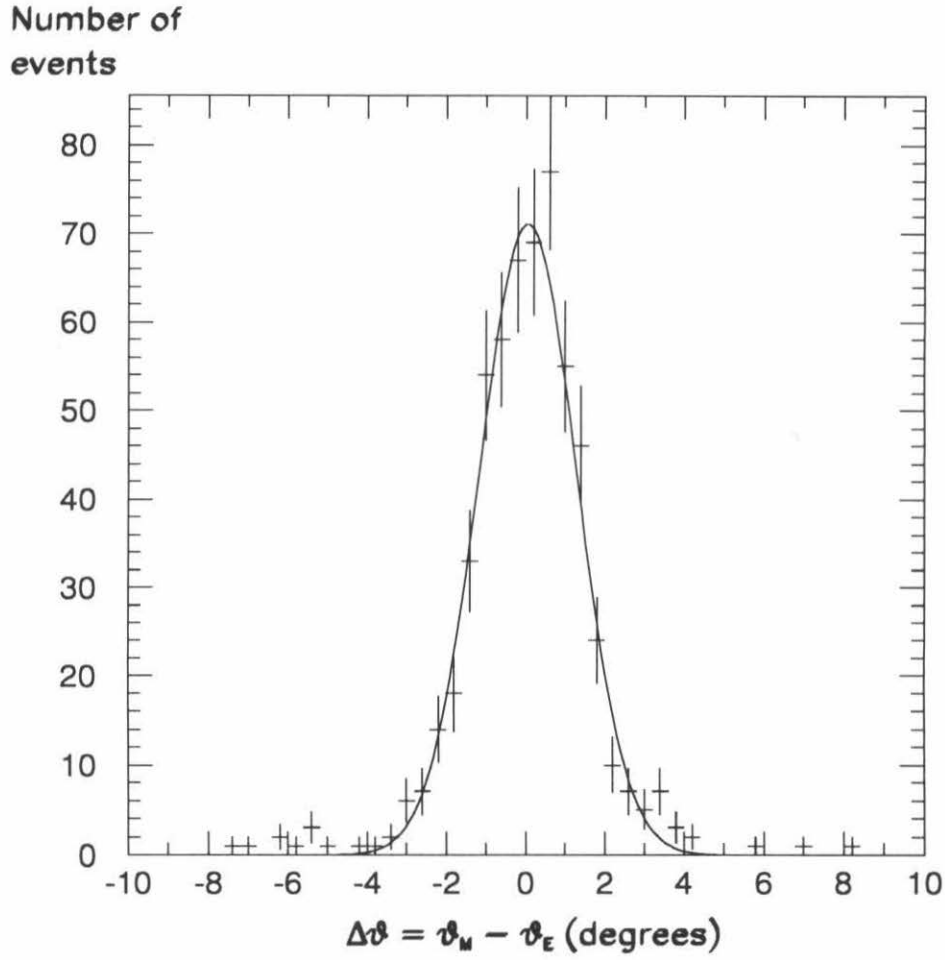

Figure 4.19: Distribution of zenith angle differences $\Delta\theta = \theta_{\rm M} - \theta_{\rm E}$ for HEI events. The curve is a Gaussian fit with mean $(0.06 \pm 0.05)^\circ$ and standard deviation $(1.23 \pm 0.05)^\circ$. The two candidate background events have $\Delta\theta = -0.8^\circ$ and 24.7°, respectively.

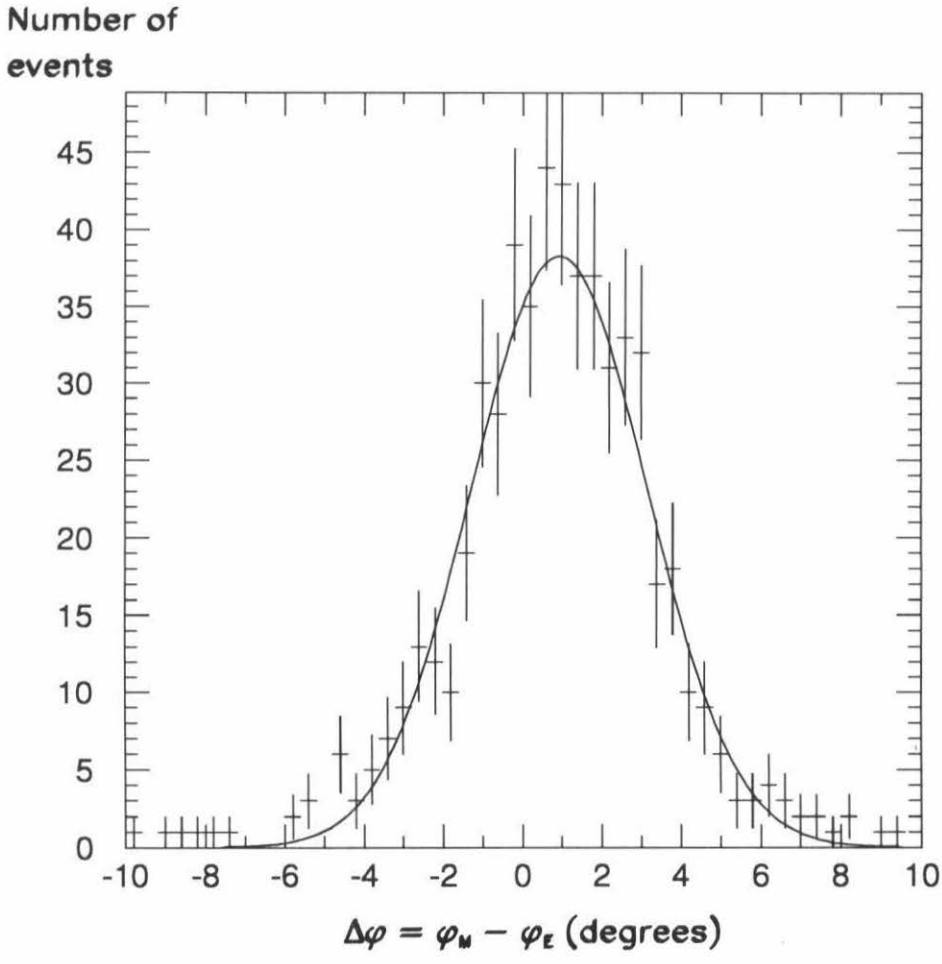

Figure 4.20: Distribution of azimuth angle differences $\Delta\phi = \phi_{\rm M} - \phi_{\rm E}$ for HEI events. The curve is a Gaussian fit with mean $(0.94 \pm 0.09)^\circ$ and standard deviation $(2.22 \pm 0.09)^\circ$. The tails are not Gaussian, however, with 14 events overflowing the bounds of the plot. The two candidate background events have $\Delta\phi = 69.2^\circ$ and -182.5°, respectively.

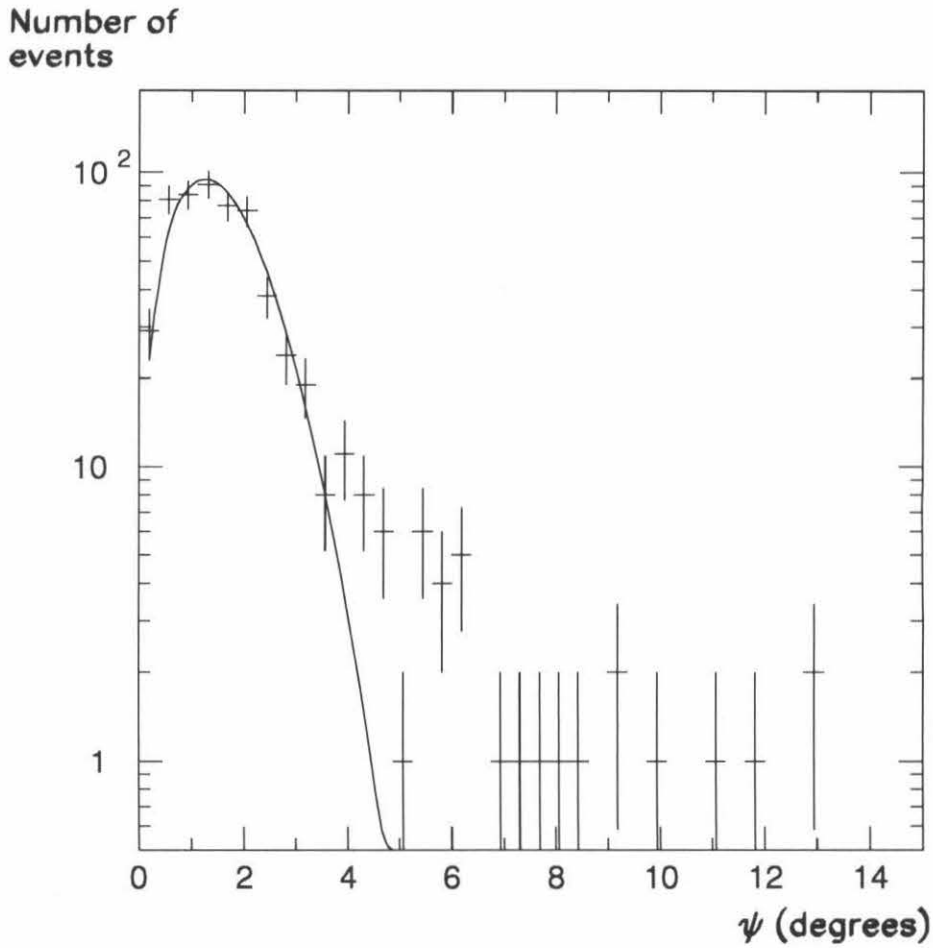

Figure 4.21: Distribution of the space angle ψ between the MACRO and EAS-TOP reconstructed directions for HEI events, as defined by Eq. 4.2. The mean of the distribution is $(1.90 \pm 0.07)^\circ$, and the "90% mark", *i.e.*, the angle within which 90% of all events are reconstructed, is 3.5°. The two candidate background events have $\psi = 51.9^\circ$ and 101.1°, respectively. 30 events overflow the boundaries of the plot as it is drawn. The curve is a $A\psi \exp(\frac{1}{2}\psi^2/\sigma^2)$ fit, with $\sigma = (1.26 \pm 0.04)^\circ$.

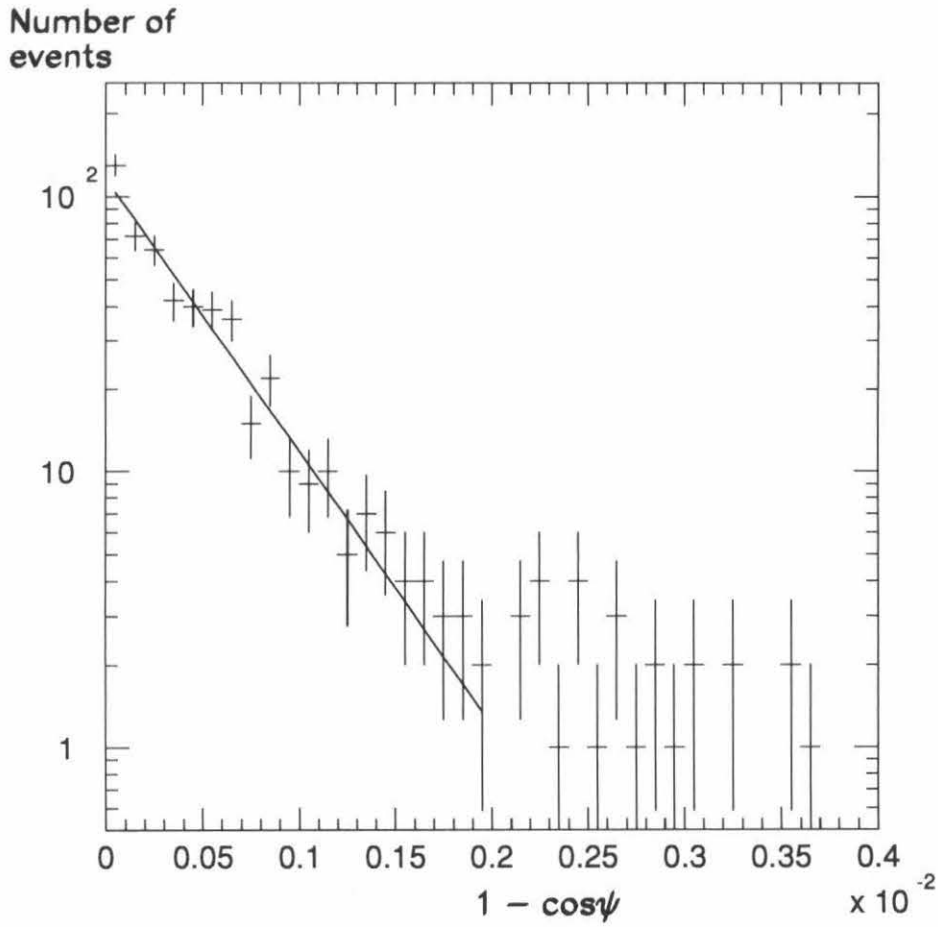

Figure 4.22: Distribution of $(1 - \cos\psi)$ for HEI events. The curve is an exponential fit with slope $(4.4 \pm 0.2) \times 10^{-4} = ((2.1 \pm 0.1) \times 10^{-2})^2 = ((1.2 \pm 0.1)^\circ)^2$ (compare with the fit of Fig. 4.21). 28 events overflow the boundaries of the plot.

4.2.3 Comparison of the core location reconstructions

In Fig. 4.23, we show a scatterplot of core locations in (East,North) coordinates as reconstructed by EAS-TOP for HEI events, superimposed onto a map of the various counters projected along the line of sight to MACRO onto a horizontal plane. It also shows one particular trigger subarray (see Section 3.2.1), together with the distribution of core locations for events having triggered it. The visible clustering of events around each inner counter is evidence that the trigger sensitivity is not quite uniform over the surface of the array, even for the high-energy showers corresponding to the HEI configuration. Fig. 4.24 shows the equivalent scatterplot for shower cores calculated by MACRO by extrapolation of the muon tracks back to the surface (see Eq. 4.3). The internal structure of the distribution has been lost due to scattering of the muons and detector resolution effects, which in the mean cause a $\sim 0.5°$ deflection (see Section 2.4), or about 9 m perpendicularly after 1 km of travelling through rock, or a shift of about 10 m in shower core location. A few muons have scattered by relatively large angles, so that their extrapolated core locations are well outside the boundaries of the array.

Figs. 4.25 and 4.26 show the distributions of differences between the MACRO and EAS-TOP core location East (X) and North (Y) coordinates, respectively. Both of them are fitted with Gaussians, and both have non-Gaussian tails. For the East differences, the mean and standard deviation of the Gaussian are $(-0.4\pm\ 0.6)$ m and (14.5 ± 0.6) m, respectively. For the North differences, the mean and standard deviation are (3.6 ± 0.7) m and (16.8 ± 0.8) m, respectively. The departure of the mean from zero for the North differences is related in part to that of azimuth angle differences from zero (see Fig. 4.20) by Eq. 4.3, where ϕ_M is near 180° (see Fig. 4.16). However, this accounts only for 29% of the discrepancy, and there remains an unresolved systematic offset of about 2.5 m, probably due to uncertainties in the surveyed positions of the two origins, which are accurate to the order of 1 m. Again,

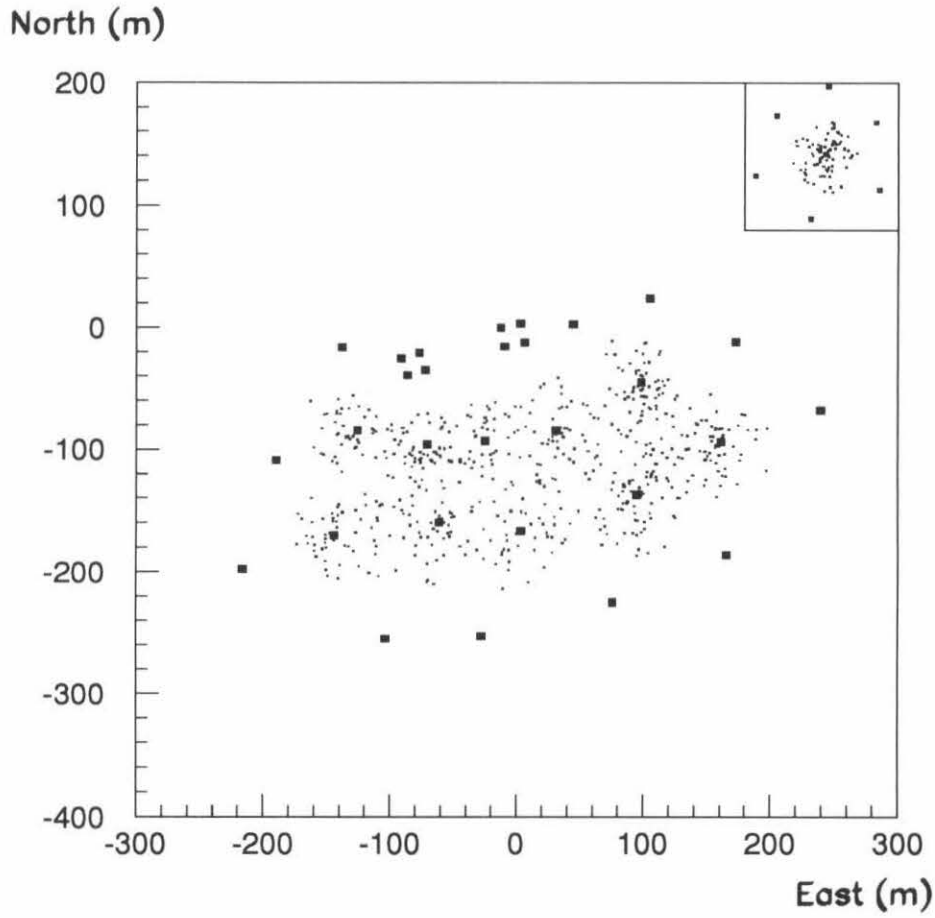

Figure 4.23: Map of the location of the shower cores as reconstructed by EAS-TOP for HEI events, superimposed onto a map of the EAS-TOP counters. The insert at the top, right, shows the trigger subarray centered at about (East,North) = (110 m,–150 m) (counter L of Fig. 3.1), and the distribution of core locations for events having triggered it.

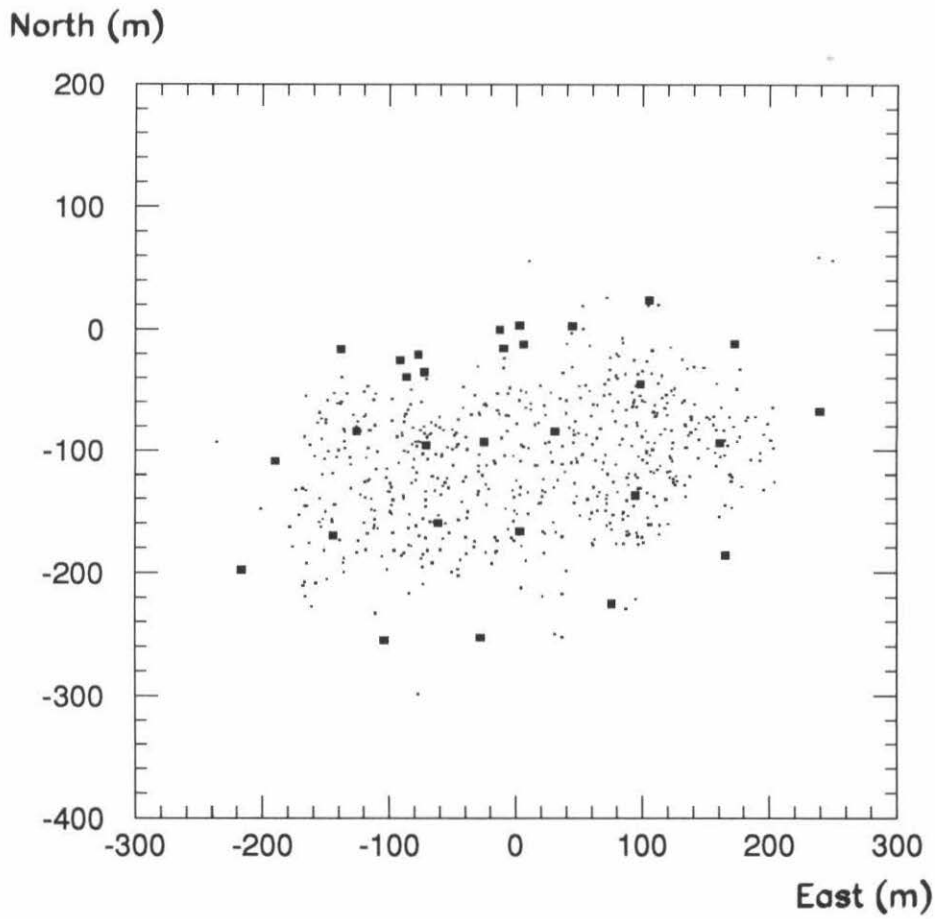

Figure 4.24: Map of the location of the shower cores as extrapolated by MACRO for HEI events, superimposed onto a map of the EAS-TOP counters. Four events (including the two background candidates) overflow the plot.

this is of no concern in this thesis.

Fig. 4.27 shows the distribution of the separation between the MACRO and EAS-TOP core locations. The mean separation is $\overline{\Delta R} = (24 \pm 1)$ m, and 90% of all events agree to within 44 m. This mean of 24 m is not quite compatible with a convolution of the 10 m core deviation arising from muon deflections and MACRO angular resolution (see above) with the EAS-TOP core location resolution of about 10 m for HEI events (see Section 3.3.2). This is not entirely understood, but again does not affect the conclusions of this work.

A more transparent distribution is that of $(\Delta R)^2$ (see Appendix B.2), and it is plotted in Fig. 4.28. As expected, it is approximately exponential, with slope (430 ± 20) m^2, compared with the "prediction" of 450 m^2 of Appendix B.2. The departures from exponentiality at values of $(\Delta R)^2$ greater than about 2000 m^2 reflect the non-Gaussian tails of the distributions of Figs. 4.25 and 4.26.

Note: from here on, we shall remove the two candidate background events from all experimental distributions shown for HEI events, as the evidence presented in Sections 4.2.2 and 4.2.3 clearly makes the separate MACRO and EAS-TOP reconstructions incompatible for them, and their number is in agreement with background expectations. We shall consider the sample of HEI coincident events to be background-free. In the next Section, some experimental distributions for LEI (low-energy, internal events) will be shown; for these, a systematic comparison of MACRO and EAS-TOP reconstructions was not performed because of difficulties encountered in reconstructing events with fewer than six contiguous EAS-TOP counters hit. LEI events will be contaminated by a small percentage of accidental coincidences (on the order of 1%). However, in quantitatively analyzing coincident events in comparison with Monte Carlo calculations, in Chapter 6, in the context of the primary composition problem, we shall consider only the well-reconstructed HEI events.

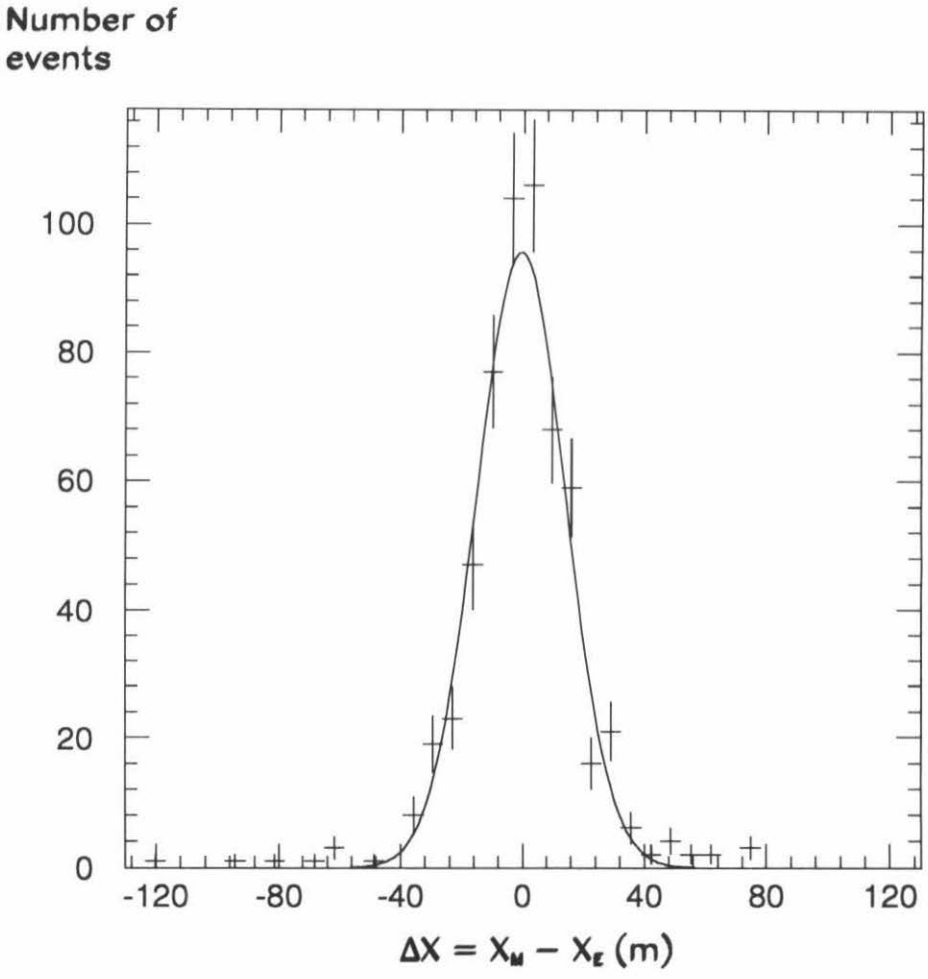

Figure 4.25: Distribution of differences between the East coordinate of the core location determined by MACRO and that by EAS-TOP. The curve is a Gaussian fit with mean $(-0.4\pm\ 0.6)$ m and standard deviation $(14.5\ \pm\ 0.6)$ m. Five events (including the two background candidates) overflow the plot.

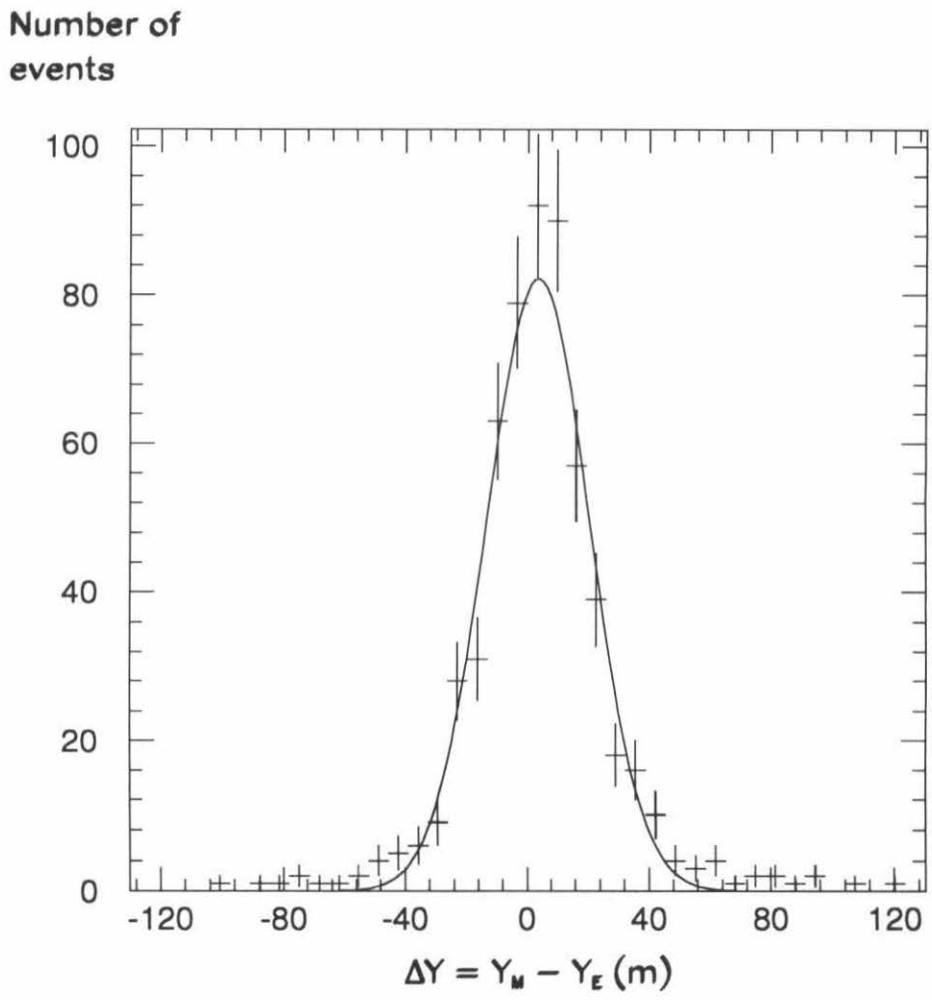

Figure 4.26: Distribution of differences between the North coordinate of the core location determined by MACRO and that by EAS-TOP. The curve is a Gaussian fit with mean (3.6 $\pm$ 0.7) m and standard deviation (16.8 $\pm$ 0.8) m. Three events (including the two background candidates) overflow the plot.

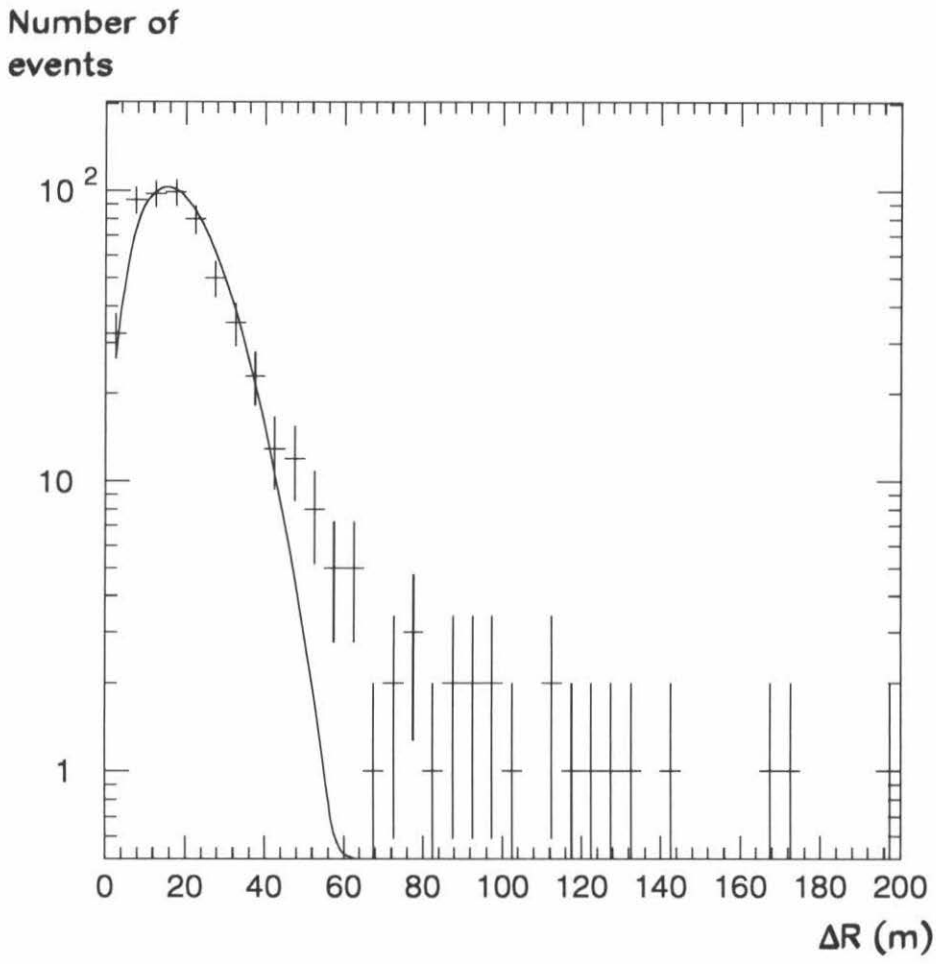

Figure 4.27: Distribution of the separation between the MACRO and EAS-TOP core locations (in meters). The mean of the distribution is (24 $\pm$ 1) m, and the "90% mark" is at 44 m. Three events overflow the plot, two of them dramatically with ΔR = 850 m and 2804 m, respectively (the two candidate background events). The curve is a $A(\Delta R)\exp(\frac{1}{2}(\Delta R)^2/\sigma^2)$ fit, with $\sigma = (15.4 \pm 0.5)$m.

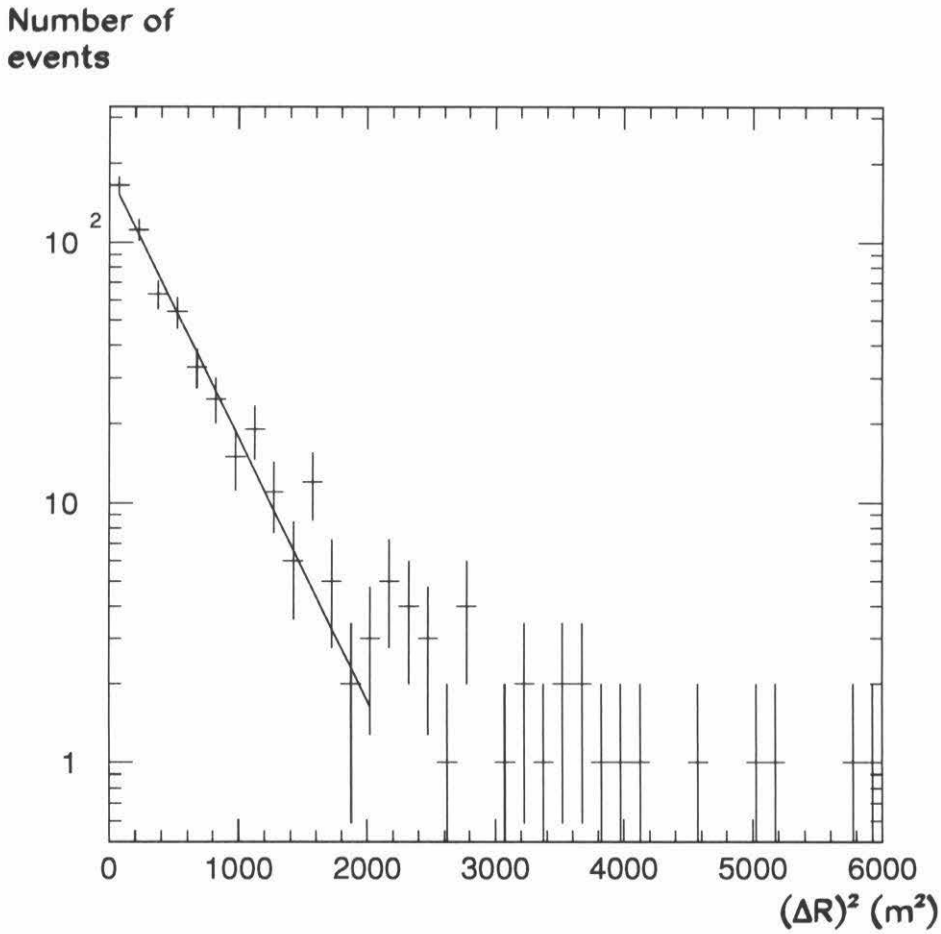

Figure 4.28: Distribution of the square of the separation between the MACRO and EAS-TOP core locations (in m^2). The curve is an exponential fit with slope $(430 \pm 20)m^2 = ((21 \pm 1)m)^2$. The discrepancy between the slope here and the parameter σ of the fit of Fig. 4.27 is due to the nonzero mean of the ΔY distribution of Fig. 4.26. 22 events overflow the boundaries of the plot.

4.3 Muon multiplicity and shower size distributions for coincidences

4.3.1 Muon multiplicity distributions

In Fig. 4.29, we show the muon multiplicity distributions reconstructed by MACRO for internal coincidences (HEI and LEI events) in comparison with the distribution obtained by MACRO alone (Fig. 2.11). For each multiplicity, the number of events is normalized to the number of single muon events for that particular trigger configuration. The mean multiplicities are:

$$\begin{aligned} &\text{MACRO alone:} && \overline{N}_\mu{}^{MAC} &&= (1.06 \pm 0.02) \\ &\text{LEI:} && \overline{N}_\mu{}^{LEI} &&= (1.18 \pm 0.03) \\ &\text{HEI:} && \overline{N}_\mu{}^{HEI} &&= (1.74 \pm 0.08) \end{aligned}$$

An increase in primary threshold energy due to the various trigger configurations (from $\sim 10^4$ GeV for MACRO alone, to $\sim 1.5 \times 10^5$ GeV for HEI events) yields an increase in mean muon multiplicity deep underground due to an increase in the proportion of high-multiplicity events. Table 4.3 shows the number of events of each multiplicity recorded by MACRO alone (with two supermodules) and in coincidence with EAS-TOP HEI or LEI events. In it, the standalone-MACRO multiplicities are corrected after a sample of events has been visually scanned, and the error bars include a systematic uncertainty to account for this (see Reference [23]). For large multiplicities, sometimes only a range of possible multiplicities can be estimated, and each possible multiplicity in that range is given an equal fractional weight (hence some fractional numbers of events in Table 4.3). For the HEI and LEI samples, all events have been visually scanned; the scanned multiplicities being unambiguous in all cases, no systematic uncertainty is introduced. Note that the standalone-MACRO muons have traversed a 3700 m.w.e. thickness of rock on the average, whereas those

for coincidences have traversed about 3250 m.w.e., and the two categories of events really correspond to muons with different distributions of energy entering the ground. However, the comparison is done here for qualitative purposes only.

In Fig. 4.30 we present the MACRO muon multiplicity distributions for HEI coincidences divided into four regions of EAS-TOP shower sizes. The mean muon multiplicities for the four windows are:

$$4.2 < \log(N_e) \leq 4.7 : \quad \overline{N}_\mu = (1.26 \pm 0.04)$$
$$4.7 < \log(N_e) \leq 5.2 : \quad \overline{N}_\mu = (1.45 \pm 0.05)$$
$$5.2 < \log(N_e) \leq 5.7 : \quad \overline{N}_\mu = (2.3 \pm 0.2)$$
$$5.7 < \log(N_e) : \quad \overline{N}_\mu = (6 \pm 1)$$

Here again, an increase in shower size and thus in primary energy corresponds to an increase of the mean muon multiplicity observed in coincidence deep underground. Table 4.4 gives the number of events of each multiplicity for each shower size window.

4.3.2 Shower size distributions

Fig. 4.31 shows the distribution of shower sizes reconstructed by EAS-TOP for HEI events divided in two windows of underground muon multiplicities. The mean shower sizes are:

$$N_\mu \leq 2 : \quad \overline{\log N_e} = (4.88 \pm 0.02)$$
$$N_\mu \geq 3 : \quad \overline{\log N_e} = (5.27 \pm 0.05)$$

The high muon multiplicity window corresponds to a higher primary energy and therefore to a higher mean shower size.

Fig. 4.32 shows a scatterplot of muon multiplicities in MACRO for HEI coincidences as a function of shower sizes reconstructed by EAS-TOP. The linear correlation coefficient for the distribution is $r = 0.44$. For 580 events, the probability that

N_μ	MACRO alone (in 1195 h)	HEI (in 2400 h)	LEI (in 2400 h)
1	268700 ± 6200	394	377
2	10400 ± 250	104	43
3	1620 ± 69	40	8
4	566 ± 35	17	5
5	201 ± 16	6	0
6	102 ± 10	3	1
7	69 ± 9	7	
8	39 ± 7	2	
9	19 ± 5	3	
10	11 ± 4	0	
11	8.5 ± 2.9	0	
12	4.8 ± 2.2	0	
13	5.8 ± 2.4	0	
14	4.3 ± 2.1	0	
15	1.3 ± 1.1	1	
16	1.7 ± 1.3	0	
17	2.2 ± 1.5	1	
18	1.3 ± 1.1	0	
19	0.5 ± 0.5	0	
20	0.3 ± 0.3	0	
21	0.3 ± 0.3	0	
22	0.3 ± 0.3	0	
23	0	2	
24	0		
25	0		
26	0		
27	1 ± 1		
total:	281800 ± 6500	580 ± 24	434 ± 21
$\overline{N}_\mu$:	1.06 ± 0.02	1.74 ± 0.08	1.18 ± 0.03

Table 4.3: Number of events of each muon multiplicity recorded by MACRO alone (with two supermodules) and in coincidence with EAS-TOP internal events (HEI and LEI events). For coincidences, the uncertainty on the number of events of any multiplicity is the square root of that number.

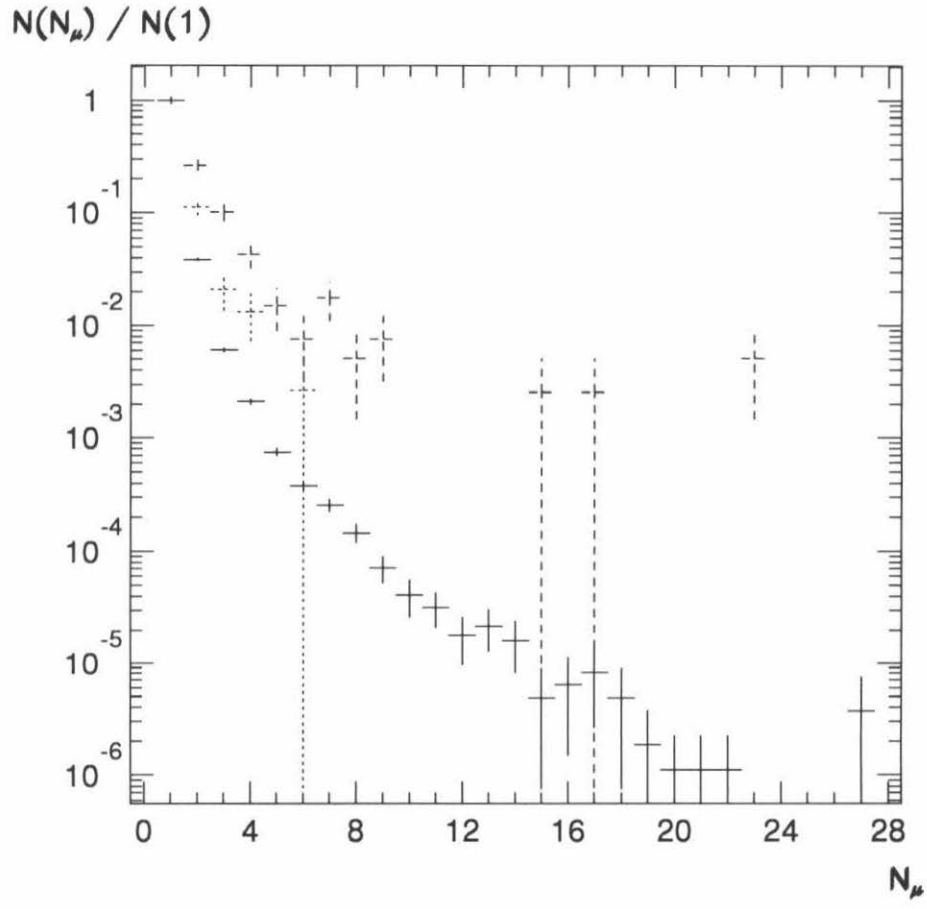

Figure 4.29: Muon multiplicity distributions for MACRO alone (solid lines), low-energy internal (LEI) coincidences (dotted lines) and high-energy internal (HEI) coincidences (dashed lines). Each distribution is normalized to its number of single muons. The distribution for MACRO alone is that of Fig. 2.11 (see Reference [23]). The points with error bars extending to the bottom of the graph are obtained with a single event of the given multiplicity. The mean multiplicities are (1.06 ± 0.02), (1.18 ± 0.03) and (1.74 ± 0.08), respectively.

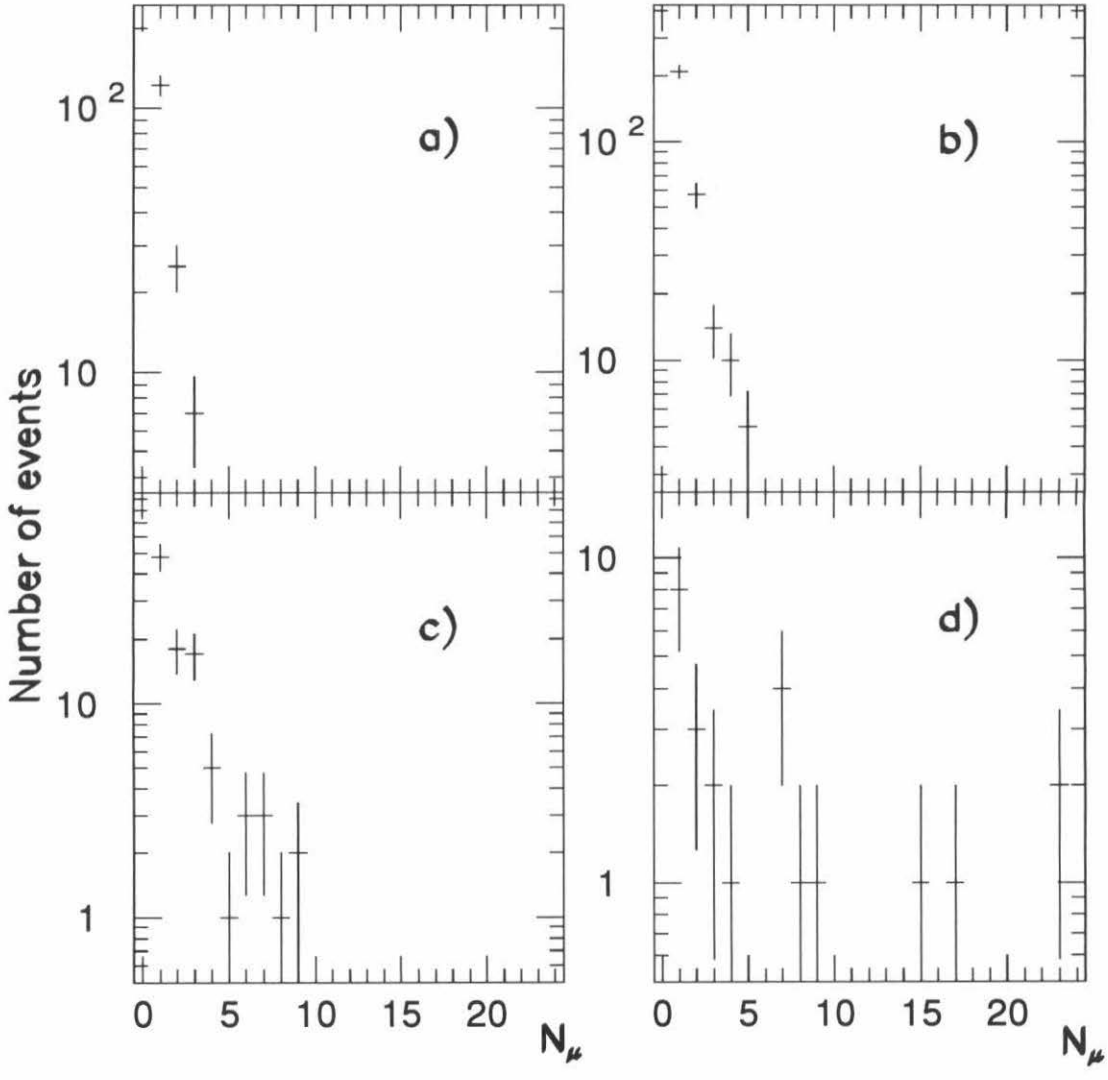

Figure 4.30: Muon multiplicity distributions for HEI coincidences in four shower size windows: a) $4.2 < \log(N_e) \leq 4.7$, b) $4.7 < \log(N_e) \leq 5.2$, c) $5.2 < \log(N_e) \leq 5.7$ and d) $5.7 < \log(N_e)$. The mean multiplicities are: a) (1.26 ± 0.04), b) (1.45 ± 0.05), c) (2.3 ± 0.2) and d) (6 ± 1).

N_μ	$4.2 \rightarrow 4.7$	$4.7 \rightarrow 5.2$	$5.2 \rightarrow 5.7$	$5.7 \rightarrow$
1	121	209	48	8
2	25	56	18	3
3	7	13	17	2
4		10	5	1
5		5	1	0
6			3	0
7			3	4
8			1	1
9			2	1
10				0
11				0
12				0
13				0
14				0
15				1
16				0
17				1
18				0
19				0
20				0
21				0
22				0
23				2
total:	153 ± 12	293 ± 17	98 ± 10	24 ± 6
$\overline{N}_\mu$:	1.26 ± 0.04	1.45 ± 0.05	2.3 ± 0.2	6 ± 1

Table 4.4: Number of events of each muon multiplicity for HEI coincidences in four shower size windows (the ranges indicate $\log(N_e)$ intervals). The uncertainty on the number of events of any multiplicity is the square root of that number.

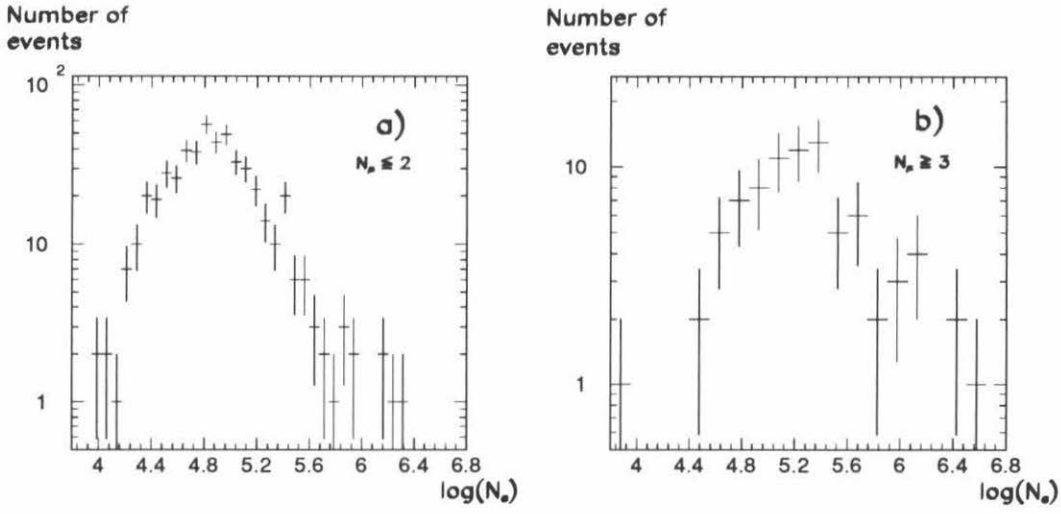

Figure 4.31: Shower size distributions for HEI coincidences in two muon multiplicity windows: a) $N_\mu \leq 2$ and b) $N_\mu \geq 3$. The mean shower sizes $\overline{\log(N_e)}$ are: a) (4.88 $\pm$ 0.02) and b) (5.27 $\pm$ 0.05).

r is this large or larger if the distributions of N_μ and $\log(N_e)$ are uncorrelated is $\mathrm{erfc}(0.44/\sqrt{580/2}) = 7 \times 10^{-26}$ (see Reference [73], p.485).

4.4 Anticoincidences

4.4.1 Definition and rates

Anticoincident events are defined as MACRO events, reconstructed to point to a fiducial area well within the boundaries of EAS-TOP, that occurred during a period of simultaneous operation of both detectors, without triggering the surface array. These correspond to relatively low-energy primary cosmic rays, in the approximate range from a few times 10^3 GeV to a few times 10^5 GeV, that have enough energy to generate a muon deep underground, but not enough to trigger the surface array.

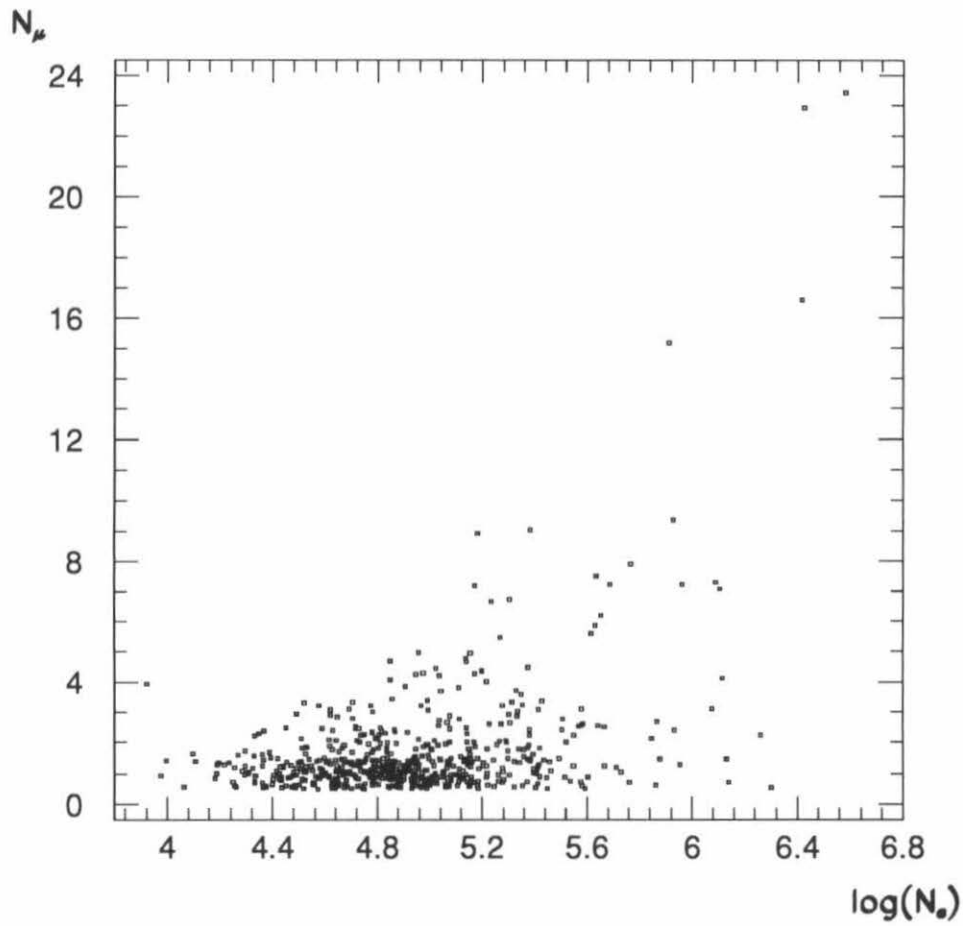

Figure 4.32: Muon multiplicity in MACRO versus shower size at EAS-TOP for the 580 HEI coincidences. The linear correlation coefficient for the distribution is r = 0.44. A value of r this large or larger has a probability 7×10^{-26} of occurring if the distributions of N_μ and $\log(N_e)$ are uncorrelated.

The angular anticoincidence window is defined as:

$$\begin{cases} 208^\circ < \phi_M + \theta_M < 230^\circ \\ 33^\circ < \phi_M - 4.6 \times \theta_M < 46^\circ \end{cases} \tag{4.4}$$

The solid angle it subtends at MACRO is $\Omega = 0.0083$ sr. The intersection of this solid angle window with a horizontal plane at the level of EAS-TOP is shown in Fig. 4.33, superimposed onto a map of the EAS-TOP counters projected onto the same horizontal plane along the line of sight to MACRO. Muons reconstructed by MACRO to point within the anticoincidence window defined by Eq. 4.4 may actually have scattered into it from outside of this window. In Fig. 4.33 is also shown a larger region of actual ground impact for more than 97% of the events reconstructed to point to the inner region. It subtends a 0.019 sr solid angle, and is determined by a Monte Carlo calculation, in which a muon entering the ground at angles (θ, ϕ) is allowed to scatter by an overall angle χ and uniformly in azimuth about its initial direction, where χ is selected according to the experimental distribution of angular separations between muons of dimuon pairs (see Fig. 2.13; this distribution includes all underground propagation as well as detector effects). This is a conservative calculation, as the mean dimuon separation is 0.74°, whereas the reconstructed muon angular deviation from shower axis is about 0.5° in the mean. Thus, the great majority of MACRO events satisfying Eq. 4.4 entered the ground well within the area of EAS-TOP sensitivity.

During the 96.3 days of combined live time, a total of 2913 events were recorded by MACRO to point to within the anticoincidence window defined by Eq. 4.4, for an anticoincidence rate of (30.2 ± 0.6) events/day. Out of the 7644 time-coincident events of Section 4.1.2, 673 were reconstructed by MACRO to point within the anticoincidence window (these events include EAS-TOP triggers of all types, not only HEI). The coincidence rate within this angular window was thus (7.0 ± 0.3) events/day. The anticoincidence-to-coincidence ratio was about 4.4 : 1.

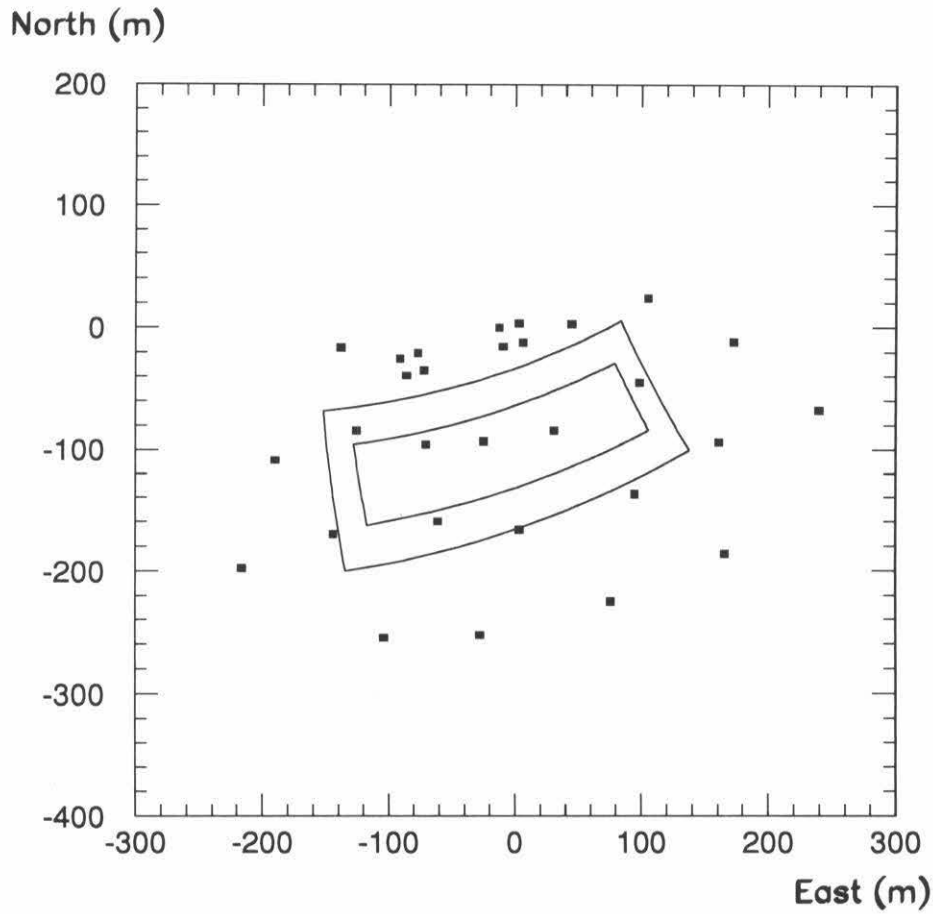

Figure 4.33: Anticoincidence window definition: intersection of the anticoincidence solid angle (Eq. 4.4) with a horizontal plane at the level of EAS-TOP (inner region) superimposed onto a map of the EAS-TOP counters projected onto the same plane along the line of sight to MACRO. More than 97% of the muons reconstructed to point to the inner region actually entered the ground within the outer region (see text).

N_μ	Coincidences	Anticoincidences
1	567	2849
2	78	61
3	18	3
4	4	
5	3	
6	1	
7	1	
8	1	
total:	673 ± 30	2913 ± 50
$\overline{N}_\mu$:	1.23 ± 0.03	1.023 ± 0.003

Table 4.5: Number of events of each muon multiplicity recorded by MACRO in coincidence and anticoincidence with EAS-TOP. The uncertainty on the number of events of each multiplicity is the square root of that number.

4.4.2 Muon multiplicities

All 673 coincident events within the anticoincidence window were scanned visually to verify the multiplicities assigned by the DREAM reconstruction program. All anticoincident events with reconstructed multiplicities greater than one were also scanned, 64 in all. A sample of 100 anticoincident events of multiplicity one was scanned, and all events were found to be indeed single muons; thus no correction was applied to the number of single muon, anticoincident events. Table 4.5 gives the number of events of each multiplicity recorded for coincident and anticoincident events satisfying Eq. 4.4, and Fig. 4.34 displays the same information graphically, but with the distributions normalized to the number of single muons in each case. The mean multiplicities are $\overline{N}_\mu = (1.23 \pm 0.03)$ for coincidences and $\overline{N}_\mu = (1.023 \pm 0.003)$ for anticoincidences. The larger mean multiplicity for coincident events is due to a trigger configuration corresponding to a higher primary energy.

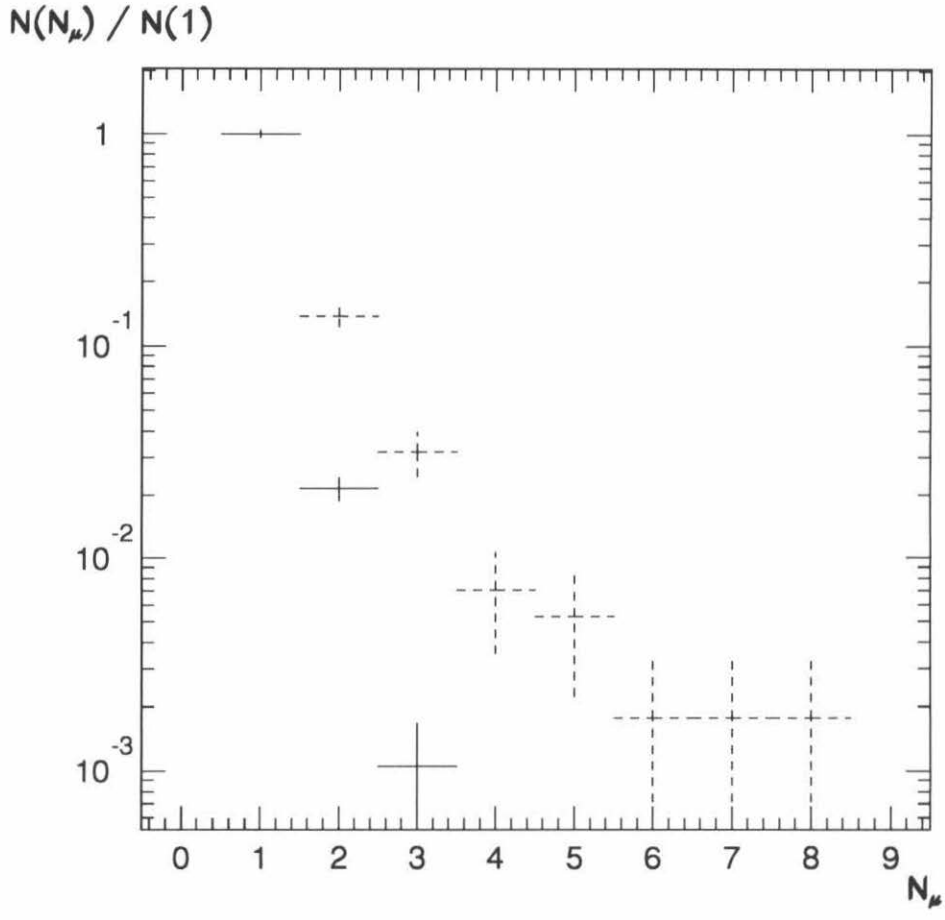

Figure 4.34: Muon multiplicity distributions for coincidences (dashed lines) and anticoincidences (solid lines). Each distribution is normalized to the number of single muons. The mean multiplicities are (1.23 $\pm$ 0.03) and (1.023 $\pm$ 0.003), respectively.

4.5 Summary and conclusions

The method of finding coincident events between MACRO and EAS-TOP from the individual data sets on the basis of atomic clock times works well and yields sets of events with very little contamination by accidental coincidences. Moreover, in the particular case of the high-energy internal events, for which EAS-TOP reconstructions have the greatest resolution, a systematic comparison of the independent reconstructions by MACRO and EAS-TOP of the shower direction and point of impact on the ground surface yields good agreement between the two and permits the unambiguous identification of chance coincidences. For events with core location outside of the array, a precise determination of the core location is difficult (large counts in the stations could result from a distant high-energy or a near low-energy shower), and in principle a core location supplied by MACRO can be used to perform the NKG reconstruction of the shower size. Although some work has been performed in that direction, this remains mostly in the realm of future improvements to the coincidence work.

The experimental muon multiplicity distributions satisfy the expectations that an increase in mean primary energy results in an increase in mean muon multiplicity underground, as shown by comparing the distribution of multiplicities recorded by MACRO alone with those in coincidence with EAS-TOP events of two different trigger configurations. Similarly, the mean shower size reconstructed by EAS-TOP, for high-energy internal events in coincidence with MACRO, increases when a high muon multiplicity cut is applied.

Finally, the mean muon multiplicity observed underground for events in coincidence with EAS-TOP is larger than that for events in anticoincidence, as expected for the two different ranges of primary energies sampled by the two sets of events.

Chapter 5

Monte Carlo Simulations

In this chapter, we present and describe the chain of computer programs (all written in FORTRAN) used in Monte Carlo simulations of MACRO/EAS-TOP events, in coincidence or anticoincidence. Then we present some distributions obtained with it, of relevance to primary composition studies.

5.1 Simulation chain

A flowchart of the Monte Carlo simulation chain used in the analysis of coincident data is shown in Fig. 5.1. An event generator called HEMAS selects a primary cosmic ray direction and energy (with the primary mass input as a parameter), causes this primary cosmic ray to interact in the atmosphere, propagates the interaction products and causes them to further interact or decay. From the atmospheric cascade, an electromagnetic shower size at the ground level is calculated. Muons produced in the decay of high-energy pions and kaons are further propagated through the ground, and events for which at least one muon survives to the depth of MACRO are saved for further processing. Next, a program called HEMCAMP samples the axis of the shower over an area underground larger than the effective area of MACRO,

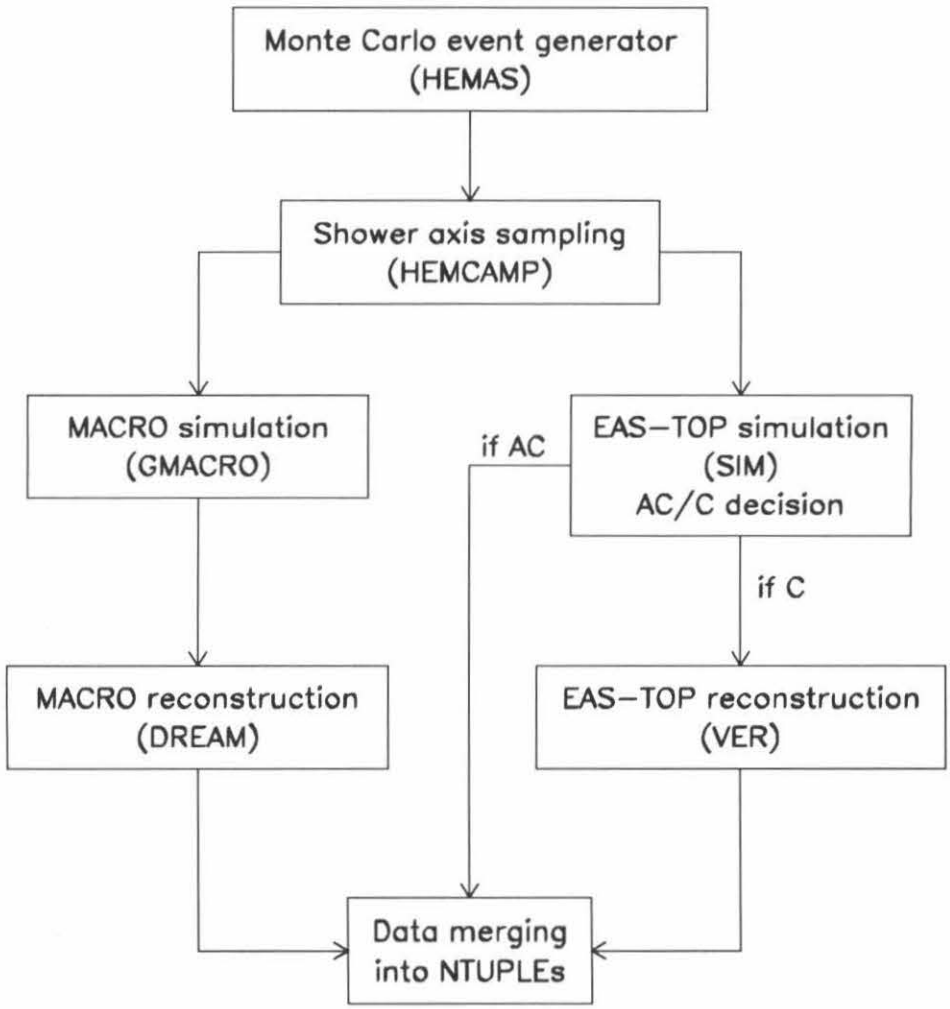

Figure 5.1: Flowchart of the Monte Carlo simulation chain. The names of various programs used are shown in parentheses. AC and C refer to AntiCoincident and Coincident event, respectively.

and records the events for which at least one muon hits a simplified simulated underground detector. Then the simulation splits in two arms for the underground and surface reconstructions, respectively. First, a program called GMACRO fully simulates the experimental details of the MACRO apparatus, and for those events determined to have hit the detector, creates a file of the same format as that used in recording the experimental data. This file is subsequently input to the same MACRO reconstruction program (called DREAM) used for experimental data. In parallel, a program called SIM simulates the EAS-TOP array and superimposes the virtual electromagnetic air shower onto it, for the events output by HEMCAMP. At this point in the chain, a decision is made as to whether the event has triggered the surface detector or not, and therefore whether the event is coincident or anti-coincident. Those events that do trigger the array are reconstructed by VER, also used to reconstruct experimental EAS-TOP events. One last program merges the reconstructed events back together and saves the results to NTUPLE files, which are subsequently studied using the PAW package from CERN (see Reference [74]).

In the next few subsections, the various programs in the simulation chain are described in some detail.

5.1.1 The HEMAS event generator

The HEMAS (**H**adronic, **E**lectromagnetic and **M**uonic components of **A**ir **S**howers) generator is fully described in Reference [75]. Here we review briefly its underlying physical assumptions and some of its operational details.

Sampling of primary mass, direction and energy

A separate Monte Carlo run is made for each primary mass group, where masses 1, 4, 14, 24 and 56 are used (see Section 1.2.2), and primary mass is input to the HEMAS generator (for some calculations, a mass of 27 is used for the Mg group).

The energy of the primary is sampled from a differential energy spectrum appropriate for the mass group being studied, such as the directly measured spectra of Fig. 1.3 (or any composition model tested against the data, extending beyond the knee). The minimum energy sampled is determined from the threshold energy for a primary to yield an underground muon (from 2×10^3 GeV for a proton primary to 8.4×10^4 GeV for an iron primary). In practice, for anticoincidence simulations, a slightly higher bound (4.1×10^3 GeV for protons, the 95% mark, see Fig. 5.4) is used to reduce the number of events run to manageable levels, the high-energy muon yield being low near threshold, and the spectra being steep enough that even a small increase in lower limit yields a large saving in number of events simulated; for coincidence simulations, a low-energy bound of 5×10^4 GeV is used, well below the threshold of EAS-TOP for HEI events. An upper limit to the energy range sampled is any energy never attained during the live time simulated. For coincidence simulations, the upper limit used is 10^8 GeV, whereas for anticoincidence simulations an upper limit of 9×10^5 GeV is sufficient, where EAS-TOP has long since reached full trigger efficiency and all events are coincident (see Fig. 5.3).

Cosmic rays at the top of the atmosphere being isotropic, the azimuth angle of each primary is sampled uniformly, and the zenith is sampled according to a $\cos\theta \sin\theta$ distribution, where the extra $\cos\theta$ factor arises in projecting the primary flux onto a horizontal surface (that of the horizontal plane underground containing MACRO). For coincidence simulations, zenith and azimuth are sampled in angular ranges $18° \leq \theta \leq 44°$ and $146° \leq \phi \leq 224°$, respectively, corresponding to a solid angle window about twice as large as the one subtended at MACRO by the effective area of EAS-TOP. For anticoincident events, defined by the geometrical requirement of Eq. 4.4, the angular sampling bounds used are those corresponding to the outer region drawn in Fig. 4.33, containing at least 97% of all events.

Shower size and muon multiplicity generation

After HEMAS has selected a primary energy and angular direction according to the above prescription, an air shower is developed following the flowchart of Fig. 5.2. On it, the index I is the number of particles remaining to be processed in the shower, and it fluctuates up and down as the shower is followed. The significance of other symbols in the figure is as follows: I' is the number of particles remaining to be processed before each iteration of the shower loop, Ne is the total electromagnetic shower size at the ground surface, Ne' is a subsize resulting from the current particle in the loop, Nμ is the muon multiplicity deep underground, Hi is the height above sea level of production of particle i in the atmosphere, Hi' is its height of disappearance due to interaction or decay, Hdecay is the height at which the particle decays (if it can), Hgnd is the atmospheric height of the ground surface and N is the number of new particles produced in an interaction or decay.

In the cascade development, electrons, positrons and gammas as well as particles with energy less than 10^3 GeV are not followed. Rather, for electrons, positrons and gammas, a subroutine (ANEM) is called to calculate the electromagnetic shower size at the ground surface that results from them, and the result is added to the total shower size. A similar routine (ANHAD) is used to calculate the contribution from hadrons of energy less than 10^3 GeV. Both ANEM and ANHAD utilize tables of shower sizes constructed from independent simulations using the full electromagnetic and hadronic treatment of the EGS4 and CERN's GEANT software packages, accounting for all possible detector effects such as conversion of low-energy gammas into $e^{\pm}$ pairs in the EAS-TOP scintillator.

Before reaching the ground, hadrons and muons with energy greater than 10^3 GeV face the possibility of decaying or interacting (for muons, decaying only, and for nucleons, interacting only), whichever comes first (higher up in the atmosphere), if at all. Muons deemed not to decay in the atmosphere are subsequently propagated

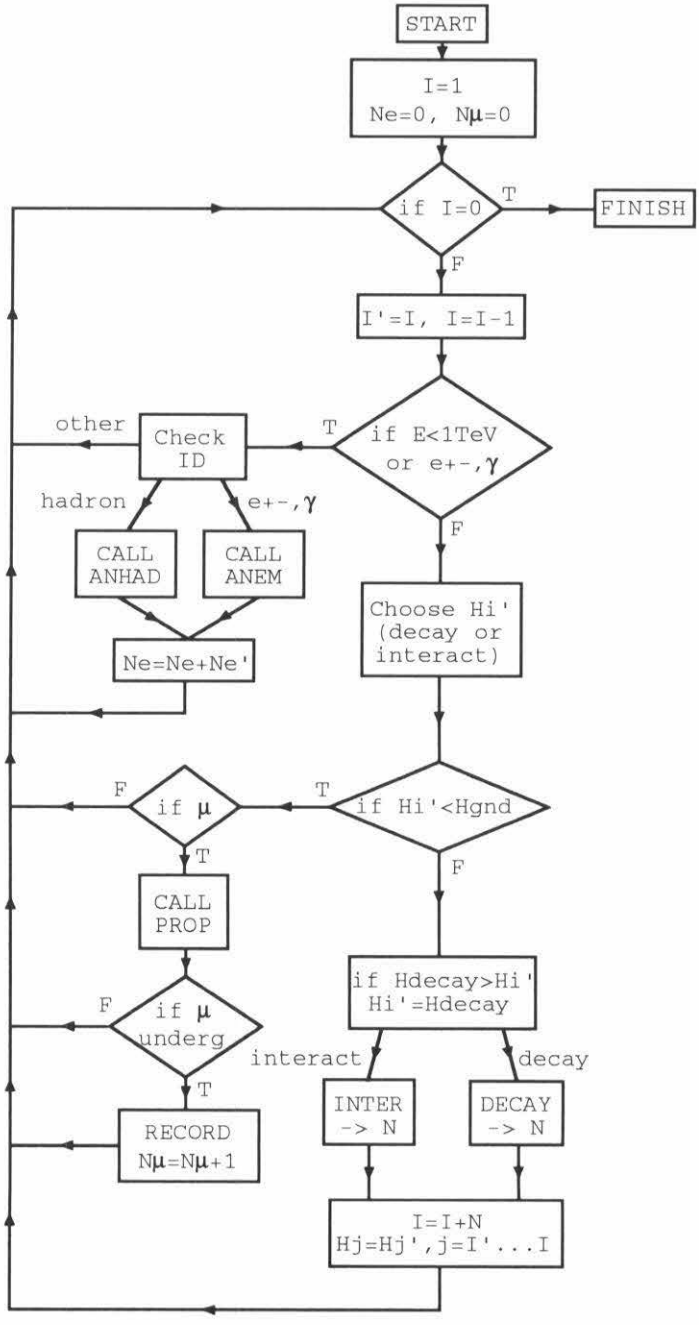

Figure 5.2: Flowchart of the HEMAS event generator. See text for a detailed explanation.

through the ground (subroutine PROP), and are recorded if they reach the depth of MACRO. Muon energy loss is parametrized from a full simulation including ionization, pair production, bremsstrahlung and nuclear interactions, and is used to calculate angular deflections and lateral displacements in each step. Results were found to agree with Scott-Snyder-Molière theory. The propagation routine (see Reference [76]) divides the ground into steps of 25 hg/cm^2-thickness each, within which average energy losses (on the order of a few GeV) are negligible compared with the total muon energy. The step size is further reduced when energy losses result in angular deflections greater than one degree. The propagation routine also makes use of a full map of the Gran Sasso mountain (obtained from a survey performed by the Italian Istituto Geografico Militare).

Hadronic interaction generator

Again, the hadronic interaction generator of HEMAS is described extensively in Reference [75]. The algorithm for pp and $p\bar{p}$ interactions is based initially on the GENCL code developed by CERN's UA5 collaboration (see Reference [77]), which has been checked against pp data at $\sqrt{s} = 53$ GeV and $p\bar{p}$ data from $\sqrt{s} = 53$ GeV to 900 GeV, where s is the square of the center-of-mass energy. It describes particle production in terms of clusters and imposes energy and momentum conservation. Several parameters of the clustering mechanisms are taken directly from experimental observations, and *ad hoc* assumptions are made to fit various distributions (such as pseudorapidity, transverse momentum and charged multiplicity) to experimental data. Nucleon-nucleus interactions are obtained from nucleon-nucleon results by application of Glauber theory, as in Reference [78], with some experimental input from p-nucleus experiments. Extrapolation of cross-sections to energies not yet reached at accelerators is done according to the prescription $\sigma \sim a + b[\ln(s)]^{1.8}$ (as in Reference [79]). Pion-nucleus and kaon-nucleus interactions are treated in a fashion similar

to the nucleon-nucleus case, with appropriate modifications tuned to experimental π^+-C and K^+-C data. The initial nucleus-nucleus interaction is treated in the context of the superposition approximation, where a primary of total energy E and mass A is treated as A nucleons, each of energy E/A, and each independently interacting in the atmosphere.

Parametrizations of underground muon characteristics obtained with HEMAS were used as the basis of Monte Carlo calculations of the decoherence function of underground muons (*i.e.*, the distribution of separation between muons in bundles), in comparison with MACRO data (see Reference [59]). Good agreement was obtained and taken as evidence for the validity of the entire algorithm. In Reference [28], the NUSEX collaboration reports also using parametrizations obtained with HEMAS to calculate muon multiplicity distributions, and finding good agreement with the experimental distribution.

5.1.2 The rest of the simulation chain

In HEMCAMP (see Fig. 5.1), for events generated by HEMAS with at least one deep-underground muon, sampling of the shower core is done by dropping the shower axis uniformly over an underground area 104 m $\times$ 92 m ($\sim$30 times the effective horizontal area of MACRO), and testing whether any muon hits a simplified version of the detector. This area is large enough to permit absolute flux calculations without significant bias (*e.g.*, for 9×10^5 GeV Fe primaries, the probability for a shower with axis outside this area to yield a muon in MACRO is less than 0.6%). To partially compensate for the high event rejection rate incurred by this technique, events from a primary of energy less than 2×10^5 GeV are sampled four times each, those from primaries of energy between 2×10^5 and 10^6 GeV are sampled twice, and those from higher-energy primaries are sampled only once. In the first case, 4.9% of accepted events are detected twice and 57% of all generated events are accepted; in the second

case, 1.9% of accepted events are detected twice and 22% of all generated events are accepted; in the last case 8.0% of all generated events are accepted. Events from higher-energy primaries are sampled a smaller number of times than those from low-energy primaries so as to avoid biases in possibly over-sampling large multiplicity events that have a higher probability of being accepted more than once.

The GMACRO program is a simulation of the MACRO detector based on the GEANT package from CERN (see Reference [80]). The various components of the detector are simulated, including the electronics (in particular the streamer tube readout scheme). As muons travel through the detector, all physical processes available in the program are allowed (such as multiple scattering, bremsstrahlung and pair creation). It is determined whether the event from HEMCAMP triggers the detector, and the data is written to a file of the same format as that used for experimental data. The events are then subjected to the DREAM reconstruction procedure described in Section 2.3.2.

Program SIM takes the events determined by HEMCAMP to have hit MACRO and extrapolates the shower axis back to the surface to determine where the location of the shower core is with respect to the EAS-TOP array. The experimental angular resolution is simulated by adding to the simulated direction an angular shift, sampled from an experimental resolution curve, and corrected to account for systematic effects due to shower front curvature. The mean number of particles having hit each scintillator counter of the array is obtained by superimposing the NKG lateral distribution function (Eq. 3.1) onto the array, using the simulated N_e as its normalization (the age parameter s is sampled from the experimental distribution). A new average number of particles for each counter is calculated by sampling from a Poisson distribution with this mean. Finally, the effective actual number of particles recorded by each counter is sampled from a Gaussian distribution with this new mean, and a sigma taken from the experimental distribution. It is then decided whether the event

has satisfied the trigger requirement of Section 3.2.1 or not, and therefore whether the event is coincident or anticoincident. The event is subsequently reconstructed by VER, the same program used in reconstructing experimental events (see Section 3.3).

The final step of the analysis chain is one more program which merges the outputs of DREAM and VER into a PAW-readable file, storing the parameters of the events into NTUPLEs.

5.2 Some simulated distributions

In Section 2.4, in a discussion of angular resolution issues for MACRO, a distribution of calculated angular deviations from shower axis of deep-underground muons was presented (Fig. 2.12). It had been obtained using the Monte Carlo code described in the previous Section. In this Section, we present a few more distributions, obtained with the simulation chain, of relevance to MACRO/EAS-TOP studies.

5.2.1 Primary energy for coincident and anticoincident events

Fig. 5.3 shows the number of MACRO events, coincident or anticoincident with EAS-TOP, per million showers, as a function of primary energy. The calculations were made for proton primaries from a fixed direction $\theta = 33.1°$ and $\phi = 186.9°$, near the center of the fiducial window defining anticoincident events (Eq. 4.4). It shows that the minimum primary energy required to yield a muon capable of reaching MACRO is about 2×10^3 GeV, that the minimum primary energy required for an electromagnetic air shower to trigger EAS-TOP is about 10^4 GeV, that the maximum probability for a proton primary to yield an anticoincident event is at about 6×10^4 GeV, and that at energies greater than about 4×10^5 GeV all events are coincident, *i.e.*, EAS-TOP has achieved full trigger efficiency.

The contribution of primaries of various energies to underground rates arises from

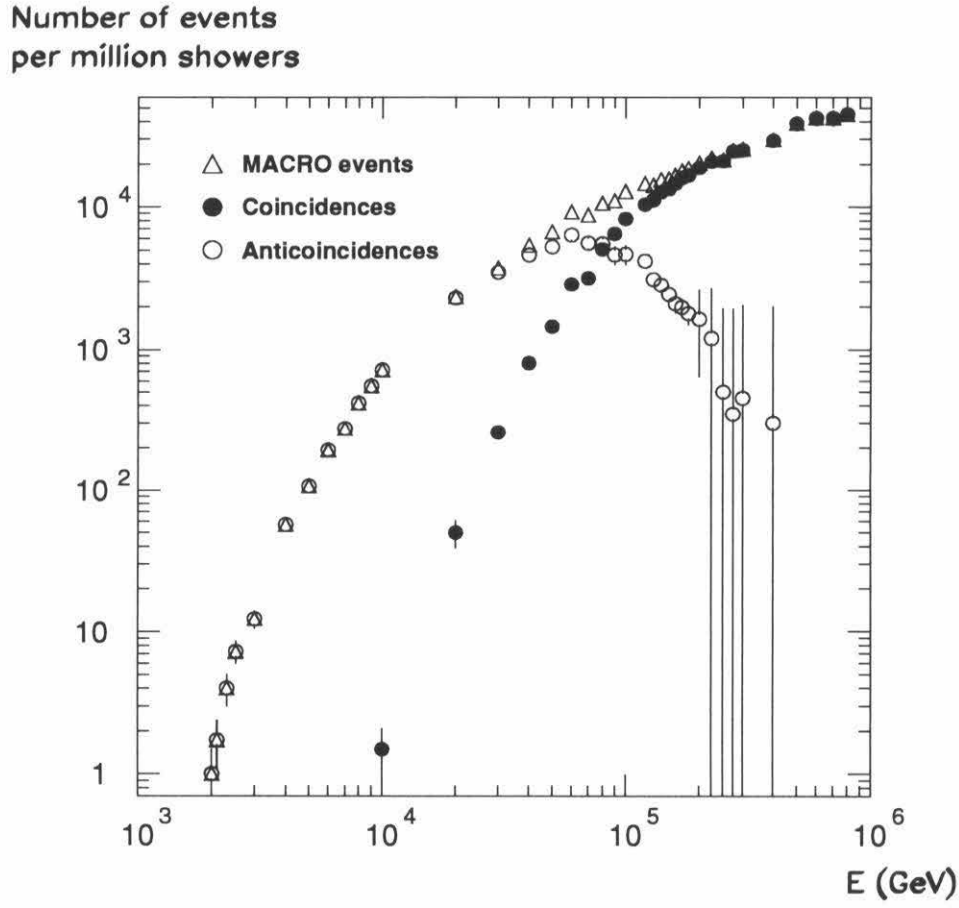

Figure 5.3: Simulated number of events in MACRO, coincident or anticoincident with EAS-TOP, per million showers, as a function of primary energy E (in GeV). The simulation was run for proton primaries from a fixed direction $\theta = 33.1°$ and $\phi = 186.9°$, with an underground sampling area about 30 times the effective horizontal area of MACRO. Error bars are the statistical uncertainties.

the previous distribution multiplied by the primary flux, which falls with energy as a power law (see Section 1.1). Fig. 5.4 shows the result of multiplying the distribution of Fig. 5.3 (with the ordinate values divided by 10^6) by a differential all-particle flux 1.90×10^4 $E^{-2.64}$ $m^{-2}s^{-1}sr^{-1}GeV^{-1}$ (the power-law fit shown on the all-particle spectrum part of Fig. 1.3) and by the underground sampling area A = 9568 m^2. The same data is presented differently in Fig. 5.5, with the ordinate values of Fig. 5.4 multiplied by the primary energy E (in GeV), noting that $EdN/dE = dN/d(lnE)$, and therefore that the area under the distributions of Fig. 5.5 is proportional to their integral. This shows that most anticoincident events (and indeed most MACRO events) arise from the region between 5000 GeV and 50000 GeV, whereas most coincident events arise from a decade more in energy.

5.2.2 Pair separation in dimuon events

Fig. 5.6 shows the distribution of separations R_2 between the two muons of anticoincident dimuon events, for experimental data and for two simulated compositions (the light and tailored models described in Section 6.1). The curves are fits to the simulated distributions, where the functional form used is $aR_2 \exp(-R_2/b)$, and where the normalization is arbitrary. Within the obviously limited experimental statistics, the shape of the simulated distributions is correct. The mean separations are: for experimental data (5.54 ± 0.40) m, for the light composition model (5.70 ± 0.13) m and for the tailored composition model (5.78 ± 0.14) m.

Fig. 5.7 shows the equivalent distributions for coincident events this time. Again, the shape of the simulated distributions is in agreement with experimental data. The mean separations are: for experimental data (5.83 ± 0.50) m, for the light composition model (5.11 ± 0.12) m and for the tailored composition model (5.45 ± 0.11) m.

No composition statement can be drawn from either distribution due to the obviously limited statistics of dimuon events.

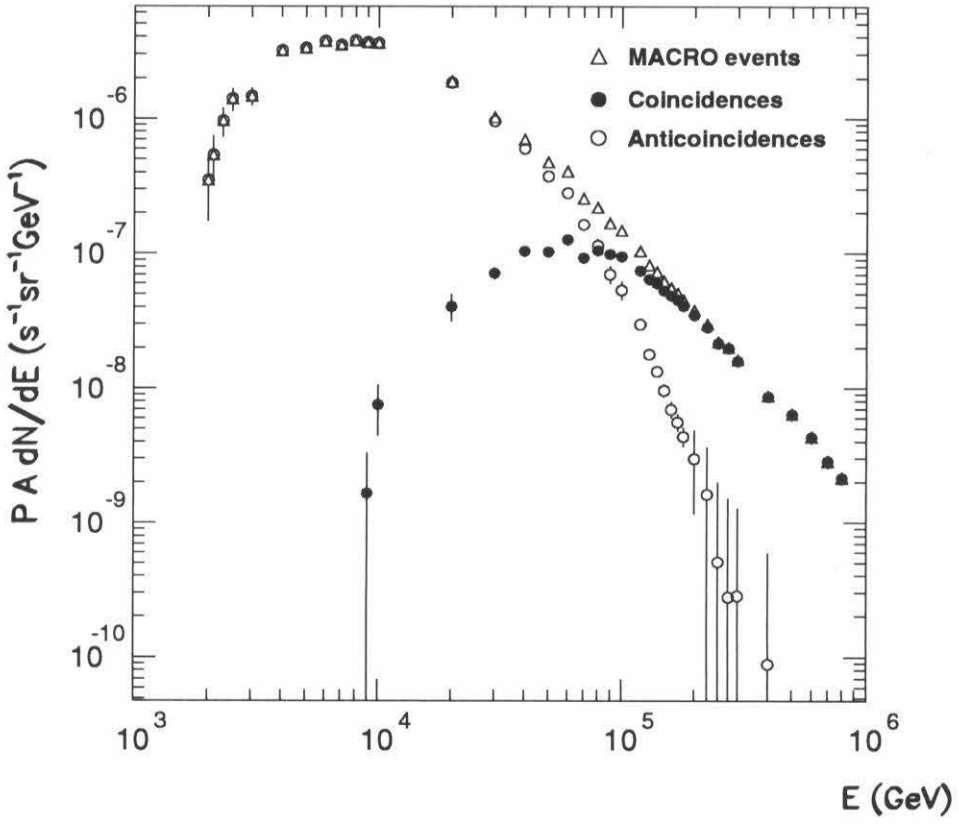

Figure 5.4: Event probability P from Fig. 5.3 multiplied by the all-particle differential flux $dN/dE = 1.90 \times 10^4\ E^{-2.64}\ m^{-2}s^{-1}sr^{-1}GeV^{-1}$ and by the underground sampling area $A = 9568\ m^2$, as a function of primary energy E (in GeV). Error bars are statistical uncertainties.

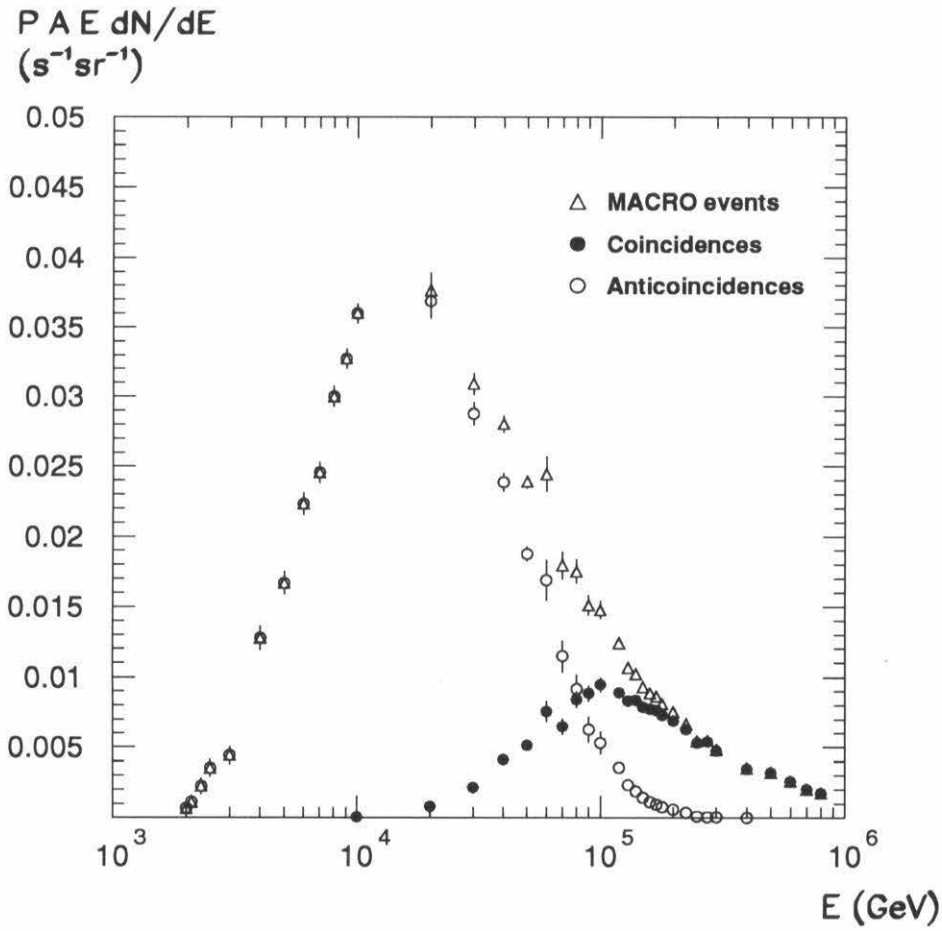

Figure 5.5: Event probability P multiplied by the underground area A, the all-particle differential flux dN/dE (as in Fig. 5.4) and by the primary energy E. Note that EdN/dE = dN/d(lnE), so that the area under the distributions is proportional to their integral.

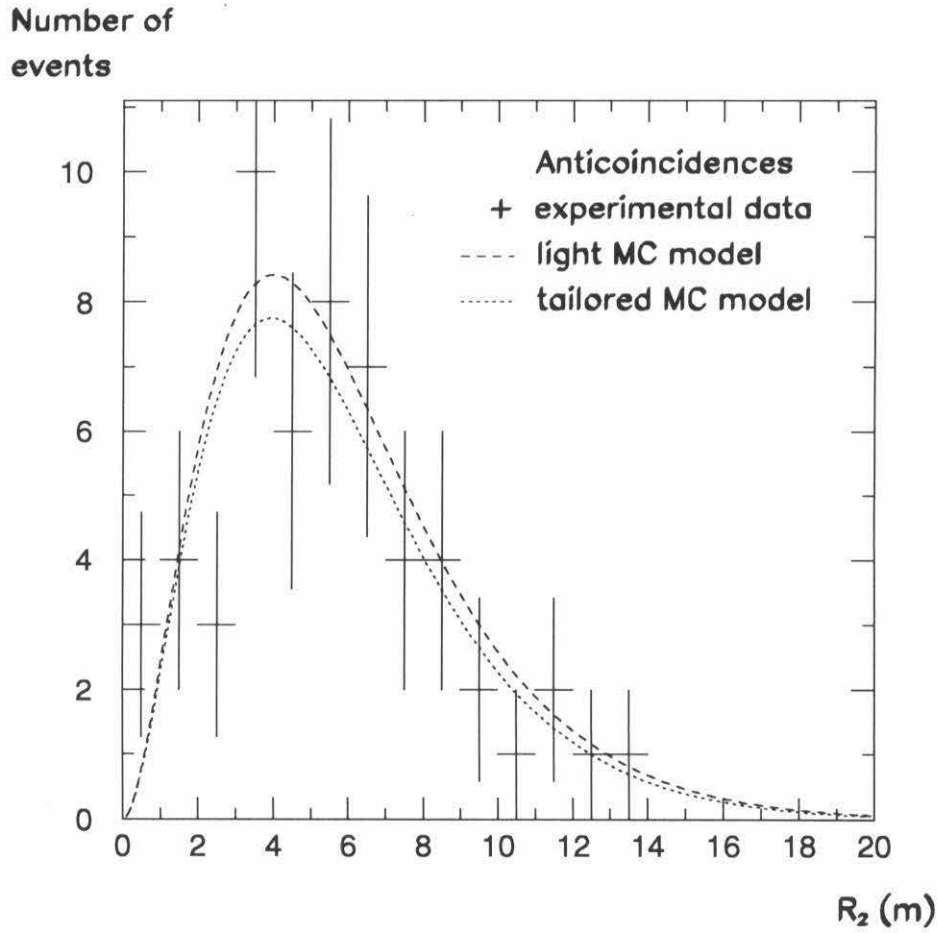

Figure 5.6: Muon pair separation R_2 (in m) between the two tracks of anticoincident dimuon events, for experimental data and two simulated compositions (the models are described in Section 6.1). The Monte Carlo normalizations are arbitrary. The mean separations are: experimental: (5.54 ± 0.40) m, light model: (5.70 ± 0.13) m, tailored model: (5.78 ± 0.14) m.

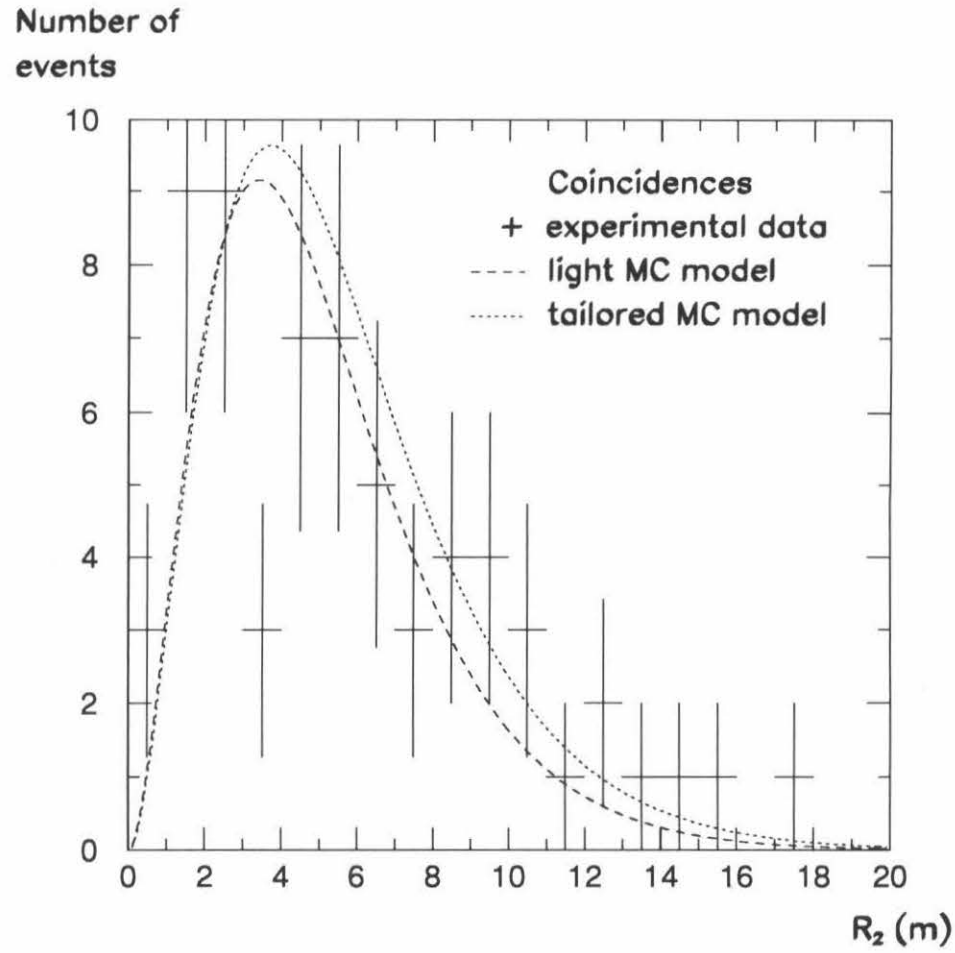

Figure 5.7: Muon pair separation R_2 (in m) between the two tracks of coincident dimuon events, for experimental data and two simulated compositions (the models are described in Section 6.1). The Monte Carlo normalizations are arbitrary. The mean separations are: experimental: (5.83 ± 0.50) m, light model: (5.11 ± 0.12) m, tailored model: (5.45 ± 0.11) m.

5.2.3 Atmospheric muon spectrum

Fig. 5.8 shows the differential energy spectrum for near-vertical atmospheric muons at sea level, for assumed effective area 43 m^2, live time 100 days and solid angle 0.095 sr. Three sets of calculations are shown: those obtained with the HEMAS-based Monte Carlo chain (using the tailored model of Section 6.1 as the primary composition), those obtained with the MACRO-reconstructed atmospheric muon spectrum of Reference [57] (valid for muon energies greater than about 1 TeV):

$$\frac{dN_\mu}{dE_\mu} = (1.3 \pm 0.2) \times 10^{-3} \frac{E_\mu{}^{(-3.56 \pm 0.03)}}{\cos\theta} \quad m^{-2}s^{-1}sr^{-1}TeV^{-1} \tag{5.1}$$

and those obtained with the calculation of Reference [13], p. 71 (verified for muon energies less than about 0.8 TeV):

$$\frac{dN_\mu}{dE_\mu} \approx 1.1 \times 10^{-2} E_\mu{}^{-2.7} \left(\frac{1}{1 + 9.6\, E_\mu \cos\theta} + \frac{0.054}{1 + 1.3\, E_\mu \cos\theta} \right) m^{-2}s^{-1}sr^{-1}TeV^{-1} \tag{5.2}$$

The atmospheric spectrum of Reference [57] was obtained by first measuring the muon flux underground in MACRO as a function of rock depth, and deconvoluting the result from the muon survival probability. Therefore the spectrum obtained corresponds to atmospheric muons of energies greater than 1 TeV and is directly comparable with the spectrum of TeV muons calculated using the simulation chain described in Section 5.1. On the other hand, the atmospheric spectrum calculated in Reference [13] is found to be in agreement with measurements below 1 TeV, and is being extrapolated here. However, Fig. 5.8 shows that it is in good agreement with the MACRO result.

The index of the atmospheric muon energy spectrum resulting from the HEMAS generator is in agreement with that of the two independent results shown in Fig. 5.8, but the normalization is lower by about 25–30%. The effect is not understood at this time and is under investigation. It is not due to the use of the tailored model of Section 6.1, as the all-nucleon spectrum for the tailored model is in good agreement with

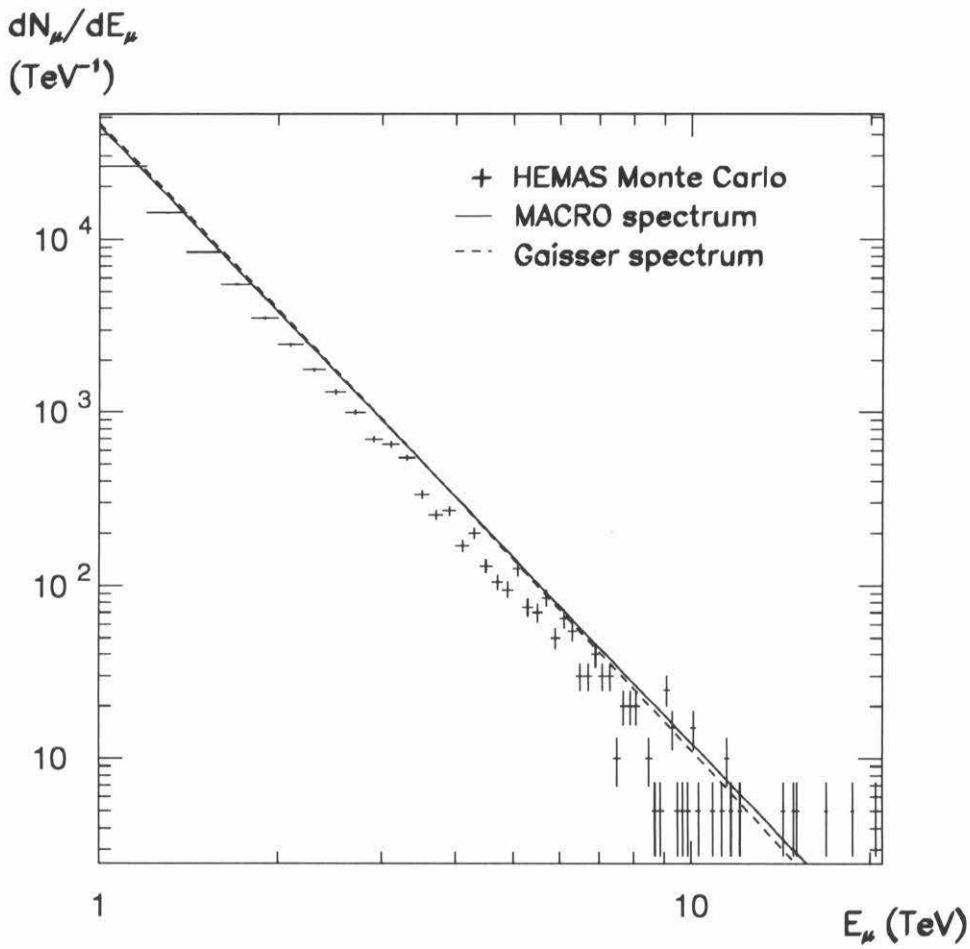

Figure 5.8: Atmospheric muon energy spectrum, with muon energy in TeV, at sea level, for near-vertical muons ($0° \leq \theta \leq 10°$). Shown are results from the HEMAS Monte Carlo and from two independent calculations (see text), for assumed effective area 43 m^2, live time 100 days and solid angle 0.095 sr.

that used in the calculation of Reference [13] ($0.14\ E^{-2.7}$ nucleons/(m^2 s sr TeV/A)). Indeed, a simulation of atmospheric muons resulting from an all-proton primary flux following the all-nucleon spectrum of Reference [13] still shows a 20% deficit.

Chapter 6

Comparison of Experimental and Monte Carlo Data

In this chapter, we first describe the various primary composition models that are used as input to the Monte Carlo simulation chain of the previous chapter. Then we compare the rate and muon multiplicity distribution obtained with these models with the equivalent experimental quantities, for events pointing to a small fiducial area well within the boundaries of EAS-TOP. Finally we compare the rates, muon multiplicity and shower size distributions obtained with these models for high-energy, internal coincidence simulations with the equivalent experimental quantities, and draw some conclusions on primary composition. Some of the results presented here will appear in Reference [2].

6.1 Primary composition models used

Various primary compositions have been used as input to the Monte Carlo simulation chain described in Section 5.1, to compare muon multiplicity and shower size distributions with the experimental quantities in an effort to discriminate be-

tween the various models. The parameters K and γ of the models used are listed in Table 6.1, where the differential energy spectrum of each mass group is given by $dN/dE = KE^{-\gamma}$, with possible changes in the index γ at various energies E_{cut} (given in GeV). In the following, we describe the models used, giving some justification for each.

6.1.1 Pure primary compositions

A natural first assumption that can be made to study the behavior of the simulation chain and interaction model is that the primary flux constitutes entirely of a single component of mass A, *e.g.*, pure protons, He nuclei or Fe nuclei. This is known to be a poor assumption at energies below 10^6 GeV (see Fig. 1.3), but at higher energies, and particularly near and above the knee, the composition is unknown; besides, certain theoretical scenarios predict that the cosmic flux becomes entirely made up of protons, whereas others predict an increasingly heavy composition (see Section 1.4). This approach is also useful in studying the primary composition in terms of average mass. Three pure compositions have been simulated, namely all-p, all-He and all-Fe compositions.

The differential spectra utilized in sampling the energy of each p, He or Fe primary are shown in Fig. 6.1, together with the same experimental data as in Fig. 1.1. Each spectrum was constructed by first running the simulation chain at a number of fixed energies for the mass group, calculating the electromagnetic shower size resulting at each energy setting, and then constraining the primary energy spectrum to yield the experimentally observed EAS-TOP standalone shower size distribution. At a given total primary energy, a heavy primary interacts sooner (higher up) in the atmosphere than a light primary, and the resulting shower size at any given depth past shower maximum is therefore smaller. In other words, in order for a heavy primary to yield a certain shower size, it requires a higher total energy than a light one. This is why

Model	K	γ	E_{cut}	$\gamma(E>E_{cut})$
All-p	1.53×10^5	2.88	1.7×10^6	3.19
All-He	4.94×10^5	2.92	2.2×10^6	3.24
All-Fe	3.23×10^6	2.99	3.5×10^6	3.32
Light				
p	1.50×10^4	2.71	2.0×10^4	
	1.87×10^3	2.50	3.0×10^6	3.00
He	5.69×10^3	2.71	3.0×10^6	3.00
CNO	3.30×10^3	2.71	3.0×10^6	3.00
NeMgSi	2.60×10^3	2.71	3.0×10^6	3.00
Fe	3.48×10^3	2.71	3.0×10^6	3.00
Heavy				
p	1.50×10^4	2.71	1.0×10^5	3.00
He	5.69×10^3	2.71	2.0×10^5	3.00
CNO	3.30×10^3	2.71	7.0×10^5	3.00
NeMgSi	2.60×10^3	2.71	1.2×10^6	3.00
Fe	3.10×10^2	2.36	2.7×10^6	3.00
Σ				
p	4.94×10^4	2.86		
He	3.31×10^4	2.80		
CNO	4.37×10^3	2.73	1.5×10^4	2.48
NeMgSi	2.62×10^3	2.72	1.0×10^4	2.55
Fe	1.08×10^3	2.59		
Tailored				
p	6.50×10^3	2.65		
He	1.43×10^4	2.72		
CNO	4.34×10^3	2.73	6.5×10^3	2.50
NeMgSi	2.62×10^3	2.72	6.0×10^3	2.50
Fe	1.08×10^3	2.59		

Table 6.1: Parameters of the various composition models used in the simulations (see text for a description). The spectrum of each component is given by $dN/dE = KE^{-\gamma}$, where K, in $m^{-2}s^{-1}sr^{-1}(GeV/nucleus)^{\gamma-1}$, is the normalization factor for $E < E_{cut}$. Cutoff energies E_{cut}, marking slope changes, are in GeV.

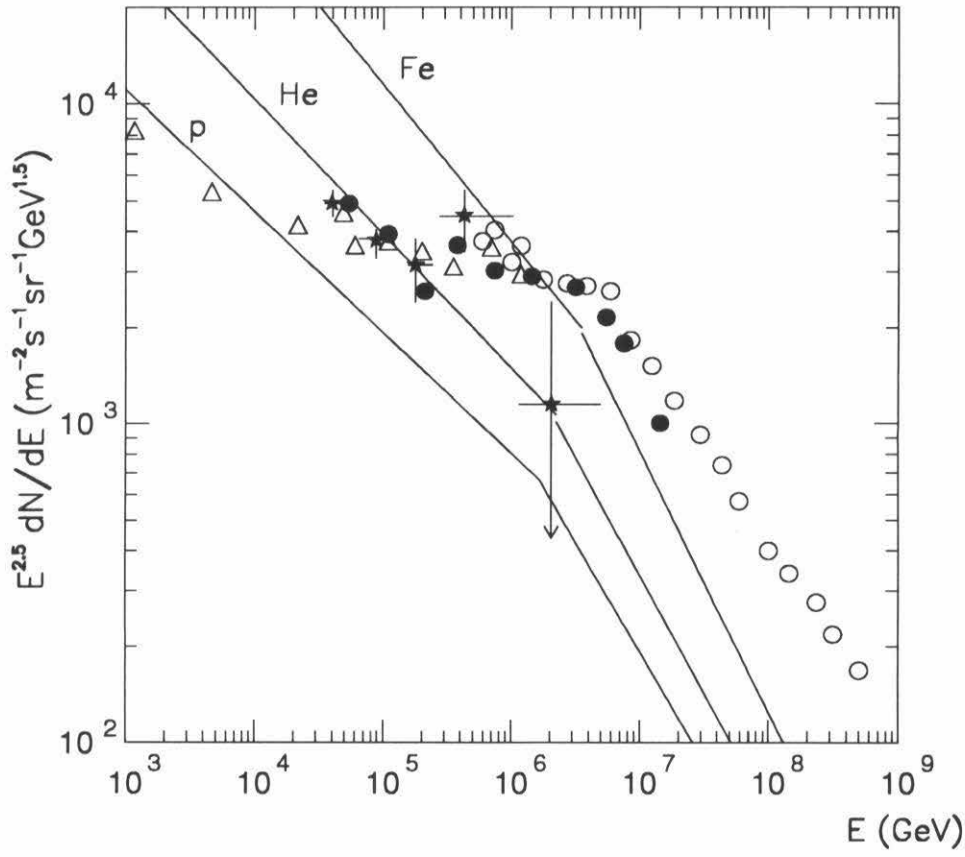

Figure 6.1: Primary spectra for all-p, all-He and all-Fe compositions adjusted to yield the observed EAS-TOP standalone shower size distribution, compared with the same experimental data as in Fig. 1.1. See Table 6.1.

the spectra constrained to yield a given shower size distribution are shifted towards higher energies for heavier primaries in Fig. 6.1. The fact that the spectra resulting from this construction method differ much from existing experimental data could be invoked as an argument against a pure composition in the first place. However, at energies greater than 10^6 GeV, the experimental spectrum data are derived from air shower results (where shower sizes are measured) by utilizing Monte Carlo techniques involving composition assumptions to start with, and large uncertainties are ever present. At any rate, as will be discussed in Section 6.3.3, the relation between muon multiplicity underground and simultaneous shower size at the surface is essentially independent of the primary spectrum utilized, and a composition statement can be made from it regardless of how poorly the spectrum used in the simulations agrees with the spectra determined by other experiments.

6.1.2 Light and heavy models

Two other primary composition models used in the analysis of MACRO/EAS-TOP data are the "light" and "heavy" models of Ref. [81], also used in the analysis of MACRO standalone data in Ref. [23]. The individual component spectra of the light and heavy models are plotted in comparison with direct measurements below 10^6 GeV on Figs. 6.2 and 6.3, respectively. The light model was constructed by adding a pure proton component to the other mass groups (fitted to direct measurements below a few thousand GeV) to constrain the sum to agree with the all-particle spectrum of Fig. 1.1. The heavy model is an extrapolation of the delayed-hadron results of Ref. [32]. The evolution with energy of the fractional composition for each of these two models is shown in Fig. 6.6. Neither of these models agrees with the JACEE He, CNO or NeMgSi data (the black circles on Figs. 6.2 and 6.3), and the heavy model has Fe abundances in disagreement with direct measurements.

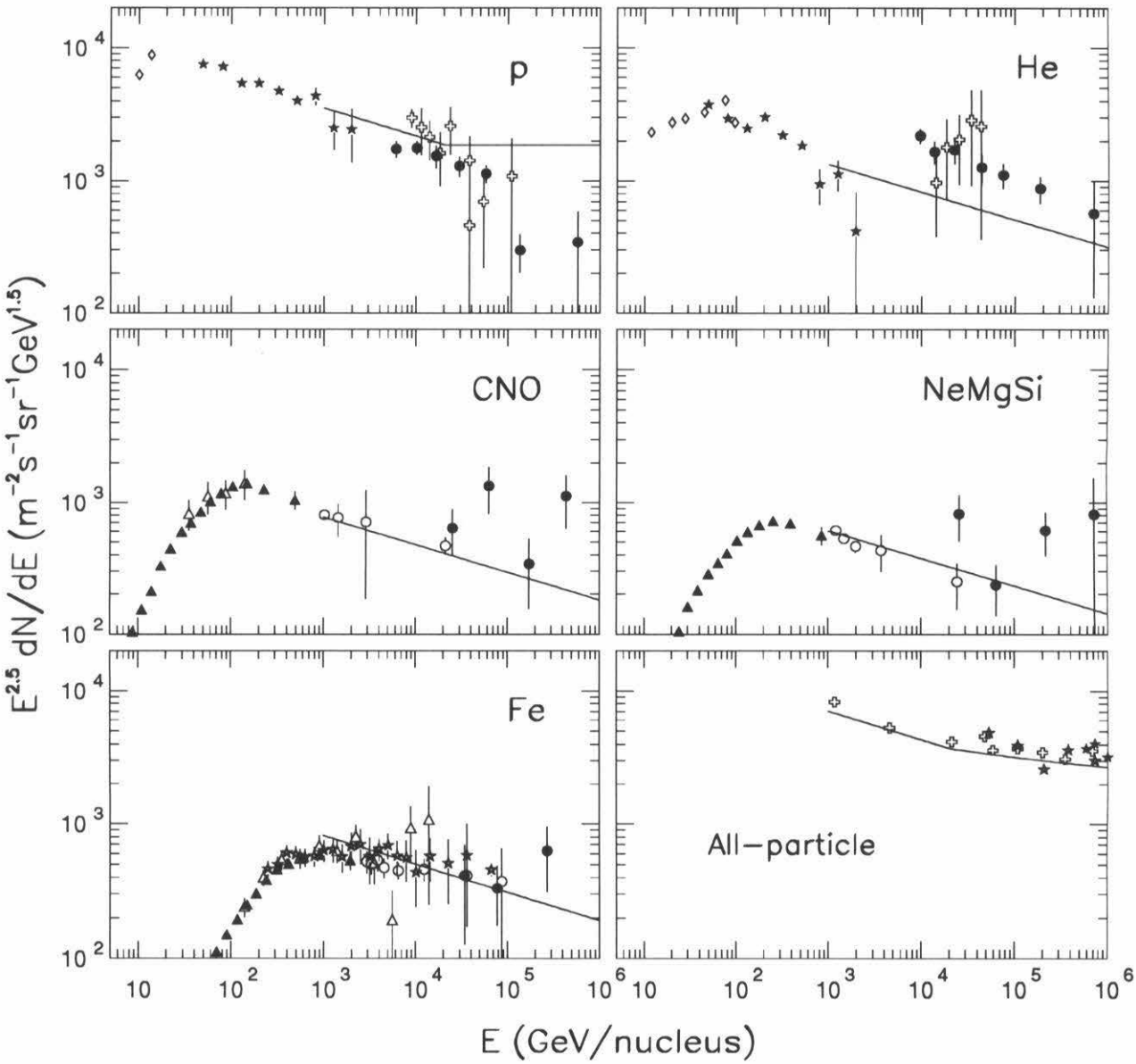

Figure 6.2: Light composition model of Reference [81] (see Table 6.1) in the energy region below 10^6 GeV/nucleus. The data are the same as those of Fig. 1.3.

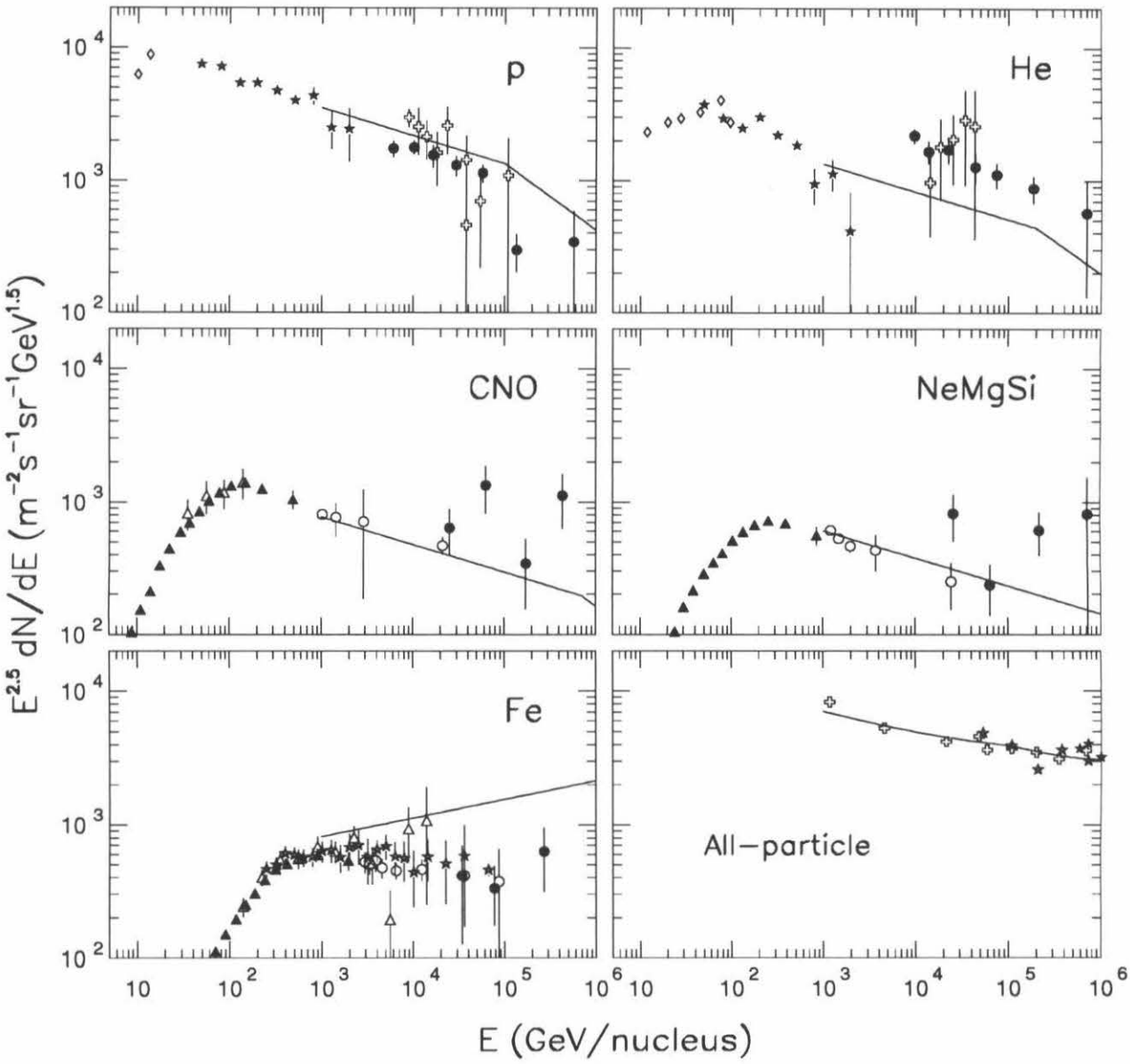

Figure 6.3: Heavy composition model of Reference [81] (see Table 6.1) in the energy region below 10^6 GeV/nucleus. The data are the same as those of Fig. 1.3.

6.1.3 Σ and tailored models

Two more composition models have been devised to agree better with direct measurements than the light and heavy models described above. The first, dubbed "Σ model," is shown in Fig. 6.4. It is designed to agree with the JACEE and other direct composition measurements (in particular, with enhanced CNO and NeMgSi components), without any requirement on the sum of the components compared to the all-particle spectrum. The second model is shown in Fig. 6.5. It is tailored to agree with direct observations between a few thousand GeV and 10^6 GeV (the range of energies yielding anticoincident events, see Section 5.2.1), but also with the all-particle spectrum. The latter requirement forces a relatively flat p spectrum, where the steepening seen by JACEE near 10^5 GeV has to be disregarded.

The evolution of the fractional composition with energy for the last two models is shown in Fig. 6.6 (together with that for the light and heavy models), but only up to 10^6 GeV, since they are specifically designed to agree with direct measurements that do not extend beyond this energy, and no assumption is made here on how they might extrapolate to higher energies. The Σ and tailored models are somewhat intermediate in mass compared to the light and heavy compositions, whereas of course pure p, He or Fe compositions are the most extreme cases.

6.2 Events pointing to within the AC window

Simulations of anticoincident (AC) events are performed according to the prescription of Section 5.1, with the all-p, all-He, all-Fe, light, Σ and tailored models of the previous section as input trial compositions (the heavy model is not used because it is deemed to have an unrealistic Fe spectrum at low energies). The number of showers simulated in each case is that equivalent to a live time of 963 days, ten times longer than the experimental live time of 96.3 days (see Section 4.1). Anticoincident events

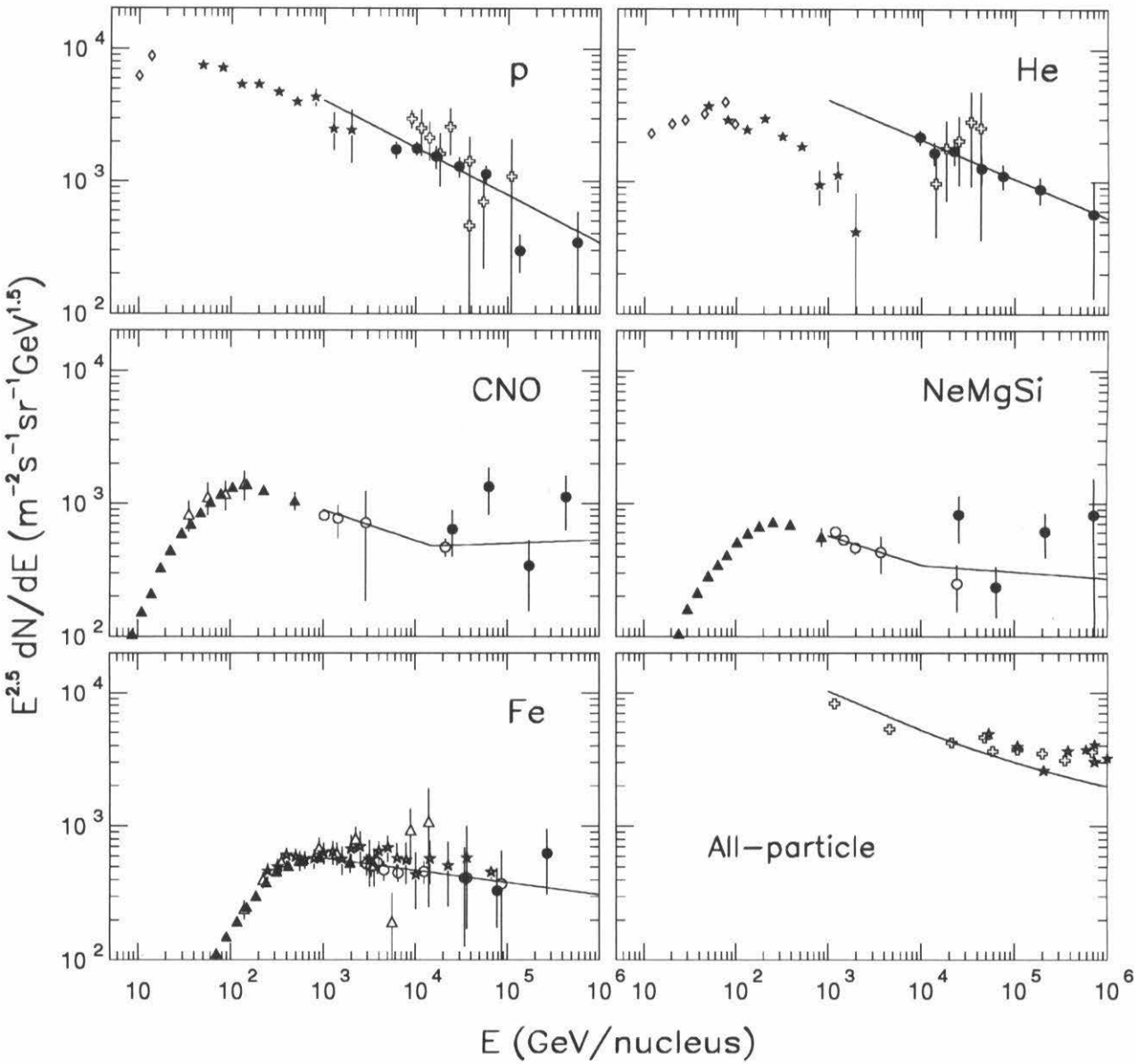

Figure 6.4: Σ composition model designed to match the JACEE data (see Table 6.1) in the energy region below 10^6 GeV/nucleus. The data are the same as those of Fig. 1.3.

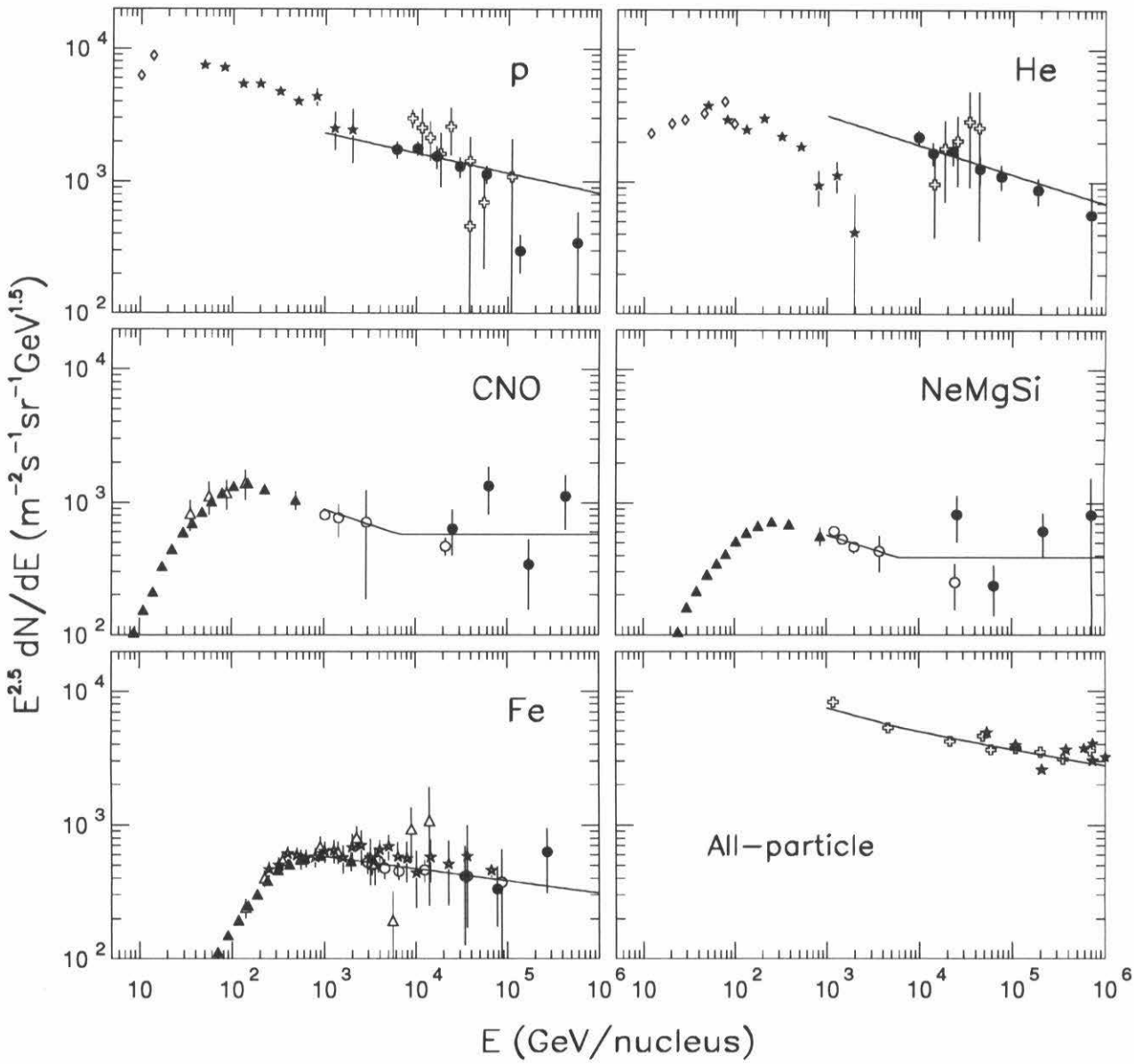

Figure 6.5: Composition model tailored to match the JACEE and all-particle spectra (see Table 6.1) in the energy region below 10^6 GeV/nucleus. The data are the same as those of Fig. 1.3.

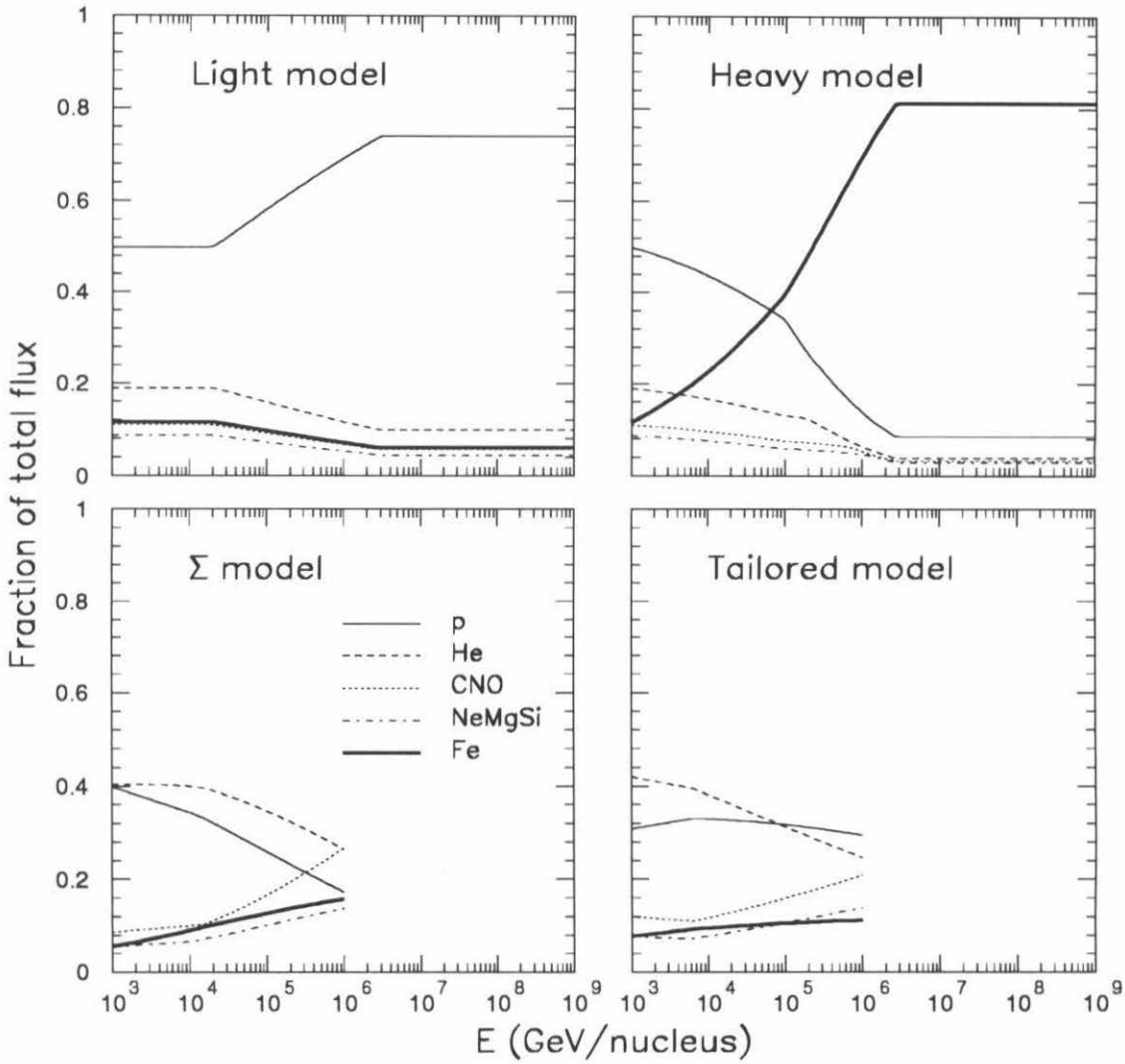

Figure 6.6: Evolution with primary energy (in GeV) of the fractional composition for the light, heavy, Σ and tailored models of Table 6.1.

are obtained by sampling primary energies up to 9×10^5 GeV. Most coincident (C) events also arise from this energy region (see Fig. 5.5), although they tend to be of fairly low multiplicity; therefore, coincident events generated with these simulations can be used to compare with the experimental rate of coincident events pointing to within the fiducial AC window of Eq. 4.4 (but not with the high-multiplicity tail of the experimental N_μ distribution).

6.2.1 Pure compositions

The experimental N_μ distributions for anticoincident and coincident events (within the fiducial AC window) were plotted and summarized in Fig. 4.34 and Table 4.5. In Table 6.2, we summarize the muon multiplicity distributions obtained with the pure compositions (all-p, all-He and all-Fe), for both AC and C events, together with the experimental distributions. Fig. 6.7 shows the same results graphically. Although the energy spectra for these pure models were constructed so as to yield the observed EAS-TOP standalone N_e distribution, they yield muon multiplicities underground that are in disagreement with at least the AC or C experimental distributions. Specifically, the all-p model yields 28% too many AC events, but 45% too few C events, and in both cases the relative number of dimuons compared to single muons is about half that of the experimental result (see Table 6.2). The all-He model yields 38% too few AC events, and 8% too few C events, and again relatively too few dimuons are produced compared to single muons (a deficit of 20% for AC, and 37% for C events). The all-Fe model yields only less than 1% of the observed AC rate, and 25% of the C rate, because too little energy per nucleon is available to produce underground muons. That none of these models agrees with experimental data is not surprising, in view of the fact that the composition at these energies is known to be mixed.

	All-p		All-He		All-Fe		Expt.	
N_μ	AC	C	AC	C	AC	C	AC	C
1	3694	340	1775	565	33	152	2849	567
2	45	24	30	49	0.7	13	61	78
3	1.0	2.8	0.4	6.8		1.5	3	18
4		0.1	0.2	1.3		0.1		4
5		0.1						3
6								1
7								1
8								1
total:	3740	367	1806	622	34	167	2913	673
$\overline{N}_\mu$:	1.0124	1.083	1.018	1.107	1.021	1.099	1.023	1.23
$\pm$	0.0006	0.005	0.001	0.005	0.008	0.008	0.003	0.03

Table 6.2: Muon multiplicity distributions for AC and C events obtained with the all-p, all-He and all-Fe simulations, compared with the experimental distributions. The simulated distributions have been corrected for low-energy sampling bound and angular sampling losses. The uncertainty on each number of events is the square root of that number divided by $\sqrt{10}$, except for the experimental data where uncertainties are those of Table 4.5.

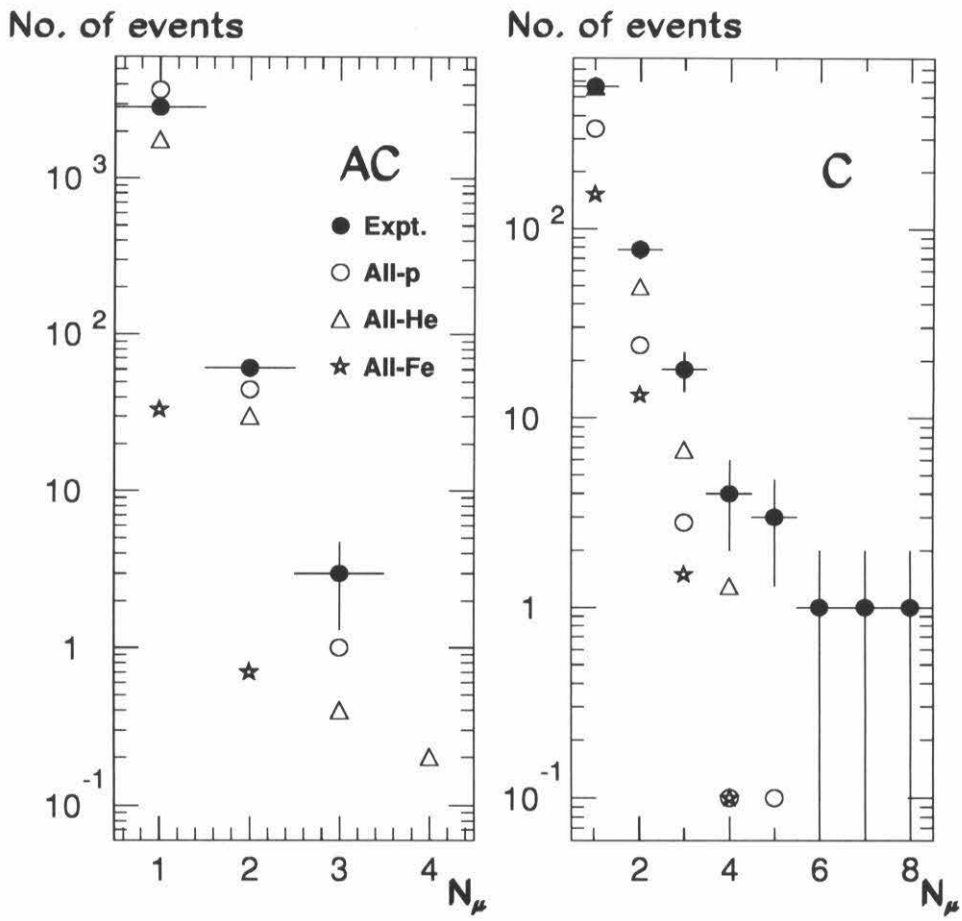

Figure 6.7: Muon multiplicity distributions for AC and C events obtained with the all-p, all-He and all-Fe simulations, compared with the experimental distributions. See Table 6.2. For clarity, uncertainties on the Monte Carlo results are not shown.

6.2.2 Light, Σ and tailored models

In Table 6.3, we summarize the muon multiplicity distributions from each component of the light composition model, for AC and C events, compared with the experimental quantities. The equivalent distributions obtained with the Σ and tailored models are presented in Tables 6.4 and 6.5, respectively. The global multiplicity distributions from each model are compared graphically with the experimental distributions in Fig. 6.8. All three trial compositions result in overall AC and C numbers of events that are lower than the experimental results: for AC events, the light, Σ and tailored models yield 77%, 66% and 67% of the experimental number, respectively, and for C events they yield 75%, 59% and 77% of the experimental number. The deficits in the Monte Carlo rates are compatible with the one observed in calculations of the atmospheric muon spectrum (see Section 5.2.3) in comparison with experimental data. They point to possible problems with the hadronic interaction generator of HEMAS (since the deficit underground is in agreement with that at the surface, the origin of the problem does not lie with the muon propagation treatment in the Monte Carlo or with uncertainties in the rock depth). [1] However, it is worth noting that the deficits observed for AC events are comparable to those for C events, indicative that in the overlap region between the two types of events, where the EAS-TOP trigger efficiency becomes progressively greater with energy, the response of the air shower array is well simulated, and that AC events are not mistaken for C events or vice versa.

The relative proportion of dimuon to single muon events (which is of course independent of normalization) is also lower for all three trial compositions than that for experimental data: for AC events, the light, Σ and tailored models yield an N_2/N_1

[1] In fact, there is some preliminary evidence ([82]) that the FLUKA hadronic interaction generator yields a greater harvest of charged pions in the forward region (with pseudorapidity $\eta > 3$) than HEMAS, by about 20%. This effect would result in greater muon rates underground, in better agreement with our experimental rates.

N_μ	p AC (C)	He AC (C)	CNO AC (C)	NeMgSi AC (C)	Fe AC (C)	Sum AC (C)	Expt. AC (C)
1	1985 (337)	189 (75)	17 (24)	4.1 (12)	1.3 (11)	2196 (459)	2849 (567)
2	31 (25)	3.9 (6.3)	0.2 (1.5)	(2.0)	(1.3)	35 (36)	61 (78)
3	1.3 (4.0)	(0.7)	(0.6)	(0.6)	(0.5)	1.3 (6.4)	3 (18)
4	0.1 (0.3)	(0.3)		(0.3)		0.1 (0.9)	(4)
5	(0.1)			(0.1)		(0.2)	(3)
6	(0.1)					(0.1)	(1)
7							(1)
8							(1)
total:	2017 (366)	193 (82)	17 (26)	4.1 (15)	1.3 (13)	2232 (502)	2913 (673)
$\overline{N}_\mu$:						1.0172 (1.105)	1.023 (1.23)
$\pm$:						0.0009 (0.005)	0.003 (0.03)

Table 6.3: Muon multiplicity distributions for AC and C events obtained with the light composition simulation (the contribution from each mass group is shown), compared with the experimental distributions. The simulated distributions have been corrected for low-energy sampling bound and angular sampling losses. See the remark in the caption of Table 6.2 about uncertainties.

N_μ	p AC (C)	He AC (C)	CNO AC (C)	NeMgSi AC (C)	Fe AC (C)	Sum AC (C)	Expt. AC (C)
1	1442 (133)	415 (144)	33 (47)	7.2 (17)	1.8 (15)	1899 (356)	2849 (567)
2	17 (9.9)	6.2 (14)	0.9 (5.1)	0.3 (2.0)	(1.6)	24 (33)	61 (78)
3	0.7 (1.3)	0.6 (2.2)	(1.3)	(0.2)	(0.3)	1.3 (5.3)	3 (18)
4	(0.1)	(0.4)	(0.2)		(0.1)	(0.8)	(4)
5							(3)
6							(1)
7							(1)
8							(1)
total:	1460 (144)	422 (161)	34 (54)	7.5 (19)	1.8 (17)	1924 (3955)	2913 (673)
$\overline{N}_\mu$:						1.0139 (1.115)	1.023 (1.23)
$\pm$:						0.0009 (0.006)	0.003 (0.03)

Table 6.4: Muon multiplicity distributions for AC and C events obtained with the Σ composition simulation (the contribution from each mass group is shown), compared with the experimental distributions. The simulated distributions have been corrected for low-energy sampling bound and angular sampling losses. See the remark in the caption of Table 6.2 about uncertainties.

N_μ	p AC (C)	He AC (C)	CNO AC (C)	NeMgSi AC (C)	Fe AC (C)	Sum AC (C)	Expt. AC (C)
1	1445 (203)	422 (163)	33 (58)	8.2 (24)	1.8 (15)	1910 (463)	2849 (567)
2	22 (17)	6.5 (16)	1.3 (6.7)	0.2 (2.9)	(1.5)	30 (44)	61 (78)
3	0.7 (2.5)	0.4 (2.7)	0.1 (0.8)	(0.3)	(0.3)	1.2 (6.6)	3 (18)
4	(0.2)	(0.3)	(0.4)	(0.1)	(0.1)	(1.1)	(4)
5	(0.1)		(0.1)			(0.2)	(3)
6							(1)
7							(1)
8							(1)
total:	1468 (223)	429 (182)	34 (66)	8.4 (27)	1.8 (17)	1941 (515)	2913 (673)
$\overline{N}_\mu$:						1.017 (1.119)	1.023 (1.23)
$\pm$:						0.001 (0.005)	0.003 (0.03)

Table 6.5: Muon multiplicity distributions for AC and C events obtained with the tailored composition simulation (the contribution from each mass group is shown), compared with the experimental distributions. The simulated distributions have been corrected for low-energy sampling bound and angular sampling losses. See the remark in the caption of Table 6.2 about uncertainties.

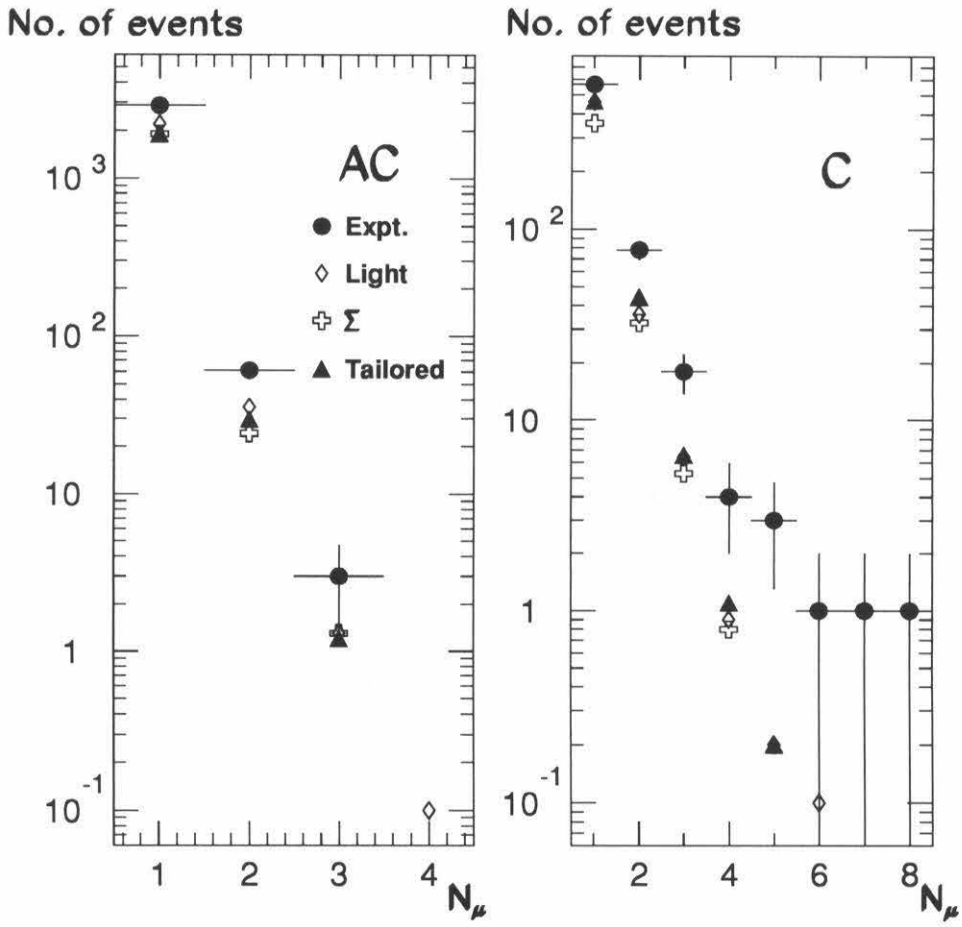

Figure 6.8: Muon multiplicity distributions for AC and C events obtained with the light, Σ and tailored composition simulations, compared with the experimental distributions. See Tables 6.3, 6.4 and 6.5. For clarity, uncertainties on the Monte Carlo results are not shown.

ratio that is 75%, 59% and 73% of the experimental result, respectively, and for C events they yield 57%, 66% and 69% of the experimental number. This indicates that the rate problem in the Monte Carlo generator possibly varies with energy.

These problems are currently under investigation by the authors of the software (see References [75] and [83]). Unfortunately, problems of this kind affect studies of the primary composition based on underground muon data alone (such as that of Reference [23]; see also Fig. 1.4), which rely solely on absolute numbers of events at each multiplicity. Therefore, quantities independent of normalization problems, such as underground muon multiplicity as a function of simultaneous surface shower size (see Section 6.3.3) are of great importance to composition studies. When the difficulties with the hadronic interaction generator are resolved, the anticoincidence data presented here shows some promise in discriminating between various trial compositions (such as the light, Σ and tailored models considered here) in an energy region where direct composition measurements exist, but are however still controversial (greater experimental statistics than available here might be required to make a definitive statement). In particular, this type of study is most sensitive to the protons in the primary flux (which account for between 75 and 90% of the underground muons), as heavier primaries are less efficient at producing deep-underground muons, having less energy per nucleon. An independent confirmation of the steepening in the proton spectrum observed by the JACEE experiment at about 10^5 GeV is highly desirable. He primaries yield between 20 and 10% of the underground muons, and it should be possible to verify the overall normalization of the JACEE He flux, which is somewhat higher than extrapolations of previous measurements at lower energies (see Fig. 1.3). Unfortunately, this is not yet possible here because of the aforementioned problems with the Monte Carlo generator, coupled with still low experimental statistics.

6.3 High-energy, internal coincident events

Simulations of coincident events are performed with the all-p, all-He, all-Fe, light, heavy and Σ trial compositions. The Σ and tailored models, designed to reproduce data below the knee and not extending beyond, are not suitable for studies of very high-energy or large-multiplicity events; of the two, only the Σ model is used here as a first test. The number of events simulated for each trial composition corresponds to the same statistics as the experimental data (a live time of 96.3 days). Only high-energy, internal (HEI) events are simulated and compared with experimental distributions in the following.

6.3.1 Pure compositions

Fig. 6.9 shows the distributions of $\log(N_e)$ obtained with the pure p, He and Fe trial compositions, compared with the experimental result. The knee (as observed by EAS-TOP alone in the (θ,ϕ) direction corresponding to the MACRO/EAS-TOP line-of-sight) is at a $\log(N_e)$ value of about 5.7. The pure proton composition appears to be incompatible with the experimental results at all values of $\log(N_e)$, including above the knee. However, Fig. 6.9 shows absolute numbers of events, which are strongly dependent on the primary spectrum utilized and on possible problems with the Monte Carlo generator such as those discussed in Section 6.2.2.

Table 6.6 summarizes the muon multiplicity distributions obtained with the pure trial compositions, and the information is displayed graphically in Fig. 6.10 (see Table 4.3 and Fig. 4.29 for details of the experimental distribution). Again, the pure proton composition fares poorly compared with the experimental distribution, but the same warning about absolute numbers as above applies here.

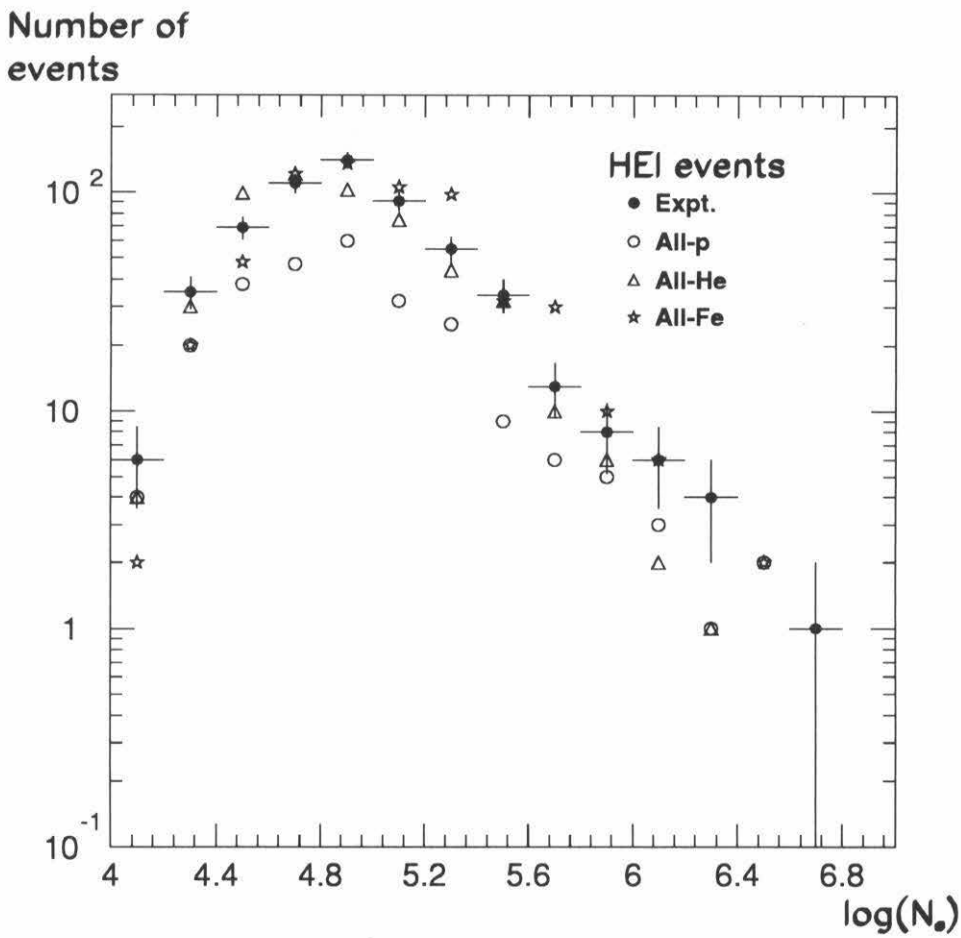

Figure 6.9: Experimental and all-p, all-He and all-Fe simulated $\log(N_e)$ distributions for HEI events. For clarity, uncertainties on the Monte Carlo results are not shown.

N_μ	All-p	All-He	All-Fe†	Expt.
1	198	390	438	394
2	43	99	86	104
3	7	26	32	40
4	3	8	28	17
5	0	4	6	6
6	1	0	10	3
7	0	1	6	7
8	1	1	4	2
9			0	3
10			2	0
11			2	0
12				0
13				0
14				0
15				1
16				0
17				1
18				0
19				0
20				0
21				0
22				0
23				2
total:	253	529	614	580
$\overline{N}_\mu$:	1.31	1.39	1.67	1.74
$\pm$	0.05	0.04	0.08	0.08

Table 6.6: Muon multiplicity distributions for HEI events obtained with the all-p, all-He and all-Fe simulations, compared with the experimental distribution. The uncertainty on each number of events is the square root of that number ($\times\sqrt{2}$ for Fe). † For Fe, only 48 days of live time were simulated, and the results scaled by a factor two.

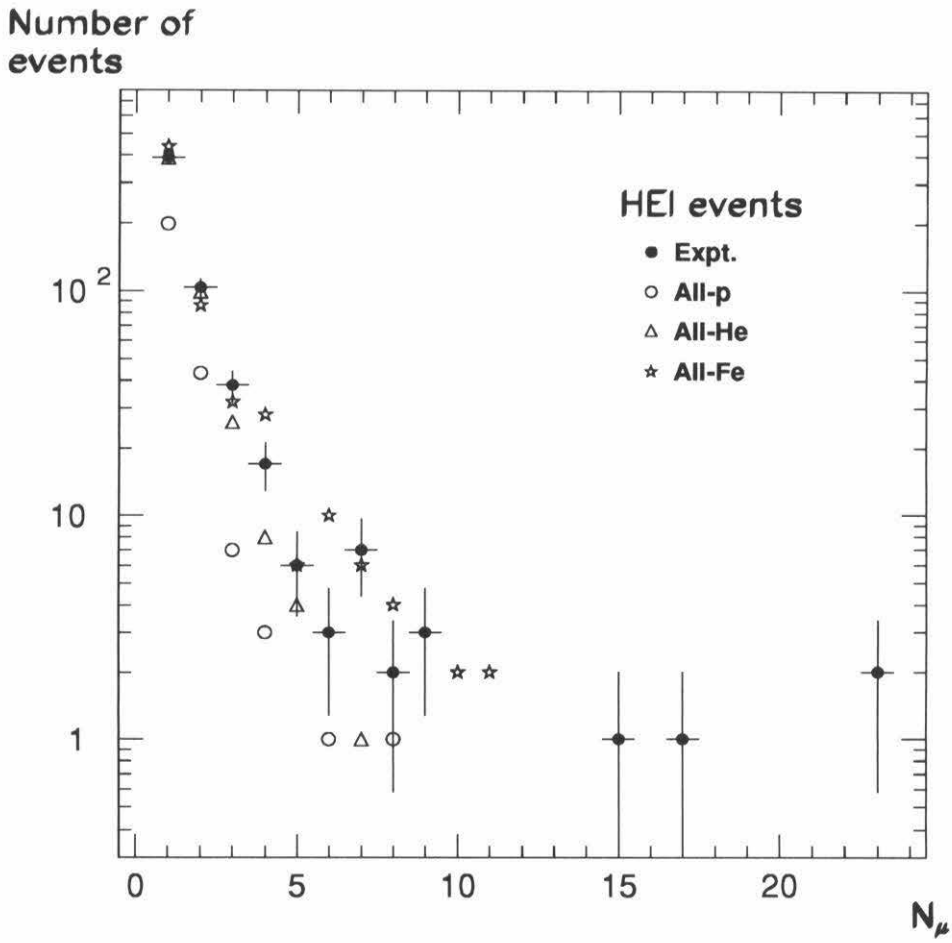

Figure 6.10: Experimental and all-p, all-He and all-Fe simulated N_μ distributions for HEI events. See Table 6.6. For clarity, uncertainties on the Monte Carlo results are not shown.

6.3.2 Light, heavy and Σ models

In Fig. 6.11, we compare the experimental log(N_e) distribution with those obtained with the light, heavy and Σ trial compositions (where the Σ points do not extend beyond the knee). For these three models, no spectrum construction method was used to constrain the EAS-TOP standalone log(N_e) distribution to agree with the experimental one, but here again difficulties with the Monte Carlo rates hamper an unambiguous interpretation of the absolute numbers plotted.

Tables 6.7, 6.8 and 6.9 summarize the muon multiplicity distributions obtained with the light, heavy and Σ trial compositions, respectively, and are graphically displayed in Fig. 6.12 in comparison with experimental data. It is worth noting that while the light model was observed to yield 75% of the experimental single muon rate for coincident events of all kinds (see Table 6.3), here for HEI coincident events it yields 127% of the experimental number. Whereas the former events arose from primaries of energy near 10^5 GeV (see Fig. 5.5), HEI coincident events are due to primaries with a factor of two higher energy. As will be apparent in Fig. 6.15, the excess of the light model over the experimental data increases with shower size, *i.e.*, with primary energy. This could be a new indication of rate problems in the HEMAS generator (this time energy-dependent), which would further complicate the interpretation of the absolute numbers shown in Fig. 6.12. On the other hand, it could be the result of the individual spectra assumed in the light model (in particular the proton abundances could be too high).

It is not possible to discriminate between the light and heavy compositions on the basis of Figs. 6.11 and 6.12. The Σ model yields absolute event rates that are everywhere lower than the experimental rates, but again due to Monte Carlo normalization problems, rate comparisons are problematic; besides, this particular model having been designed to reproduce experimental features at energies below the knee, it is being used here partly outside its range of validity (in Fig. 6.12 especially,

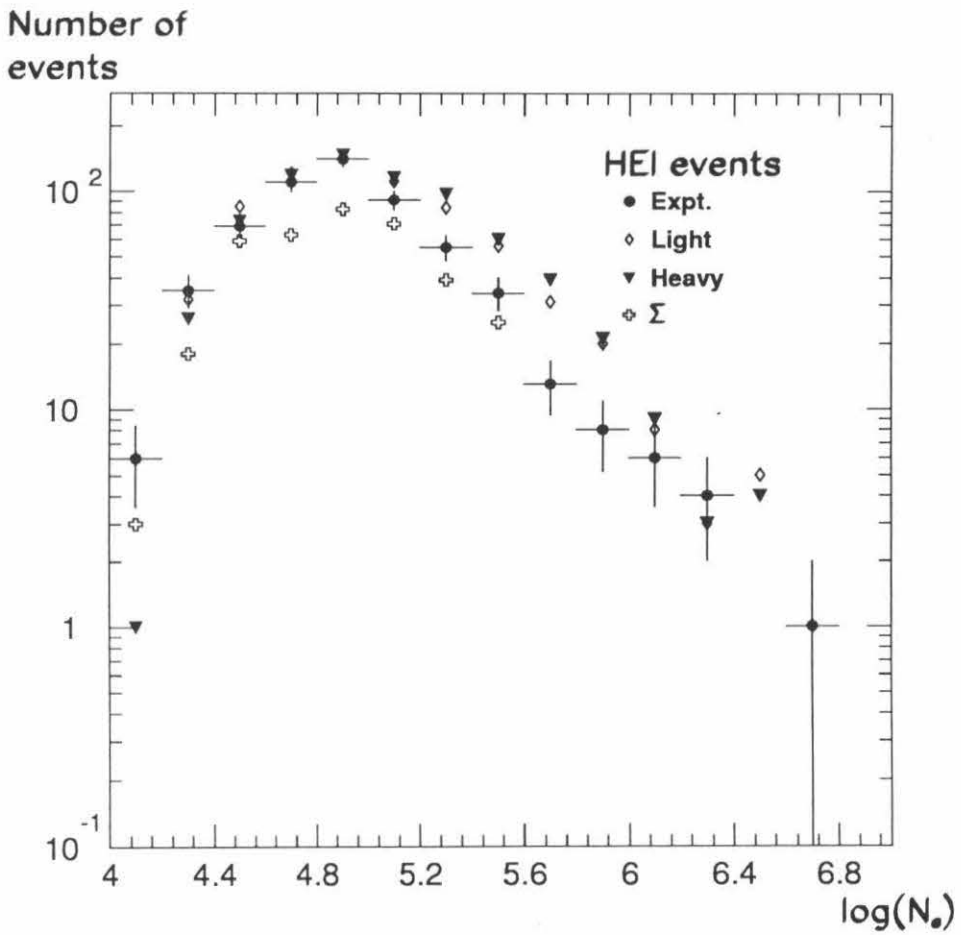

Figure 6.11: Experimental and light, heavy and Σ simulated $\log(N_e)$ distributions for HEI events. For clarity, uncertainties on the Monte Carlo results are not shown.

N_μ	p	He	CNO	NeMgSi	Fe	Sum	Expt.
1	347	76	30	24	22	499	394
2	90	19	12	11	6	138	104
3	26	6	3	3	3	41	40
4	6	1	2	4	2	15	17
5	2	1	1	0	0	4	6
6	3		0	0	0	3	3
7	0		0	0	0	0	7
8	2		1	1	1	5	2
9					1	1	3
10							0
11							0
12							0
13							0
14							0
15							1
16							0
17							1
18							0
19							0
20							0
21							0
22							0
23							2
total:	476	103	49	43	35	706	580
$\overline{N_\mu}$:						1.48	1.74
$\pm$						0.04	0.08

Table 6.7: Muon multiplicity distributions for HEI events obtained with the light composition simulation, compared with the experimental distribution. The uncertainty on each number of events is the square root of that number.

N_μ	p	He	CNO	NeMgSi	Fe	Sum	Expt.
1	125	62	28	23	239	477	394
2	28	14	12	11	70	135	104
3	2	4	2	2	23	33	40
4	2	1	2	4	17	26	17
5	0	1	1	0	10	12	6
6	1		0	0	8	9	3
7	0		0	0	8	8	7
8	1		1	1	5	8	2
9					2	2	3
10					3	3	0
11					1	1	0
12					1	1	0
13					0	0	0
14					0	0	0
15					0	0	1
16					1	1	0
17					0	0	1
18					0	0	0
19					0	0	0
20					0	0	0
21					1	1	0
22							0
23							2
total:	159	82	46	41	389	717	580
$\overline{N}_\mu$:						1.80	1.74
$\pm$						0.07	0.08

Table 6.8: Muon multiplicity distributions for HEI events obtained with the heavy composition simulation, compared with the experimental distribution. The uncertainty on each number of events is the square root of that number.

N_μ	p	He	CNO	NeMgSi	Fe	Sum	Expt.
1	89	122	29	11	25	276	394
2	20	38	7	7	8	80	104
3	1	10	3	1	5	20	40
4	1	4	1		2	8	17
5	0	3	1		2	6	6
6	0		1		0	1	3
7	0		0		2	2	7
8	1		0		2	3	2
9			0			0	3
10			1			1	0
11							0
12							0
13							0
14							0
15							1
16							0
17							1
18							0
19							0
20							0
21							0
22							0
23							2
total:	112	177	43	19	46	397	580
$\overline{N}_\mu$:						1.54	1.74
$\pm$						0.06	0.08

Table 6.9: Muon multiplicity distributions for HEI events obtained with the Σ composition simulation, compared with the experimental distribution. The uncertainty on each number of events is the square root of that number.

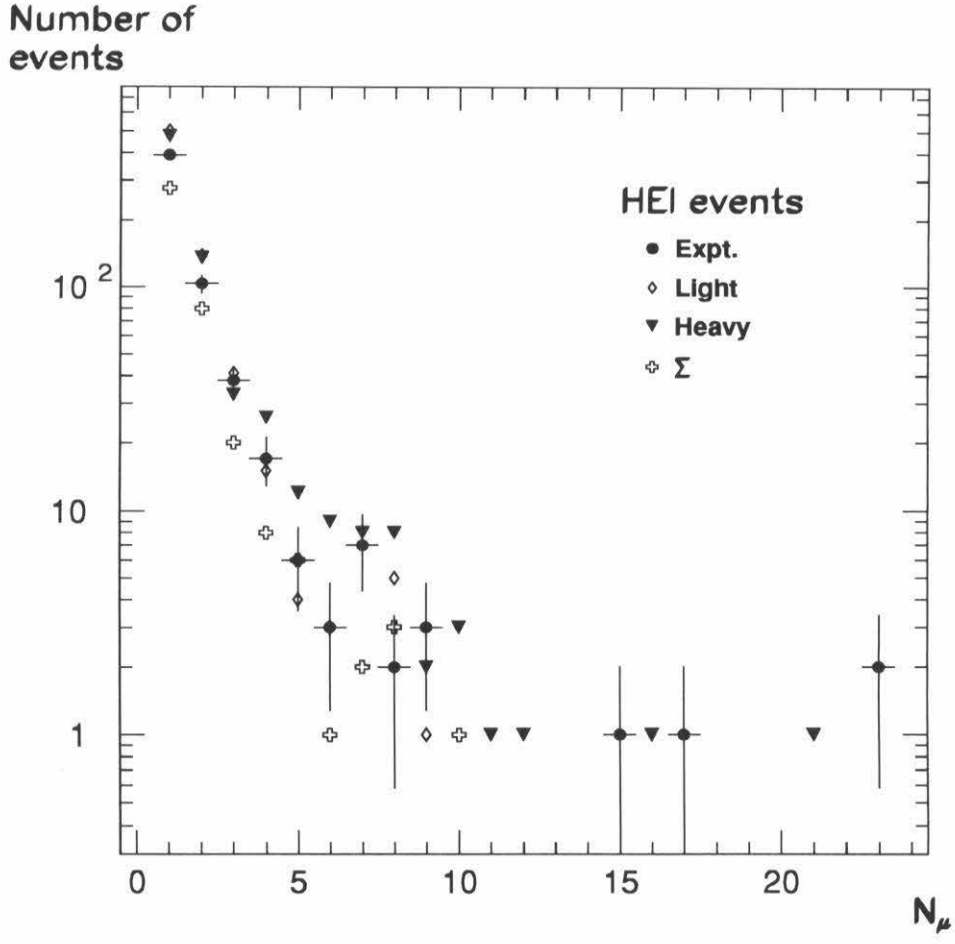

Figure 6.12: Experimental and light, heavy and Σ simulated N_μ distributions for HEI events. See Tables 6.7, 6.8 and 6.9. For clarity, uncertainties on the Monte Carlo results are not shown.

events above the knee would contribute high-multiplicity events, and to a relatively lesser extent, some low-multiplicity events).

We now describe the behavior of deep-underground muon multiplicities as a function of simultaneous surface shower size, a relation that is essentially independent of primary energy spectrum or Monte Carlo normalization problems.

6.3.3 $\overline{N}_\mu - \log(N_e)$ relation

It is clear from the discussions of Sections 6.2.2 and 6.3.2 that the interpretation of underground muon data or surface shower size data alone in terms of primary composition is difficult and much reliant on the assumed energy spectra and details of the Monte Carlo generator. However, the combination of the two is to first order independent of these effects. Indeed, in the approximation that shower size is uniquely related to primary energy, a distribution of muon multiplicity underground as a function of shower size at the surface is independent of the energy spectrum or overall normalization problems in the Monte Carlo generator. It has been verified ([84]) that for a pure proton composition, calculations of the $\overline{N}_\mu - \log(N_e)$ relation (performed using the simulation chain described in Section 5.1) using wildly differing primary energy spectra (*e.g.*, with extreme differential spectral exponents 2.62 or 3.04 everywhere, without a knee) yield the same result within statistical uncertainties.

In the following, we divide the underground muon data for each simulated model into four shower size windows: a) $4.2 < \log(N_e) \leq 4.7$, b) $4.7 < \log(N_e) \leq 5.2$, c) $5.2 < \log(N_e) \leq 5.7$ and d) $5.7 < \log(N_e)$, as was done for experimental data in Section 4.3.1. Then we plot the mean muon multiplicity $\overline{N}_\mu$ as a function of average shower size $\log(N_e)$ for each window. The experimental muon multiplicities for each shower size window were given in Table 4.4 and plotted in Fig. 4.30.

Pure compositions

In Table 6.10, we give the muon multiplicities obtained with the pure trial compositions for each shower size window, and we graphically display the same results in Fig. 6.13 in comparison with experimental data. Then in Fig. 6.14 we plot the mean muon multiplicity $\overline{N}_\mu$ as a function of the log of the shower size $\log(N_e)$. The deficit (mentioned in Section 6.2.2) in simulated multimuon events relative to single muons compared with experimental data is responsible for the disagreement between simulated and experimental data for the lowest shower size bin of Fig. 6.14. At higher shower sizes, we find that the pure proton composition is in disagreement with the experimental data, even near and above the knee (at $\log(N_e)\sim5.7$). For the highest energy bin, where the statistics are admittedly limited, the experimental mean multiplicity is dominated by the four events with 15, 17 and twice 23 muons, and of the pure compositions, only the iron composition yields comparable multiplicities. In a separate, high-statistics simulation of events with $\log(N_e)>6$, it was observed that an all-p composition yields 1.6% of events with $N_\mu \geq 16$, whereas an all-Fe composition yields a fraction of 19%, compared to $\sim$ 30% (3 out of 11 events) for the experimental data. We take this as preliminary evidence that the cosmic ray flux has a heavy component above the knee, but this needs to be confirmed with higher statistics and refined simulations.

Light, heavy and Σ models

The muon multiplicities obtained with the light, heavy and Σ trial compositions for each shower size window are given in Table 6.11 (here again the Σ composition stops at the knee), and plotted in Fig. 6.15 in comparison with the experimental results. The increasing excess with energy of the number of single muons produced by the light composition model compared to the experimental result, which was alluded to above, is apparent in Fig. 6.15. The heavy model follows the same trend. On

	All-p				All-He				All-Fe†			
N_μ	a	b	c	d	a	b	c	d	a	b	c	d‡
1	72	90	22	9	157	187	39	2	102	242	70	55
2	10	20	11	2	23	44	25	7	14	38	28	18
3	2	3	2	0	4	9	9	4		20	12	14
4			2	1		4	3	1		12	14	5
5				0		1	1	2		0	6	4
6				1			0			2	8	2
7				0			1			2	2	6
8				1			1				2	0
9											0	2
10											0	4
11											2	5
12												3
13												1
14												1
15												0
16												3
17												1
18												1
19												2
20												0
21												0
22												1
total:	84	113	37	14	184	245	79	16	116	316	144	128
$\overline{N}_\mu$:	1.17	1.23	1.6	2.2	1.17	1.32	1.9	2.6	1.12	1.43	2.4	4.3
$\pm$	0.05	0.05	0.1	0.6	0.03	0.04	0.1	0.3	0.04	0.08	0.2	0.4

Table 6.10: Muon multiplicity distributions in four shower size windows (for HEI events) obtained with the all-p, all-He and all-Fe simulations. a) $4.2 < \log(N_e) \leq 4.7$, b) $4.7 < \log(N_e) \leq 5.2$, c) $5.2 < \log(N_e) \leq 5.7$ and d) $5.7 < \log(N_e)$. The uncertainty on each number of events is the square root of that number ($\times\sqrt{2}$ for Fe). † For Fe, only 48 days of live time were simulated, and the results scaled by a factor two. ‡ For this bin, the results are from a separate, high-statistics simulation, and only $\overline{N}_\mu$ can be compared to the other bins.

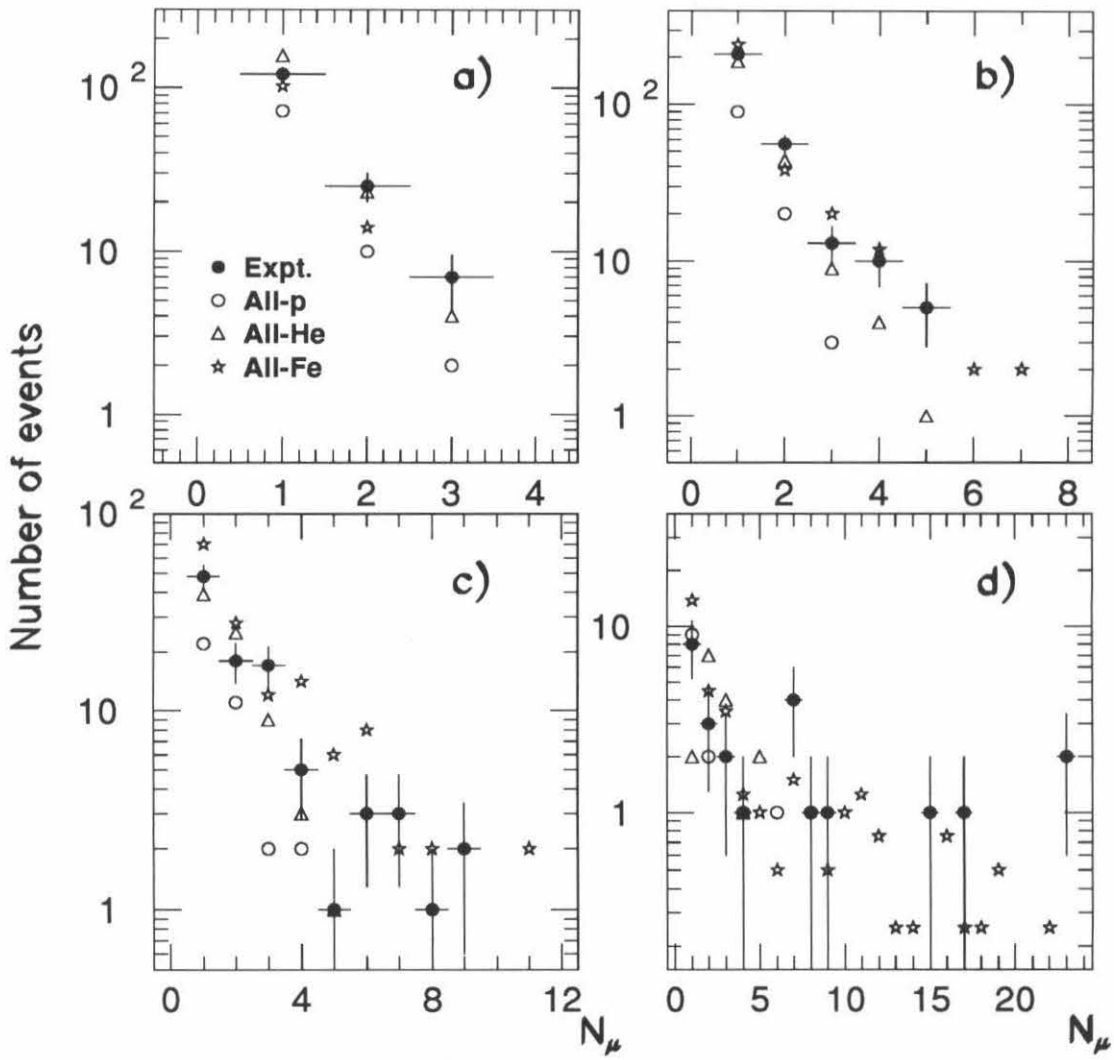

Figure 6.13: Muon multiplicity distributions in four shower size windows (for HEI events) obtained with the all-p, all-He and all-Fe simulations. a) $4.2 < \log(N_e) \leq 4.7$, b) $4.7 < \log(N_e) \leq 5.2$, c) $5.2 < \log(N_e) \leq 5.7$ and d) $5.7 < \log(N_e)$. See Table 6.10. For clarity, uncertainties on the Monte Carlo results are not shown.

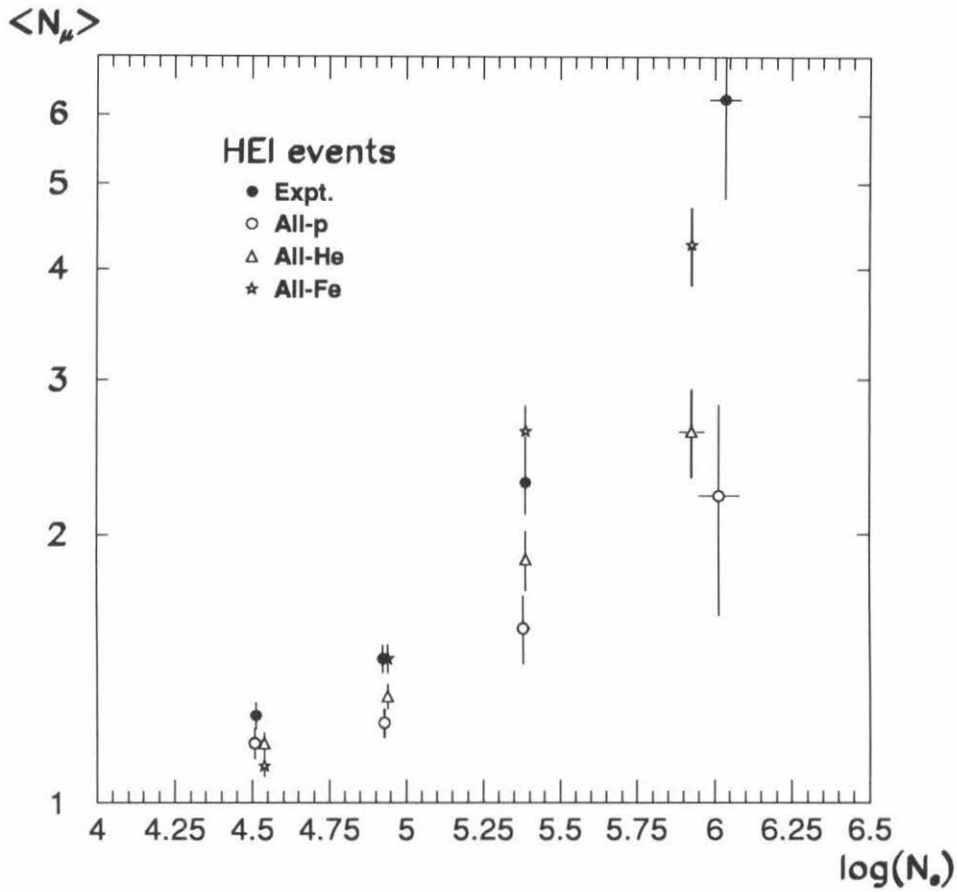

Figure 6.14: $\overline{N}_\mu - \log(N_e)$ relation for the pure composition simulations, compared with the experimental data for HEI events. See Table 6.10.

the other hand, the more realistic (in terms of agreement with direct composition measurements) Σ model has a lower normalization than the data, the same effect that was observed in Section 6.2.2.

The mean muon multiplicity $\overline{N}_\mu$ is plotted as a function of $\log(N_e)$ in Fig. 6.16. In agreement with the observations made for Fig. 6.14, the proton-dominated light composition is not consistent with the experimental data whereas a heavier composition is preferred. The Σ composition is compatible with the experimental results.

Note that this preference towards a heavy composition at and above the knee is in contradiction with the results of Reference [23], obtained by analysis of MACRO data alone (see also Fig. 1.4), where a light composition was preferred. The calculations for that analysis had been performed using parametrizations of results obtained with the same Monte Carlo generator as that used in the work presented here. Therefore, the MACRO-standalone results were afflicted with the rate problems mentioned in this chapter and the last. When the rate problems in the generator are solved, the MACRO-standalone analysis will have to be revised, and will hopefully be found in agreement with the one presented here.

	Light				Heavy				Σ		
N_μ	a	b	c	d	a	b	c	d	a	b	c
1	147	231	93	23	131	229	89	25	92	132	33
2	31	60	37	8	27	68	33	7	13	39	21
3	5	10	15	11	2	14	13	4		12	4
4		4	9	2		6	15	5		4	3
5		1	2	1		1	10	1		1	4
6		1	0	2		1	5	3		0	0
7			0	0		1	4	3		1	1
8			3	2			5	3			1
9				1			0	2			
10							0	3			
11							1	0			
12							1	0			
13								0			
14								0			
15								0			
16								1			
17								0			
18								0			
19								0			
20								0			
21								1			
total:	183	307	159	50	160	320	176	58	105	189	67
$\overline{N}_\mu$:	1.22	1.33	1.8	2.4	1.19	1.40	2.4	3.9	1.12	1.45	2.0
$\pm$	0.04	0.04	0.1	0.3	0.03	0.05	0.2	0.5	0.03	0.06	0.2

Table 6.11: Muon multiplicity distributions in four shower size windows (for HEI events) obtained with the light, heavy and Σ composition simulations. a) $4.2 < \log(N_e) \leq 4.7$, b) $4.7 < \log(N_e) \leq 5.2$, c) $5.2 < \log(N_e) \leq 5.7$ and d) $5.7 < \log(N_e)$. The uncertainty on each number of events is the square root of that number.

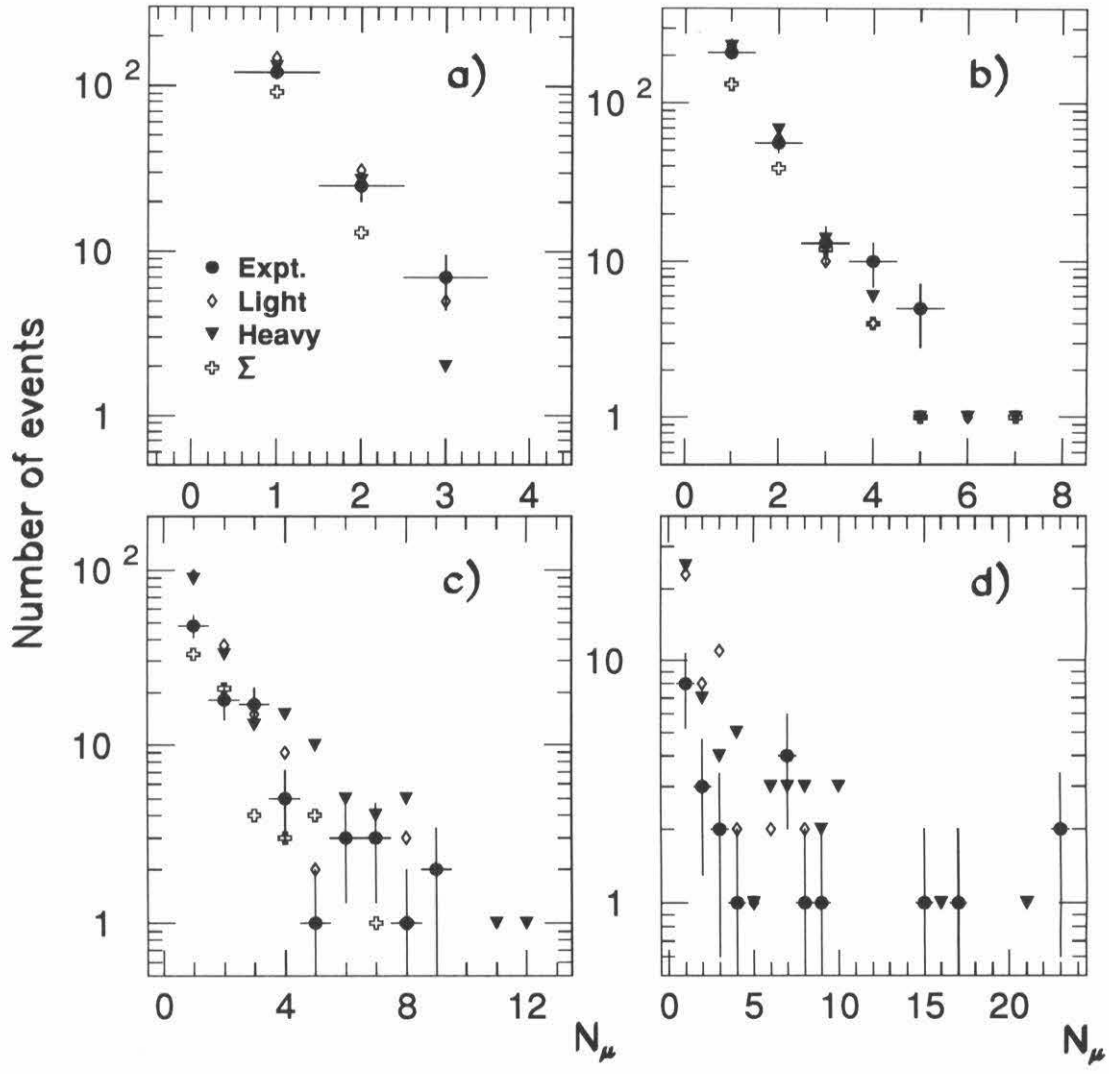

Figure 6.15: Muon multiplicity distributions in four shower size windows (for HEI events) obtained with the light, heavy and Σ composition simulations. a) $4.2 < \log(N_e) \leq 4.7$, b) $4.7 < \log(N_e) \leq 5.2$, c) $5.2 < \log(N_e) \leq 5.7$ and d) $5.7 < \log(N_e)$. See Table 6.11. For clarity, uncertainties on the Monte Carlo results are not shown.

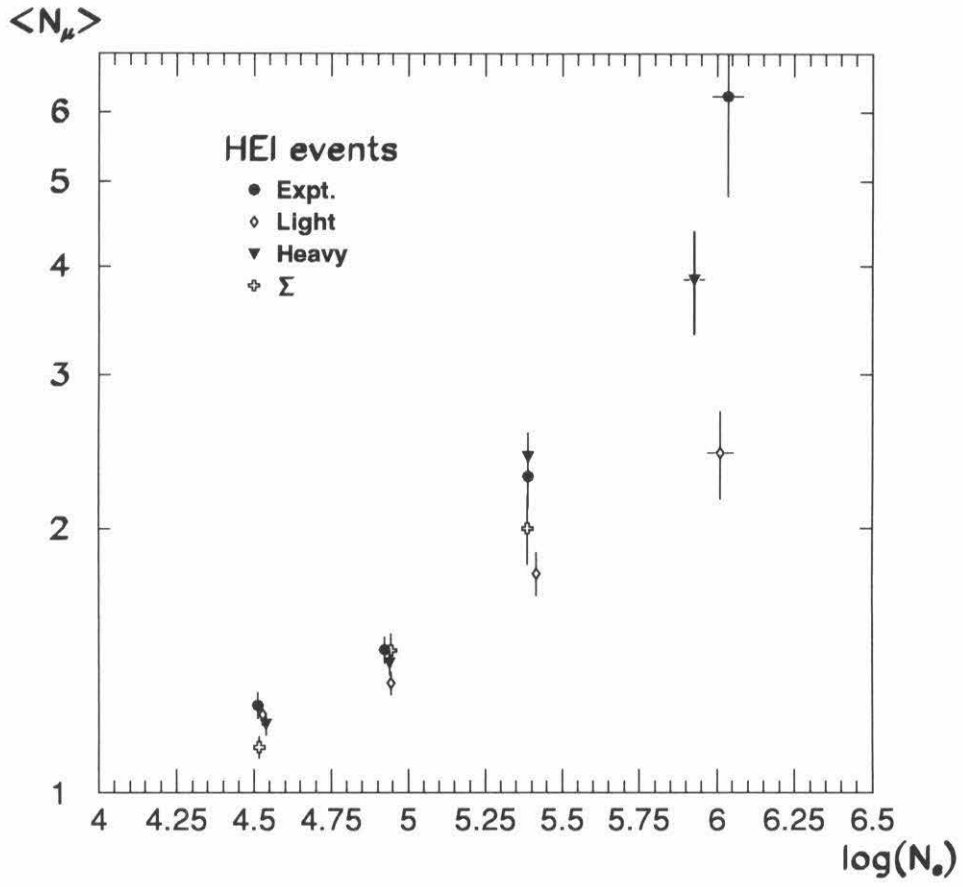

Figure 6.16: $\overline{N}_\mu - \log(N_e)$ relation for the light, heavy and Σ composition simulations, compared with the experimental data for HEI events. See Table 6.11.

Chapter 7

Conclusions

7.1 Experimental results

The combination of deep underground muon bundles from MACRO with surface shower information from EAS-TOP, in anticoincidence or in coincidence, yields data of excellent quality, with little (and unambiguously identifiable) contamination by chance coincidences. The experimental muon multiplicity distributions obtained for various surface trigger configurations follow the qualitative expectation that the mean multiplicity increases with increasing primary energy, from anticoincident events up to high-energy, internal coincident events.

7.2 Composition results

Using various trial composition models as input to a chain of Monte Carlo simulation programs based on accelerator measurements, muon multiplicity distributions underground, shower size distributions at the surface, and muon multiplicity versus shower size distributions are generated and compared with the experimental data, and found to yield approximately the correct shapes.

Detailed studies of anticoincident events (which arise from a primary energy region where the cosmic ray composition has been measured directly by satellite and balloon detectors) have unearthed some shortcomings in the Monte Carlo generator, where between 25 and 40% too few muons are produced below a few times 10^5 GeV compared to the experimental data. This effect is in agreement with a comparison of calculated atmospheric muon rates with those inferred from MACRO-standalone muon data. Differences between the ratio of number of dimuon events to number of single muon events for Monte Carlo and experimental data suggest that the problems with the generator are energy-dependent.

For coincident events, simulated shower size and muon multiplicity distributions show that a pure proton composition is inconsistent with the experimental distributions, even at and above the knee in the primary spectrum. This conclusion is further reinforced by comparisons between experimental and simulated $\overline{N}_\mu - \log(N_e)$ relations, where also the proton-dominated, light composition model is found to disagree with experimental results. A heavier composition is preferred, but a firmer conclusion awaits refinements in the Monte Carlo algorithms and the increased statistics of recent periods of simultaneous data taking.

7.3 Future developments

The experimental data described and used in this thesis had been collected in 1990, with 29 EAS-TOP scintillation stations and two MACRO supermodules in operation. In December of that year, simultaneous data collection was interrupted due to severe damage to the surface array caused by snow avalanches. The array was rebuilt during 1991 and 1992, whereas construction of MACRO continued to expand it to six supermodules. In 1992, both detectors ran simultaneously for 172 days with six MACRO supermodules and 29 EAS-TOP stations, during which time about 42,000

coincident events were collected. In 1992-1993, during 75 days of combined operation, about 21,000 further coincident events were collected with EAS-TOP now expanded to 35 stations. This data remains to be reconstructed and analyzed, and the greatly improved statistics will allow more refined composition studies with finer shower size windows, especially in the high muon multiplicity region. In addition, larger shower sizes, and therefore higher primary energies will be attained. The eventual reconstruction of events other than those of the high-energy, internal type will also increase the statistical power of the data.

Other expected improvements concern the Monte Carlo software, where current muon production problems will hopefully be resolved. Although the superposition approximation was used in nucleus-nucleus interactions here, more realistic nuclear fragmentation algorithms have been devised and are under test. Other refinements to the code are in progress, such as the addition of terrestrial magnetic field effects on muon propagation.

Appendix A

MACRO and EAS-TOP collaborations

The MACRO Collaboration

S. Ahlen,[3] M. Ambrosio,[12] R. Antolini,[2] G. Auriemma,[14*] A. Baldini,[13] B.B. Bam,[2] G.C. Barbarino,[12] B.C. Barish,[4] G. Battistoni,[6] R. Bellotti,[1] C. Bemporad,[13] P. Bernardini,[10] H. Bilokon,[6] V. Bisi,[16] C. Bloise,[6] S. Bussino,[14] F. Cafagna,[1] M. Calicchio,[1] D. Campana,[12] P. Campana,[6] M. Carboni,[6] S. Cecchini,[2•] F. Cei,[13] V. Chiarella,[6] C. Chiera,[14] A. Cobis,[6] R. Cormack,[3] A. Corona,[14] S. Coutu,[4,11] G. DeCataldo,[1] C. DeMarzo,[1] M. De Vincenzi,[14] A. Di Credico,[9] E. Diehl,[11] O. Erriquez,[1] C. Favuzzi,[1] D. Ficenec,[3o] C. Forti,[6] L. Foti,[14] P. Fusco,[1] G. Giacomelli,[2] G. Giannini,[13*] N. Giglietto,[1] P. Giubellino,[16] M. Grassi,[13] P. Green,[18] A. Grillo,[6] F. Guarino,[12] C. Gustavino,[7] A. Habig,[8] R. Heinz,[8] J.T. Hong,[3] E. Iarocci,[6†] E. Katsavounidis,[4] E. Kearns,[3] S. Klein,[3‡] S. Kyriazopoulou,[4] E. Lamanna,[14] C. Lane,[5] C. Lee,[11] D. Levin,[11] P. Lipari,[14] G. Liu,[4] R. Liu,[4] M.J. Longo,[11] G. Ludlam,[3] G. Mancarella,[10] G. Mandrioli,[2] A. Margiotta-Neri,[2] A. Marin,[3] A. Marini,[6] D. Martello,[10] G. Martellotti,[14] A. Marzari Chiesa,[16] M. Masera,[16] P. Matteuzzi,[2] D.G. Michael,[4] L. Miller,[8] P. Monacelli,[9] M. Monteno,[16] S. Mufson,[8] J. Musser,[8] S. Nutter,[11] C. Okada,[3] G. Osteria,[12] O. Palamara,[10] S. Parlati,[7] V. Patera,[6] L. Patrizii,[2] R. Pazzi,[13] C.W. Peck,[4] J. Petrakis,[17] S. Petrera,[10] N.D. Pignatano,[4] P. Pistilli,[10] F. Predieri,[2] L. Ramello,[16] J. Reynoldson,[7] F. Ronga,[6] G. Rosa,[14] C. Satriano,[14*] L. Satta,[6†] E. Scapparone,[2] K. Scholberg,[4] A. Sciubba,[14†] P. Serra Lugaresi,[2] M.

Severi,[14] M. Sitta,[16] P. Spinelli,[1] M. Spinetti,[6] M. Spurio,[2] J. Steele,[4] R. Steinberg,[5] J.L. Stone,[3] L.R. Sulak,[3] A. Surdo,[10] G. Tarlé,[11] V. Togo,[2] V. Valente,[6] G.R. Verdone,[14*] C.W. Walter,[4] R. Webb,[15] W. Worstell,[3].

1. Dipartimento di Fisica dell'Universitá di Bari and INFN, Bari, 70126, Italy
2. Dipartimento di Fisica dell'Universitá di Bologna and INFN, Bologna, 40126, Italy
3. Physics Department, Boston University, Boston, MA 02215, USA
4. California Institute of Technology, Pasadena, CA 91125, USA
5. Department of Physics, Drexel University, Philadelphia, PA 19104, USA
6. Laboratori Nazionali di Frascati dell'INFN, Frascati (Roma), 00044, Italy
7. Laboratori Nazionali del Gran Sasso dell'INFN, Assergi (L'Aquila), 67010, Italy
8. Departments of Physics and of Astronomy, Indiana University, Bloomington, IN 47405, USA
9. Dipartimento di Fisica dell'Universitá dell'Aquila and INFN, L'Aquila, 67100, Italy
10. Dipartimento di Fisica dell'Universitá di Lecce and INFN, Lecce, 73100, Italy
11. Department of Physics, University of Michigan, Ann Arbor, MI 48109, USA
12. Dipartimento di Fisica dell'Universitá di Napoli and INFN, Napoli, 80125, Italy
13. Dipartimento di Fisica dell'Universitá di Pisa and INFN, Pisa, 56010, Italy
14. Dipartimento di Fisica dell'Universitá di Roma and INFN, Roma, 00185, Italy
15. Physics Department, Texas A&M University, College Station, TX 77843, USA
16. Dipartimento di Fisica dell'Universitá di Torino and INFN, Torino, 10125, Italy
17. Bartol Research Institute, University of Delaware, Newark, DE 19716, USA
18. Sandia National Laboratory, Albuquerque, NM 87185, USA

∗ Also universitá della Basilicata, Potenza, 85100, Italy

• Also Istituto TESRE/CNR, Bologna, Italy

o Now at Physics Department, Washington University, St Louis, MO 63130, USA

⋆ Also Universitá di Trieste and INFN, Trieste, 34100, Italy

† Also Dipartimento di Energetica, Universitá di Roma, Roma, 00185, Italy

‡ Now at Department of Physics, University of California, Santa Cruz, CA 95064

The EAS-TOP Collaboration

M. Aglietta,[2,3] B. Alessandro,[3] F. Arneodo,[1,3] L. Bergamasco,[1,3] C. Castagnoli,[2,3] A. Castellina,[2,3] C. Cattadori,[4] A. Chiavassa,[1,3] G. Cini,[1,3] B. D'Ettorre Piazzoli,[2,3] W. Fulgione,[2,3] P. Galeotti,[1,3] P.L. Ghia,[2,3] G. Mannocchi,[2,3] C. Morello,[2,3] G. Navarra,[1,3] L. Riccati,[3] O. Saavedra,[1,3] G.C. Trinchero,[2,3] P. Vallania,[2,3] S. Vernetto,[2,3]

1. Istituto di Fisica Generale dell'Universitá, Torino, Italy
2. Istituto di Cosmo-Geofisica del CNR, Torino, Italy
3. Istituto Nazionale di Fisica Nucleare, Torino, Italy
4. Laboratorio Nazionale del Gran Sasso, INFN, Italy

Appendix B

Parameters for Reconstruction Comparison

In this appendix, we perform various calculations of relevance to the comparison of independent reconstructions by EAS-TOP and MACRO of coincident events.

B.1 Relevance of $(1 - \cos\psi)$

In Section 4.2.2, we state that $(1 - \cos\psi)$ is a parameter with a more transparent distribution to study than ψ, where ψ is the angle in space between the MACRO and EAS-TOP reconstructed directions and is defined by Eq. 4.2. To show this, we begin by defining two unit vectors $\hat{x}_{\rm M}$ and $\hat{x}_{\rm E}$ along the directions reconstructed by MACRO and EAS-TOP, respectively. In Cartesian coordinates, they are expressed in terms of the zenith angles $\theta_{\rm M}$ and $\theta_{\rm E}$, and azimuth angles $\phi_{\rm M}$ and $\phi_{\rm E}$ as:

$$\begin{cases} \hat{x}_{\rm M} = (\sin\theta_{\rm M}\cos\phi_{\rm M}, \sin\theta_{\rm M}\sin\phi_{\rm M}, \cos\theta_{\rm M}) \\ \hat{x}_{\rm E} = (\sin\theta_{\rm E}\cos\phi_{\rm E}, \sin\theta_{\rm E}\sin\phi_{\rm E}, \cos\theta_{\rm E}) \end{cases} \tag{B.1}$$

and therefore the angle ψ between them, obtained by taking their dot product, is:

$$\cos\psi \;=\; \hat{x}_{\rm M}\cdot\hat{x}_{\rm E} \tag{B.2}$$

$$= \cos\theta_M \cos\theta_E + \sin\theta_M \sin\theta_E(\cos\phi_M \cos\phi_E + \sin\phi_M \sin\phi_E) \quad \text{(B.3)}$$

$$= \cos\theta_M \cos\theta_E + \sin\theta_M \sin\theta_E \cos(\phi_M - \phi_E) \quad \text{(B.4)}$$

$$= \tfrac{1}{2}[\cos(\Delta\theta) + \cos(2\bar{\theta}) + \cos(\Delta\theta)\cos(\Delta\phi) - \cos(2\bar{\theta})\cos(\Delta\phi)] \quad \text{(B.5)}$$

$$= \tfrac{1}{2}[\cos(\Delta\theta)(1 + \cos(\Delta\phi)) + \cos(2\bar{\theta})(1 - \cos(\Delta\phi))] \quad \text{(B.6)}$$

where in the step before last we have defined $\Delta\theta = \theta_M - \theta_E$, $\Delta\phi = \phi_M - \phi_E$ and $\bar{\theta} = \frac{1}{2}(\theta_M + \theta_E)$ and we have used $\cos\theta_M \cos\theta_E = \frac{1}{2}[\cos(\Delta\theta) + \cos(2\bar{\theta})]$ and $\sin\theta_M \sin\theta_E = \frac{1}{2}[\cos(\Delta\theta) - \cos(2\bar{\theta})]$.

We now make the approximations $\cos(\Delta\theta) \simeq 1 - \frac{1}{2}(\Delta\theta)^2$ and $\cos(\Delta\phi) \simeq 1 - \frac{1}{2}(\Delta\phi)^2$, which are justified by $|\Delta\theta| \lesssim 1.23° = 0.021$ radians $\ll 1$ (see Fig. 4.19) and by $|\Delta\phi| \lesssim 2.22° = 0.039$ radians $\ll 1$ (see Fig. 4.20), and we obtain:

$$\cos\psi \simeq \tfrac{1}{2}[(1 - \tfrac{1}{2}(\Delta\theta)^2)(2 - \tfrac{1}{2}(\Delta\phi)^2) + \tfrac{1}{2}\cos(2\bar{\theta})(\Delta\phi)^2] \quad \text{(B.7)}$$

$$\simeq 1 - \tfrac{1}{2}(\Delta\theta)^2 - \tfrac{1}{2}\left(\frac{1 - \cos(2\bar{\theta})}{2}\right)(\Delta\phi)^2 \quad \text{(B.8)}$$

$$\simeq 1 - \tfrac{1}{2}(\Delta\theta)^2 - \tfrac{1}{2}[\sin\bar{\theta}(\Delta\phi)]^2 \quad \text{(B.9)}$$

where we have neglected the term in $(\Delta\theta)^2(\Delta\phi)^2$. Therefore:

$$1 - \cos\psi \simeq \tfrac{1}{2}[(\Delta\theta)^2 + (\sin\bar{\theta}(\Delta\phi))^2] \quad \text{(B.10)}$$

As is apparent in Fig. 4.19, the distribution of $\Delta\theta$ is approximately Gaussian, with mean near zero and standard deviation $\sigma_\theta = (1.23 \pm 0.05)°$; hence the probability density function for $\Delta\theta$ is:

$$f(\Delta\theta) \simeq \frac{1}{\sqrt{2\pi}\sigma_\theta} \exp\left(-\frac{(\Delta\theta)^2}{2{\sigma_\theta}^2}\right) \quad \text{(B.11)}$$

Fig. B.1 shows the experimental distribution of $\sin\bar{\theta}(\Delta\phi)$ for HEI events; it is approximately Gaussian with mean $\mu_\phi = (0.49 \pm 0.05)°$ and standard deviation $\sigma_\phi = (1.22 \pm 0.05)°$, and the probability density function for $\sin\bar{\theta}(\Delta\phi)$ is thus:

$$f(\sin\bar{\theta}(\Delta\phi)) \simeq \frac{1}{\sqrt{2\pi}\sigma_\phi} \exp\left(-\frac{(\sin\bar{\theta}(\Delta\phi) - \mu_\phi)^2}{2{\sigma_\phi}^2}\right) \quad \text{(B.12)}$$

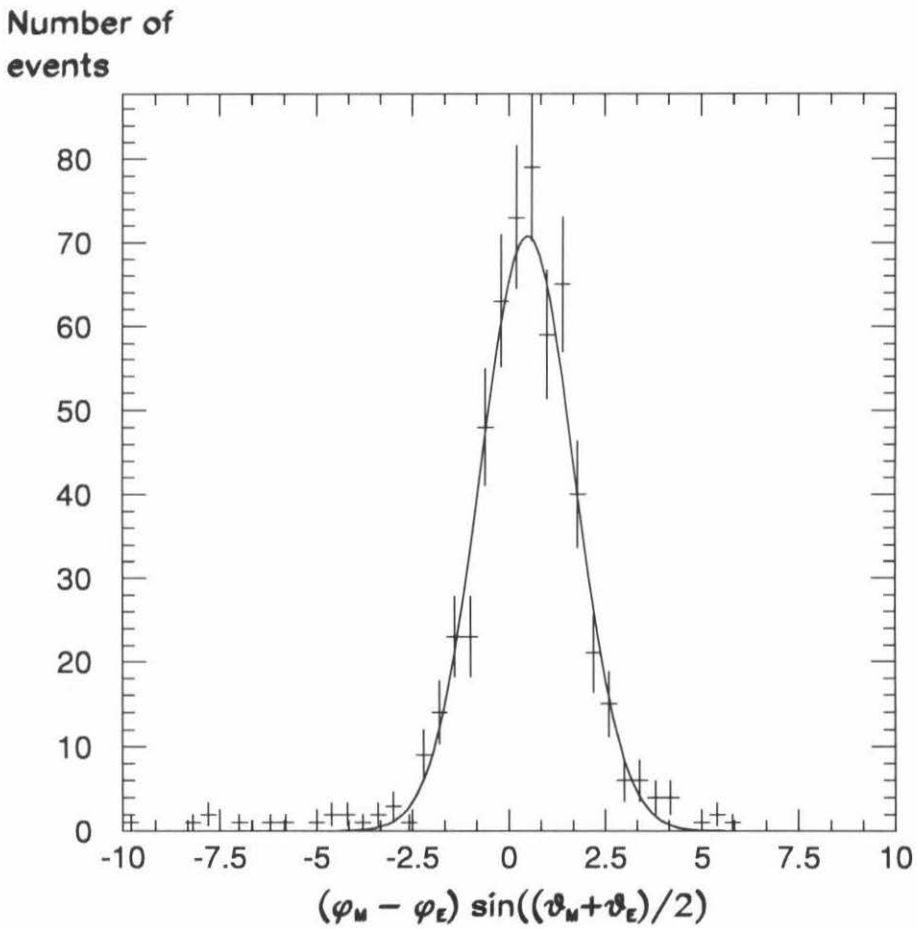

Figure B.1: Distribution of $\sin\bar{\theta}(\Delta\phi)$ (in degrees) for HEI events. The curve is a Gaussian fit with mean $(0.49 \pm 0.05)°$ and standard deviation $(1.22 \pm 0.05)°$. Three events overflow the bounds of the plot.

$\Delta\theta$ and $\Delta\phi$ are independent (see footnote on page 182); θ_M and θ_E vary over a range of only a few degrees (see Figs. 4.16 and 4.18), and thus $\sin\bar{\theta}$ is approximately constant; therefore $\Delta\theta$ and $\sin\bar{\theta}(\Delta\phi)$ are approximately independent, and their combined probability density function is just the product of the two given by Eqs. B.11 and B.12. Defining $\sigma_\psi \equiv \sigma_\theta = 1.23^\circ \simeq \sigma_\phi$, we obtain:

$$f(\Delta\theta, \sin\bar{\theta}(\Delta\phi)) \simeq \frac{1}{2\pi{\sigma_\psi}^2} \exp\left(-\frac{(\Delta\theta)^2 + (\sin\bar{\theta}(\Delta\phi) - \mu_\phi)^2}{2{\sigma_\psi}^2}\right) \quad \text{(B.13)}$$

$$\simeq \frac{1}{2\pi{\sigma_\psi}^2} \exp\left(-\frac{(1-\cos\psi) + \frac{1}{2}{\mu_\phi}^2 - \mu_\phi \sin\bar{\theta}(\Delta\phi)}{{\sigma_\psi}^2}\right) \quad \text{(B.14)}$$

where we have used Eq. B.10 in the last step. In the exponential, the term in $(1-\cos\psi)$ is of order 10^{-3} (see Fig. 4.22), the term in ${\mu_\phi}^2$ is of order 10^{-5} and the term in $\mu_\phi \sin\bar{\theta}(\Delta\phi)$ is of order 10^{-4}. Therefore, approximately:

$$f(\Delta\theta, \sin\bar{\theta}(\Delta\phi)) \approx \frac{1}{2\pi{\sigma_\psi}^2} \exp\left(-\frac{1-\cos\psi}{{\sigma_\psi}^2}\right) \quad \text{(B.15)}$$

and we expect the distribution of $(1-\cos\psi)$ to be exponential with a slope ${\sigma_\psi}^2 = 4.6 \times 10^{-4}$.

B.2 Relevance of $(\Delta R)^2$

In Section 4.2.3, we state that the distribution of the square of the separation between the MACRO and EAS-TOP core locations, $(\Delta R)^2$, is more transparent to study than that of ΔR. To motivate this, we first note from Figs. 4.25 and 4.26 that the distributions of $\Delta X = X_M - X_E$ and $\Delta Y = Y_M - Y_E$ are approximately Gaussian, and therefore that their probability density functions are given by:

$$f(\Delta X) \simeq \frac{1}{\sqrt{2\pi}\sigma_X} \exp\left(-\frac{(\Delta X - \mu_X)^2}{2{\sigma_X}^2}\right) \quad \text{(B.16)}$$

$$f(\Delta Y) \simeq \frac{1}{\sqrt{2\pi}\sigma_Y} \exp\left(-\frac{(\Delta Y - \mu_Y)^2}{2{\sigma_Y}^2}\right) \quad \text{(B.17)}$$

where $\mu_X = (-0.4 \pm 0.6)$ m, $\sigma_X = (14.5 \pm 0.6)$ m, $\mu_Y = (3.6 \pm 0.7)$ m and $\sigma_Y = (16.8 \pm 0.8)$ m. We note that ΔX and ΔY are independent, [1] so that their combined probability density function is simply the product of their individual density functions. In addition, we take $\mu_X = 0$ m and define $\sigma_R \equiv 15$ m $\simeq \sigma_X \simeq \sigma_Y$. Therefore:

$$f(\Delta X, \Delta Y) \simeq \frac{1}{2\pi {\sigma_R}^2} \exp\left(-\frac{(\Delta X)^2 + (\Delta Y - \mu_Y)^2}{2{\sigma_R}^2}\right) \quad \text{(B.18)}$$

$$\simeq \frac{1}{2\pi {\sigma_R}^2} \exp\left(-\frac{(\Delta X)^2 + (\Delta Y)^2 + {\mu_Y}^2 - 2(\Delta Y)\mu_Y}{2{\sigma_R}^2}\right) \quad \text{(B.19)}$$

$$\simeq \frac{1}{2\pi {\sigma_R}^2} \exp\left(-\frac{(\Delta R)^2 + {\mu_Y}^2 - 2(\Delta Y)\mu_Y}{2{\sigma_R}^2}\right) \quad \text{(B.20)}$$

where we have used $(\Delta R)^2 = (\Delta X)^2 + (\Delta Y)^2$ in the last step. In the exponential, the term in $(\Delta R)^2$ is of order 10^3 m^2 (see Fig. 4.28), the term in ${\mu_Y}^2$ is of order 10 m^2 and the term in $(\Delta Y)\mu_Y$ is of order $50 - 100$ m^2. Therefore, approximately:

$$f(\Delta X, \Delta Y) \approx \frac{1}{2\pi {\sigma_R}^2} \exp\left(-\frac{(\Delta R)^2}{2{\sigma_R}^2}\right) \quad \text{(B.21)}$$

and we expect the distribution of $(\Delta R)^2$ to be exponential with a slope $2{\sigma_R}^2 = 450$ m^2.

[1] Note that this statement is not exactly true, since MACRO measures the coordinates X and D (see Section 2.3), and Y is calculated from X and D and is therefore not entirely independent of X; however, this correlation is so small as to be negligible, and X and Y can be considered independent to a very good approximation.

Bibliography

[1] MACRO and EAS-TOP Collaborations (R. Bellotti *et al.*), *Proc. 22nd Intern. Cosmic Ray Conf.* (Dublin, 1991), vol. 2, p. 61 and vol. 4, p. 563.

[2] EAS-TOP and MACRO Collaborations (M. Aglietta *et al.*), *Proc. 23rd Intern. Cosmic Ray Conf.* (Calgary, 1993), to be published in July 1993.

[3] PROTON Collaboration (N.L. Grigorov *et al.*), *Sov. J. Nucl. Phys.* **11**, 588 (1970).

[4] JACEE Collaboration (T.H. Burnett *et al.*), *Astrophys. J.* **327**, L31 (1988), and (K. Asakimori *et al.*), *Proc. 22nd Intern. Cosmic Ray Conf.* (Dublin, 1991), vol. 2, p. 57.

[5] Tien Shan Collaboration (T.V. Danilova *et al.*), *Proc. 15th Intern. Cosmic Ray Conf.* (Plovdiv, 1977), vol. 8, p. 129.

[6] Akeno Collaboration (M. Nagano *et al.*), *J. Phys. G: Nucl. Phys.* **10**, 1295 (1984).

[7] A.J. Bower *et al.*, *J. Phys. G: Nucl. Phys.* **9**, L53 (1983).

[8] M. Ichimura *et al.*, University of Tokyo's Institute for Cosmic Ray Research preprint ICRR-Report-287-92-25 (1992).

[9] K. Greisen, *Phys. Rev. Lett.* **16**, 748 (1966), and G.T. Zatsepin and V.A. Kuz'min, *Sov. Phys. – JETP Lett.* **4** (1978).

[10] J. Lloyd-Evans, *Proc. 22nd Intern. Cosmic Ray Conf.* (Dublin, 1991), vol. 5, p. 215.

[11] G.R. Burbidge, *Philos. Trans. R. Soc. London A* **277**, 481 (1974).

[12] J.A. Simpson, *Ann. Rev. Nucl. & Part. Sci.* **33**, 323 (1983).

[13] T.K. Gaisser, "Cosmic Rays and Particle Physics," Cambridge University Press (1990).

[14] P. Sokolsky, "Introduction to Ultrahigh Energy Cosmic Ray Physics," Addison-Wesley (1989).

[15] J.F. Ormes and W.R. Webber, *Proc. 9th Intern. Cosmic Ray Conf.* (London, 1965), vol. 1, p. 407.

[16] M.J. Ryan, J.F. Ormes and V.K. Balasubrahmanyan, *Phys. Rev. Lett.* **28**, 985 (1972).

[17] Y. Kawamura *et al.*, *Phys. Rev. D* **40**, 729 (1989).

[18] J.J. Engelmann *et al.*, *Astron. & Astrophys.* **233**, 96 (1990).

[19] M. Simon *et al.*, *Astrophys. J.* **239**, 712 (1980).

[20] D. Müller *et al.*, *Astrophys. J.* **374**, 356 (1991).

[21] B. Rossi and K. Greisen, *Revs. Mod. Phys.* **13**, 240 (1941).

[22] T.K. Gaisser and T. Stanev, *Nucl. Instrum. & Methods A* **235**, 183 (1985).

[23] MACRO Collaboration (S.P. Ahlen *et al.*), *Phys. Rev. D* **46**, 895 (1992).

[24] Fréjus Collaboration (Ch. Berger *et al.*), *Phys. Rev. D* **40**, 2163 (1989).

[25] G. Auriemma, S. Bussino, T.K. Gaisser and T. Stanev, *Proc. 22nd Intern. Cosmic Ray Conf.* (Dublin, 1991), vol. 2, p. 101.

[26] Homestake Collaboration (D.B. Kieda *et al.*), *Proc. 21st Intern. Cosmic Ray Conf.* (Adelaide, 1990), vol. 3, p. 112.

[27] A.E. Chudakov, A.L. Tsyabuk and A.V. Voevodsky, *Proc. 22nd Intern. Cosmic Ray Conf.* (Dublin, 1991), vol. 2, p. 5.

[28] NUSEX Collaboration (G. Bologna *et al.*), *Nuov. Cim. C* **8**, 76 (1985). Also M. Aglietta *et al.*, *Nucl. Phys. B (Proc. Suppl.)* **14B**, 193 (1990).

[29] G.B. Yodh, J.A. Goodman, S.C. Tonwar and R.W. Ellsworth, *Phys. Rev. D* **29**, 892 (1984).

[30] Ohya Collaboration (T. Aoki *et al.*), *Proc. 21st Intern. Cosmic Ray Conf.* (Adelaide, 1990), vol. 3, p. 116.

[31] Mt. Fuji and China-Japan Collaborations (J.R. Ren *et al.*), *Proc. 21st Intern. Cosmic Ray Conf.* (Adelaide, 1990), vol. 8, p. 186.

[32] J.A. Goodman *et al.*, *Phys. Rev. D* **26**, 1043 (1982).

[33] H.T. Freudenreich *et al.*, *Phys. Rev. D* **41**, 2732 (1990).

[34] M.P. Chantler *et al.*, *J. Phys. G: Nucl. Phys.* **9**, L27 (1983).

[35] Fly's Eye Collaboration (G.L. Cassiday *et al.*), *Proc. 21st Intern. Cosmic Ray Conf.* (Adelaide, 1990), vol. 3, p. 154.

[36] R. Walker and A.A. Watson, *J. Phys. G: Nucl. Phys.* **8**, 1131 (1982).

[37] A.M. Hillas, *Ann. Rev. Astron. Astrophys.* **22**, 425 (1984).

[38] R. Blandford and D. Eichler, *Phys. Rep.* **154**, 1 (1987).

[39] P. Kiraly *et al.*, *Riv. Nuov. Cim. (Ser. 3)* **2** (7), 1 (1979).

[40] P. Sreekumar *et al.*, *Phys. Rev. Lett.* **70**, 127 (1993).

[41] C.J. Cesarsky, *Ann. Rev. Astron. Astrophys.* **18**, 289 (1980).

[42] C.J. Cesarsky, *Proc. 20th Intern. Cosmic Ray Conf.* (Moscow, 1987), vol. 8, p. 87.

[43] S.P. Swordy, J. L'Heureux, P. Meyer and D. Müller, *Astrophys. J.* **403**, 658 (1993).

[44] R.J. Protheroe and A.P. Szabo, *Phys. Rev. Lett.* **69**, 2885 (1992).

[45] C.E. Fichtel and J. Linsley, *Astrophys. J.* **300**, 474 (1986).

[46] D.E. Nagle, T.K. Gaisser and R.J. Protheroe, *Ann. Rev. Nucl. Part. Sci.* **38**, 609 (1988).

[47] P.H. Barrett *et al.*, *Rev. Mod. Phys.* **24**, 133 (1952).

[48] U. DasGupta, T.H. Fields and K. Ruddick, *Proc. 22nd Intern. Cosmic Ray Conf.* (Dublin, 1991), vol. 2, p. 33.

[49] Soudan 2 Collaboration (W.W.M. Allison *et al.*), *Proc. 22nd Intern. Cosmic Ray Conf.* (Dublin, 1991), vol. 2, p. 65.

[50] EAS-TOP and LVD Collaborations (M. Aglietta *et al.*), Gran Sasso preprint LNGS-93/50 (1993).

[51] E. Bellotti, *Nucl. Instrum. & Methods A* **264**, 1 (1988).

[52] MACRO Collaboration (S.P. Ahlen *et al.*), *Nucl. Instrum. & Methods A* **324**, 337 (1993).

[53] MACRO Collaboration (R. Bellotti *et al.*), *Proc. 21st Intern. Cosmic Ray Conf.* (Adelaide, 1990), vol. 10, p. 75.

[54] MACRO Collaboration (S.P. Ahlen *et al.*), *Phys. Rev. Lett.* **69**, 1860 (1992).

[55] MACRO Collaboration (S.P. Ahlen *et al.*), *Astropart. Phys.* **1**, 11 (1992).

[56] MACRO Collaboration (S.P. Ahlen *et al.*), accepted by *Astrophys. J.* (to appear in the July 20, 1993 issue).

[57] MACRO Collaboration (S.P. Ahlen *et al.*), *Phys. Lett. B* **249**, 149 (1990).

[58] MACRO Collaboration (S.P. Ahlen *et al.*), *Nucl. Phys. B* **370**, 432 (1992).

[59] MACRO Collaboration (S.P. Ahlen *et al.*), *Phys. Rev. D* **46**, 4836 (1992).

[60] MACRO and EAS-TOP Collaborations (R. Bellotti *et al.*), *Phys. Rev. D* **42**, 1396 (1990).

[61] G. Battistoni *et al.*, *Nucl. Instrum. & Methods A* **235**, 91 (1985).

[62] G. Battistoni *et al.*, *Nucl. Instrum. & Methods* **176**, 297 (1980).

[63] K. Hikasa *et al.* (Particle Data Group), "Review of Particle Properties," *Phys. Rev. D* **45** (1992).

[64] EAS-TOP Collaboration (M. Aglietta *et al.*), *Nuov. Cim. C* **9**, 262 (1986).

[65] EAS-TOP Collaboration (M. Aglietta *et al.*), *Nucl. Instrum. & Methods A* **277**, 23 (1989).

[66] EAS-TOP Collaboration (M. Aglietta *et al.*), *Proc. 22nd Intern. Cosmic Ray Conf.* (Dublin, 1991), vol. 4, p. 512.

[67] EAS-TOP Collaboration (M. Aglietta *et al.*), *Proc. 22nd Intern. Cosmic Ray Conf.* (Dublin, 1991), vol. 4, p. 323.

[68] EAS-TOP Collaboration (M. Aglietta *et al.*), *Proc. 22nd Intern. Cosmic Ray Conf.* (Dublin, 1991), vol. 1, p. 277 and p.404. Also *Europhys. Lett.* **15**, 81 (1991).

[69] EAS-TOP Collaboration (M. Aglietta *et al.*), *Proc. 22nd Intern. Cosmic Ray Conf.* (Dublin, 1991), vol. 2, p. 708.

[70] K. Greisen, *Prog. Cosmic Ray Phys.* **3**, 1 (1956).

[71] E.J. Fenyves *et al.*, *Phys. Rev. D* **37**, 649 (1988).

[72] F. Arneodo, Tesi di Laurea, Universita di Torino (1990), and M. Carboni, Tesi di Laurea, Universita di Roma "La Sapienza" (1991).

[73] W.H. Press, B.P. Flannery, S.A. Teukolsky and W.T. Vetterling, "Numerical Recipes - The Art of Scientific Computing," Cambridge University Press (1986).

[74] R. Brun, O. Couet, C. Vandoni and P. Zanarini, "PAW - Physics Analysis Workstation," CERN program library (entry Q121) writeup, CERN, Geneva, Switzerland (1989).

[75] C. Forti *et al.*, *Phys. Rev. D* **42**, 3668 (1990).

[76] H. Bilokon *et al.*, *Proc. 20th Intern. Cosmic Ray Conf.* (Moscow, 1987), vol. 9, p. 199.

[77] UA5 Collaboration (G.J. Alner *et al.*), CERN Report no. CERN-EP/86-213, Geneva, Switzerland (1986).

[78] T.K. Gaisser, U.P. Sukhatme and G.B. Yodh, *Phys. Rev. D* **36**, 1350 (1987).

[79] J.W. Elbert *et al.*, *Phys. Rev. D* **12**, 660 (1975).

[80] R. Brun *et al.*, GEANT3 manual, CERN Report no. CERN DD/EE/84-1, Geneva, Switzerland (1987).

[81] G. Auriemma, T.K. Gaisser and T. Stanev, *Proc. 21st Intern. Cosmic Ray Conf.* (Adelaide, 1990), vol. 9, p. 362.

[82] G. Battistoni, private communication.

[83] T.K. Gaisser, Bartol Research Institute preprint BA-92-80 (1992).

[84] P. Vallania, private communication.